Development of an Optical Setup for the Detection of Nitrates in Water Systems under the European Project INNOAQUA

Bernardo de Meireles Carneiro
Master in Engineering Physics
Department of Physics and Astronomy
Faculty of Sciences of the University of Porto
2024

Development of an Optical Setup for the Detection of Nitrates in Water Systems under the European Project INNOAQUA

Bernardo de Meireles Carneiro

Dissertation carried out as part of the Master in Engineering Physics

Department of Physics and Astronomy

2024

Supervisor
Prof. Dr. Luís Carlos Costa Coelho, Professor Auxiliar Convidado, FCUP, INESC TEC

Co-supervisor
Dr. João Pedro Mendes, Investigador Auxiliar, FCUP, INESC TEC

Co-supervisor
Prof. Dr. José Manuel Marques Martins de Almeida, Professor Associado, UTAD, INESC TEC

U.PORTO

FACULDADE DE CIÊNCIAS
UNIVERSIDADE DO PORTO

INESCTEC
TECHNOLOGY & SCIENCE

“ Eu tô cansado

Me salva ”

Milton Nascimento, *A Chamada* from *Milagre dos Peixes*

Acknowledgements

This dissertation marks the end of the first paragraph of my academic journey and scientific work not with a full stop, but with an ellipsis. The work done compiles not only my vocabulary, but also of everyone that helped me, in italicized and bold words. Hence, as one must credit a citation, I must acknowledge everyone that supported me.

Firstly, I wanna thank my supervisor, Dr. Luis Coelho, and co-supervisors, Dr. João Mendes and Dr. José Manuel de Almeida, for their support and guidance throughout this project. Their contributions, advises and expertise were invaluable for not only enrich this work when it comes to knowledge of optics and instrumentation, but also my abilities as a person: the autonomy and trust given not only helped me experiment, but also fail and learn with that. I wanna also thank my laboratory colleagues and all the people from the BioLab team, especially the ones who also integrated in the INNOAQUA project for their help and support for the past year.

I wanna thank FCUP and INESC TEC, namely the people from CAP that integrated me in their projects and introduced me to the world of research and scientific investigation. This dissertation couldn't have been made without the help from Carlos Gaspar Pacheco and his knowledge when it comes to electrical engineering.

I also wanna thank the INNOAQUA project for financing this project with a grant and giving me financial motivation.

The best thing this academic path gave me were my closest friends: Rui, Yuri, Bárbara and Carolina and for that, they deserve my warm words of gratitude. This couldn't have been done without the shared laughs, frustrations and moments of love and friendship shared. Especially for Rui, lab and table partner, work and study colleague and most importantly, best friend, that I thank his company, help, tolerance and love.

Cherished words of gratitude and admiration are also sent to my partner and lover, Ezra. Their love is one of the reason that motivates me everyday to grow up and pursuit my happiness. Thank you for laughing and crying with me through all the best and bad moments.

Finally, affectionate words of gratitude is nourished by me to my family. I wanna thank my mother and father for giving me an opportunity to study academically and support my curiosity and dreams. Thank you for all the unconditional love and for hearing me,

even when I'm not right. I wanna thank my siblings: Sara, Tomás and Duarte and their partners: André and Mafalda for advising me, making this whole endeavor easier and loving me. Thank you for hearing me rambling about everything: from my passions to my frustrations. I wanna give my most special gratitude for my loved nephews: Valentina, Sebastião, Estêvão and Safia for nourishing me with happiness with their silliness. I also wanna thank my cats: Kika and Mia.

Resumo

Devido ao excessivo consumo humano dos recursos naturais, a gestão destes mesmos é um tópico cada vez mais importante que pressiona a procura de novas alternativas sustentáveis de forma a reduzi-lo. A sobrepesca é um exemplo de consumo excessivo que coloca ecossistemas marinhos em perigo. A aquacultura é uma alternativa que consegue superar certos problemas da sobrepesca, porém, contribui para a eutroficação marinha através do aumento da concentração nitrato e nitrito dissolvido em água. Estes compostos são essenciais para a cultura de algas que não só são usadas como fonte de alimentação, como também para a produção de fontes de energia sustentáveis como os biocombustíveis.

Esta tese relata o desenvolvimento de um sensor ótico que será utilizado na monitorização da concentração de nitrato em reservatórios de aquacultura, fazendo parte do projeto europeu INNOAQUA, que ambiciona promover e criar métodos sustentáveis como sistemas de aquacultura multitrófica integrada e de recirculação. Através da exploração da gama UV do espetro de absorbância do nitrato dissolvido com uma configuração de LEDs/fotodetetores, uma unidade de controlo optoelectrónica foi desenvolvida, visionando não só uma fácil acessibilidade, como também um baixo custo e manutenção, sendo capaz de realizar medições periodicamente.

Este sistema foi testado num ambiente controlado com concentrações de nitrato dissolvido em agua na gama dos 5 aos 30ppm, atingindo uma resolução de 0.01ppm. Posteriormente, este sistema foi testado num aquário de algas *Ulva* construído no laboratório.

Palavras-chave: física, ótica, absorbância, instrumentação, sensor ótico, nitrato, nitrite, algas, aquacultura, sustentabilidade

Abstract

The management of natural resources has become increasingly important due to the negative impacts of excessive human consumption which led to an increase of fishing activity, putting marine ecosystems in jeopardy. As a result, finding sustainable alternative solutions is more crucial than ever. Aquaculture plays a key role in addressing challenges, but also contributes to marine eutrophication by increasing concentration levels of dissolved nitrates and nitrites. These compounds are essential for algae growth, which can be used for food production and sustainable energy sources, such as biofuels, offering an alternative to fossil fuels.

The European project INNOAQUA aims to promote and create sustainable methods for aquaculture, recirculating aquaculture systems with integrated multi-trophic aquaculture.

This thesis presesnts the development of an optical sensor for monitoring dissolved nitrate levels in aquaculture reservoirs, carried out as part of the INNOAQUA project. The goal was to create a sensing setup that is affordable, reliable with low-maintenance, capable of performing automated and periodic measurements over extended periods. This was achieved by exploring the optical absorbance of dissolved nitrate in the UV spectrum range using LEDs/photodetectors configurations. Several methods were implemented and tested to optimize different sensor's parameters, including the selection of the most suitable wavelengths and optical paths for each LED/photodetector configuration.

An optoelectronic control unit was developed to automate the measurement process, integrating optimized electronics for autonomous water sample analysis from the monitored tank. The system was tested in a controlled environment within a nitrate concentration range of 5 to 30ppm, achieving a resolution of 0.01ppm. Following these results, the system was further evaluated in the laboratory using a small-scale *Ulva* algae tank.

Keywords: physics, optics, optical absorbance, instrumentation, optical sensor, nitrates, nitrites, algae, aquaculture, sustainability

Table of Contents

List of Tables

List of Figures

1. Introduction

1.1. Motivation and Outline

As human population increases, an heavier pressure on natural resources is applied. It is expected that by 2050, the world population will reach 9.5 billion individuals [1]. The need for a sustainable methods in the food industry, encompassing both aquaculture and agriculture, is imperative, as these will have to increase their respective production. These essential activities rely on tons of important resources, such as water and soil, energy and chemicals just to be sustained. Their environmental footprint is composed by soil degradation [1], biodiversity loss [2, 3] and greenhouse gas emissions [3, 4]. With the advent of global warming, it is expected that this footprint increases as new hardships show up [5].

This thesis is about the development of an optical sensor that will be used in new sustainable methodologies for aquaculture as part of the INNOAQUA project. Aquaculture presents itself as one of the most important sources of food worldwide, but its unsustainable practice can lead to dangerous and critical outcomes that must be overcome.

1.1.1 Aquaculture

Forms of culture and breeding of aquatic species, typically fish, have been linked with human civilization's advent, having its earlier practices in ancient cultures worldwide [6, 7]. This old practice has taken many forms and various degrees of importance as centuries have passed, and it is now more important than ever. Due to the increasing influence of humankind on marine life and the over-exploration of its resources, sustainable fishing is now more important than ever. Therefore, aquaculture was pushed to the spotlight and won the title of being the fastest-growing food-producing sector in the world for 50 years [6–8].

Aquaculture is a diverse practice that encompasses not only the production of fish populations like carps, salmon and catfish, but also of mollusks, crustaceans, seaweed and algae [9]. The aquaculture of algae is called algaculture and is done with micro and macroalgae. The culture of microalgae is in high demand as a food source, namely for the culture of other aquatic animals. In their larvae form, it is essential for the culture and growth of filter-feeding species, decapod crustaceans and bivalve mollusks[10]. Macroalgae are

also used as a food source for many species later in their life cycle such as the sea bass [10, 11]. More than 700 species of macroalgae are also edible to humans, comprising the diet and gastronomy of many people and cultures, especially, but not exclusively, in East Asia [5, 12]. This way, seaweed farming ends up being a significant economic sector, having in 2019 a production of 34.7 million tonnes worldwide, comprising the work of thousands of workers [12]. As most aquatic species produced come from freshwater, this leaves most aquaculture using freshwater from rivers, lakes, groundwater, etc [13], where, up to 63% of all aquaculture production worldwide comes from freshwater reservoirs [14]. Saltwater aquaculture is also practiced in coastal regions with water from oceans, estuaries and bays, etc [13]. Both types of aquaculture can be practiced in tanks and ponds or in cages, Figure 1.1. Generally, cages tend to be more invasive methods as they are placed in pre-existing environment[13]. This increased rely in freshwater aquaculture ends up affecting negatively present and future water management as only 3% of all global water is freshwater and only 10% of it comes from the surface [15].

Figure 1.1: a) Freshwater aquaculture ponds; b) Offshore saltwater aquaculture cages

The increase of aquaculture practice, brought by its economic viability, was faster than the awareness needed to prevent some negative impacts that come with its malpractice. Although this practice creates jobs and is associated with economical and social benefits that reduce poverty in many places in the world [13, 16], new products and methods are pushed to increase profit and reduce investment, creating intense aquaculture, where new non-natural diets and methods are tested for the faster growth of cultures [6, 17]. These methods leave a big footprint in the landscape, in particular when building ponds and tanks on land-based systems where big areas of land are occupied with these cultures that put pressure on already existing ecosystems and economic activities that need land

like agriculture for example [18]. This also disrupts sedimentation processes in ecosystems. As some coastal agriculture fields are converted to aquaculture, increased erosion is observed which is caused by the destruction of mangrove regions due to aquaculture activities [19]. This not only leads to habitat destruction for many species but also accelerates coastal loss [20]. Additionally, due to evaporation, oxygen depletion and waste, a significant amount of water must be replenished in ponds and tanks [15, 21, 22], requiring a high water consumption. Ensuring sustainable water use is now more critical than ever. This means that the reliability in aquaculture is directly related to the availability of sufficient water resources.

The use of antibiotics for the protection of aquatic species from infections is a problem that is building up due to the inevitable growth of resistant bacteria and contamination of water reservoirs [23]. Beyond antibiotics, the use of different type of diets and pesticides end up increasing the concentration of many chemical species that are not desirable in water systems. These methods increase the concentration of nitrogenous compounds (NH_4^+, NO_2^- and NO_3^-) that are essential nutrients for the growth of micro and macroalgae, which end up over-fertilizing water [8]. High concentration of nitrite concentrations (NO_2^-) disrupt multiple physiological functions, such as respiration in fishes [24]. High concentrations of nitrate (NO_3^-) and nitrite ions in water can also harm humans, potentially causing methemoglobinemia in infants and increasing the risk of cancer in the digestive tract [8, 25, 26]. The uncontrolled growth of these algae leads to eutrophication that impacts negatively aquaculture ponds. If these ponds are not isolated, eutrophication will destroy marine ecosystems, as this event is toxic for fish and seagrass, and can also disrupt the balance of the zooplankton population [27].

1.1.2 Algaculture

Nitrate and nitrite are not just essential to control and detect in fishponds, but also for algaculture. This practice needs the control of these nitrogenous compounds to promote alage growth as these can be assimilated by microalgae for the synthesis of proteins, by reduction and transportation mechanisms [8, 28, 29].

Fish aquaculture assisted with algaculture

Algaculture can be combined with aquaculture of fish (figure 1.2), in which algae does not just prevent oxygen depletion of the pond, but also captures nitrogenous compounds and carbon that are essential to keep the aquatic species healthy, preventing the overuse

of antibiotics and medicine [28, 30]. Wastewater from aquaculture is rich in inorganic molecules such as phosphorus, nitrogen and carbon and poor in toxic species like heavy metals. A high concentration of large particles is also possibly found that can increase the turbidity of the water, jeopardizing the growth of some algae species. This implementation of algae with the aquaculture of other aquatic species requires a unique and controlled treatment that can require more extensive investments, as the unbalance of the profile of nutrients is also something to consider [28, 30].

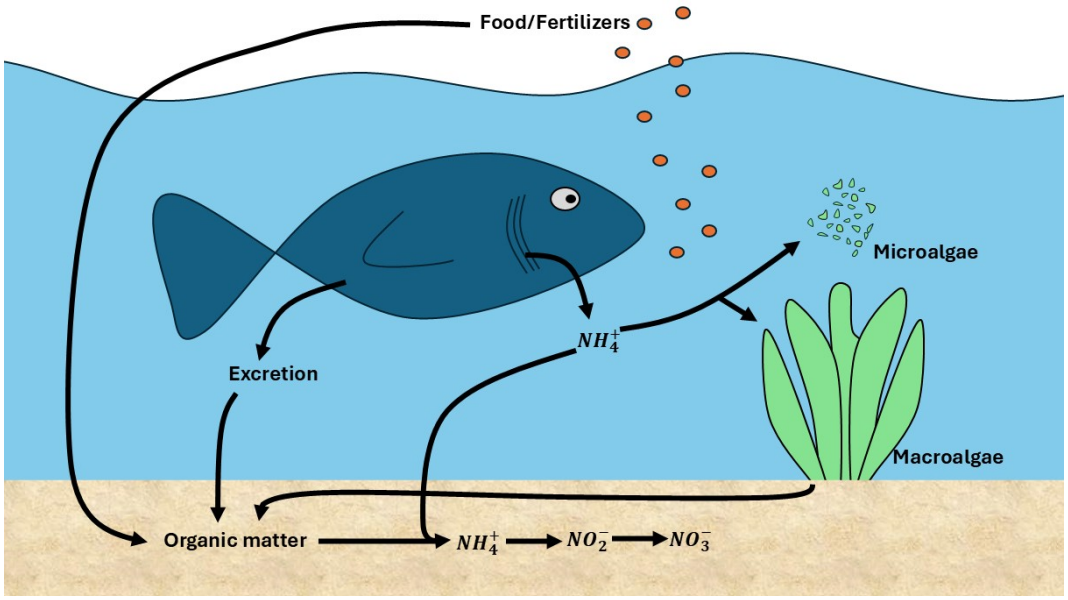

Figure 1.2: Creation of nitrogenous compounds in fishponds

Biofuel production

Beyond foodstock, lately, algaculture has also been associated with the production of biofuel and biodiesel. These consist of triglyceride molecules that microalgae can produce and accumulate [31]. This biosynthesis is usually a stress response made by unfavorable conditions for algae growth, such as nitrate depletion, as these molecules function as energy storage [32, 33]. Some of the products from microalgae's bioprocesses are shown in Figure 1.3.

As inorganic content in water reservoirs is depleted, the lipidic content in microalgae increases, but biomass production decreases, which presents a significant challenge in extracting biofuel from algaculture [34]. Additionally, the high production cost due to the need for precise control of several parameters further contribute to the key challenges that algaculture must overcome to become a viable global alternative for reducing the dependence on fossil fuels [34, 35].

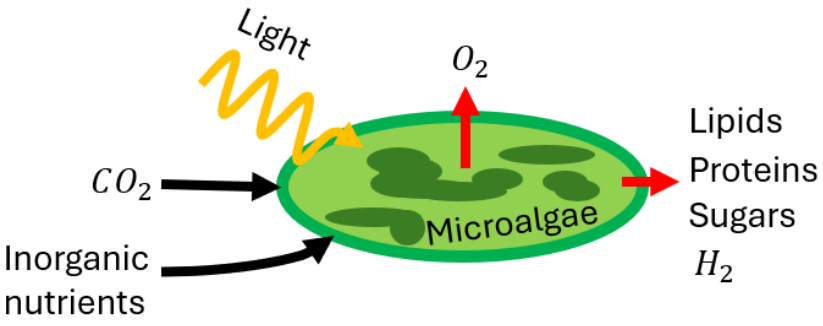

Figure 1.3: Microalgae's bioprocesses products

1.1.3 INNOAQUA Project

This thesis aims to develop a cost-effective and reliable optical sensor to measure dissolved nitrites and nitrates, NO_2^- and NO_3^-, and in wastewater from bass fish species for future application in the algaculture of *Ulva*. The sensor is intended to be used alongside with turbidity and CO_2 sensors in two aquaculture centers located in Portugal and Norway, as part of the INNOAQUA project. This initiative, funded by the European Union, seeks to "pave the path towards the upcoming sustainable and diversified EU in-land aquaculture industry by leaning on the demonstration and mainstreaming of innovative algae-based foods and solutions and ecology, circularity and digitalization concepts" [36]. This will be accomplished by:

- Demonstrating economic and ecological benefits of integrating fish tanks with algae tanks in combination with RAS-IMTA systems.
- Providing tools for recycling and renovating water, thereby reducing waste in aquaculture.
- Innovating processing methods for seafood products derived from algae.

RAS-IMTA systems combine the RAS (recirculating aquaculture system) with the IMTA (integrated multi-trophic aquaculture) system. RAS focuses on a variety of methods for the renovation of aquaculture water by filtering and reinserting it in the tanks, this way, the need for fresh water is reduced. This lets the water quality to be managed so that specific environments can be chosen [37, 38]. IMTA systems combine the cultivation of certain aquaculture species with other extractive species as seeweeds, that can be grown with wastewater from aquaculture with excessive organic and inorganic nutrients [39]. Thus, a long term sustainability and profitability can be achieved [39].

1.2. Nitrate and Nitrite Sensors: state of the art

The control nitrates and nitrites is essential not only for the growth of macro and microalgae, but also for sustainable aquaculture practices. These nitrogenous compounds, commonly used in agricultural fertilizers, can be harmful to humans and often leach into water systems through groundwater, increasing nitrate concentration in rivers and lakes [26, 40]. Consequently, the control and monitoring of nitrates and nitrites have become essential. Several methods have been developed for this purpose, which can be categorized into direct and indirect measurements [40, 41]. Generally, direct measurements are cheaper, more effective and more straightforward that indirect measurements, which require chemical agents and, consequently, produce chemical waste [40].

Detection methods for detecting NO_3^- and NO_2^- range from electrochemical detection [42], biosensors [43] and optical detection [44]. These can be implemented in analysis methods such as chromatography [45] and flow injection [46]. These detection and analysis methods can be combined and complemented with each other in different ways, each offering different ranges, resolutions, response times and degrees of complexity for implementation and maintenance. Typically, electrochemical biosensors and optical sensors are the most suitable options for remote and *in situ* water quality monitoring. Analysis methods such as flow injection and chromatography are known for their higher sensitivities and are more commonly used in laboratory applications due to their need for sample preparation procedures and expensive reagents for example [40]. These advantages and disadvantages are displayed in table 1.1.

1.2.1 Optical Sensors: spectroscopic methodologies

Optical sensors for NO_3^- and NO_2^- can be based in many different ways such as interferometry [47] for example, but most are based on spectroscopy [48], particularly using absorption methods in the ultraviolet (UV) and visible (VIS) range: for example, NO_3^- and NO_2^- exhibit absorption bands at approximately 215 nm [49] and $\sim$ 230 nm [50], respectively. To address potential interference from other chemical species, such as chlorine and iron (III), and organic matter, which absorb at similar wavelengths, a simpler measurement protocol is often used by detecting light at 220 nm and 275 nm, as NO_3^- does not absorb the latter wavelength [48, 51]. More complex UV-VIS spectroscopy methods have been implemented that use chemical reactions with NO_3^- and NO_2^- producing specific spectra indicative of their concentration in the medium. For example, one approach measures the optical absorption of a solution from an assay of soil extract at 210 nm

Table 1.1: **NO_3^- and NO_2^- detection and analysis methods advantages and disadvantages**

Detection	Advantage	Disadvantage
Electrochemical	• Simple operation; • Good sensitivity for ions in water; • Easily miniaturized; • Low power consumption;	• Complex development; • Harder to implement for soil applications;
Biosensors	• Can do *in situ* measurements; • Good sensitivities; • Can be used with other sensors;	• Complex development and implementation; • Requires the use of specific biomaterials
Optical	• Simple operation; • Customizable complexity of development; • Can be used with other sensors; • Can do *in situ* measurements;	• Harder to detect contaminants; • Better sensitivities and ranges require the use of reagents;

Analysis	Advantage	Disadvantage
Flow injection	• Higher sensitivities; • Hight-throughput analysis; • Low-sample volume; • Easy to operate;	• Complex use outside of lab; • Requires reagents;
Chromatography	• Higher sensitivities; • High detection range; • High limit of detection;	• Complex development; • Requires reagents; • Expensive; • Bulky;

before and after reducing NO_3^- to a non-absorbing species with the difference between both measurements proportional to the NO_3^- concentration in soil [50]. For NO_2^-, methods based on the Griess reaction [52] are commonly used, producing colored compounds in the 500-600nm range, where the intensity is proportional to the concentration of the respective species. Nitrate can also be detected in this way with an appropriate reduction of $NO_3^- \longrightarrow NO_2^-$ [52].

In addition to UV-VIS, infrared (IR) spectroscopy can also be used to excite the rotational and vibrational modes of the molecules. This way absorbance and reflectance spectrometry can be used to detect NO_3^- and NO_2^-, typically for soil species detection. For instance, NO_3^- can typically be analyzed around 7μm wavelength range [53, 54]. Other IR spectroscopy methods can be done with membranes that will react with the NO_3^- molecules and lead to the adsorption of these in the membrane. The concentration of NO_3^- is then determined by measuring the transmittance of the mid-infrared optical signal through the membrane [55].

Fluorescence methods can be employed, but typically require additional chemical agents to detect NO_3^- and NO_2^-. In the case of NO_3^-, a reduction to NO_2^- is needed beforehand, so that a nitrosation/diazotization process can occur between NO_2^- and other non-fluorescent material. This produces fluorescent chemical species that can be detected using a spectrometer after proper excitation [48]. The non-fluorescent material can be *3-amino-1,5-naphthalenedisulphonic acid* that reacts with NO_2^-, creating azoic acid with a detection limit of 10^{-8}M [56].

Fiber-based

Optical sensors generally follow the structure of a light source, a medium and a photodetector. Fiber-based sensors have their detection system based in the optical characteristics of optical fibers and are the most common optical sensors for nitrate and nitrite detection, [47, 57–62]. These give exceptional range and resolution without the need for reagents or membranes. Optical fiber-based sensors are highly resistant to external physical influences such as electromagnetic interference and corrosion [57]. Fiber-based detectors can be implemented as *Camas-Anzueto, et al*, did by substituting the coating of the fiber with a sensitive layer of lophine that will be in contact with the aquatic medium with the NO_3^- ions. Using this approach, the authors achieved a sensor with a range of 1mg/L to 70mg/L and a response time of 20ms [60]. Similarly, *Nahla.A.Aljaber, et al* enhanced sensitivity by removing the fiber cladding and exposing the core to the liquid containing the dissolved nitrates and nitrites [59]. This way, the medium will act as the new cladding and will interfere with the evanescent field depending on the concentration of the chemical species and the wavelength of the optical signal emitted. The power transmitted through the fiber will decrease with the increase of the concentration of NO_3^- and NO_2^- ions [59]. This sensor demonstrated sensitivity in the range of 1 to 1000ppb.

Another exciting configuration of an optical sensor is based on a Mach-Zehnder interferometer setup [47] where a photonic crystal fiber(PCF) was sandwiched between single-mode fibers. The PCF is then coated with the sensing layer, the graphite/PVA solution. At the boundary of the first single-mode fiber and the PCF, the optical mode gets diffracted exciting the modes in the cladding and the core of the PCF. This creates interference due to phase differences induced by the refractive index difference of the two media [63]. The refractive index of the cladding becomes sensitive to nitrate and nitrite concentrations due to the sensing layer capturing dissolved anions. This setup was designed for a sensor range of 0 to 100ppm, with intervals at 20ppm and a response time of 10 seconds [47].

Non-Fiber based

Non fiber-based sensors, without reagents typically rely on a straightforward optical measurement setup, where the intensity of the optical signal changes as it passes through a medium with varying concentrations of chemical species. This method involves a photodetector and a light source in the absorption wavelengths of NO_3^- and NO_2^- as reported by *E. Murray, et al.* [64]. By measuring the voltage output from the photodetector, the concentrations of NO_3^- and NO_2^- can be determined if no other interfering anions are present, as shown in Figure 1.4. Deep UV LED's are needed to see the absorption at $\lambda < 240$nm. One problem that comes with the use of LED's is their deterioration in performance with higher temperatures. This demands the use of heat sinks in these setups [65] when the current required is high (>10mA) [64]. This still leads to smaller power consumed by the LED (0.108W) than if it was a UV deuterium lamp (30 W). The detection limit achieved was 0.007 and 0.040 mg/L for NO_2^- and NO_3^-, respectively [64].

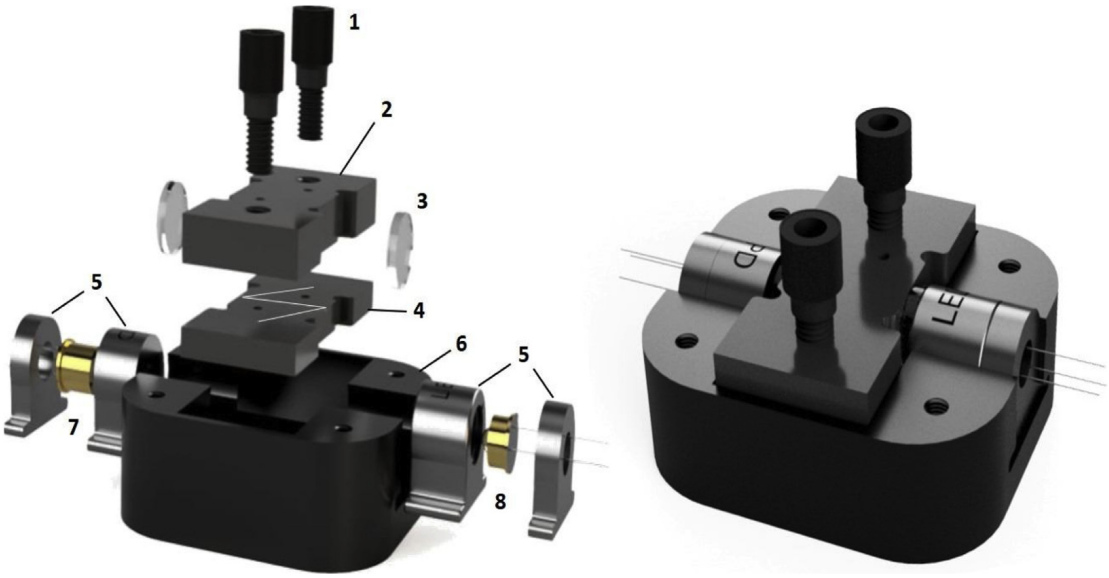

Figure 1.4: Disassembled (left) and assembled (right) optical sensor for nitrate detection. Legend: (1) Nut fittings;(2) Top PMMA layer with milled, threaded holes;(3) fused silica glass UV-transparent;(4) bottom PMMA layer fluidic channel;(5) 3D printed support for LED and photodiode;(6) 3D printed optical cell holder;(7) photodiode;(8) LED. Figure taken from [64].

Other simple non-fiber based sensor, use optical fibers, only as an optical propagator between each part of the sensor. In this philosophy, *Y. Moo, et al* [57] implemented a sensor based on the optical absorption characteristics of NO_3^- and NO_2^-, by using a deuterium tungsten halogen light source and a photodetector. This light source emits light from 185 nm to 1.1 μm. They detected two significant NO_3^- and NO_2^- absorption peaks at 302 nm and 356 nm, respectively. Using a filter to the light source, the sensor built had

a linear range of 0-50mg/L with a resolution of $\sim$ 1mg/L [57]. The use of lamps can be troublesome due to their response time and small lifetime expectancy when compared to LED's in general, especially in the UV range and when the whole spectrum is unnecessary [66]. This sensor was focused on an environment-friendly and economical approach. *M. Nehir, et al.* used a similar approach by adding a reference diode to monitor the optical signal in real time. This way, the direct comparison of the signal from the reference diode and after transmitting through the medium would avoid future calibrations that are needed due to the light source deterioration. The light source was also changed to Xenon flash lamp [58], due to their emission spectrum also share the range where it is possible to see absorption of NO_3^- and NO_2^-. This followed the same optical configuration as the one seen in figure 1.5.

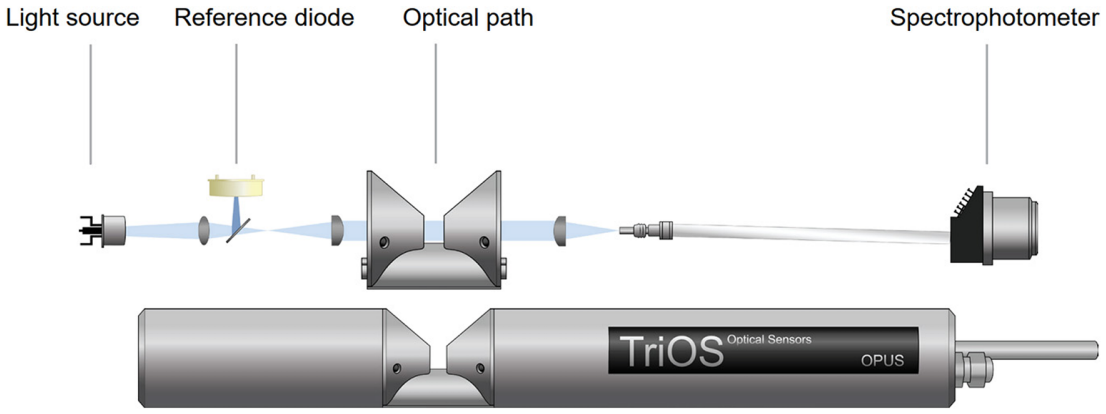

Figure 1.5: Optical configuration for the detection of NO_3^- and NO_2^- without the use of reagents. Figure taken from [58].

2. Materials and Methods

2.1. Light-Matter Interaction

To develop a light sensor, it is essential to understand that light can be used to obtain information about a certain material/medium by exploring three phenomena: reflection, absorption and transmittance. Every material interacts with light through these processes, and the nature of this interaction is unique to each material because different materials have different chemical structures and characteristics that will cause the analysis of these different phenomena to give a ”fingerprint” of the material/medium and its characteristics. The sensor to be developed, like many mentioned in Chapter 1, section 1.2, focuses on measuring the optical absorption of the medium that can be described using either classical or corpuscular approaches.

2.1.1 Classical approach

When an electromagnetic (EM) wave interacts with different media it induces distinct phenomena that are characteristic of the medium. This way, certain materials can be characterized based on their interaction with EM waves. Due to the atomic nature of mediums, an electric field will lead to the polarization of the molecules/atoms (Figure 2.1) and consequently a polarization field, P [67].

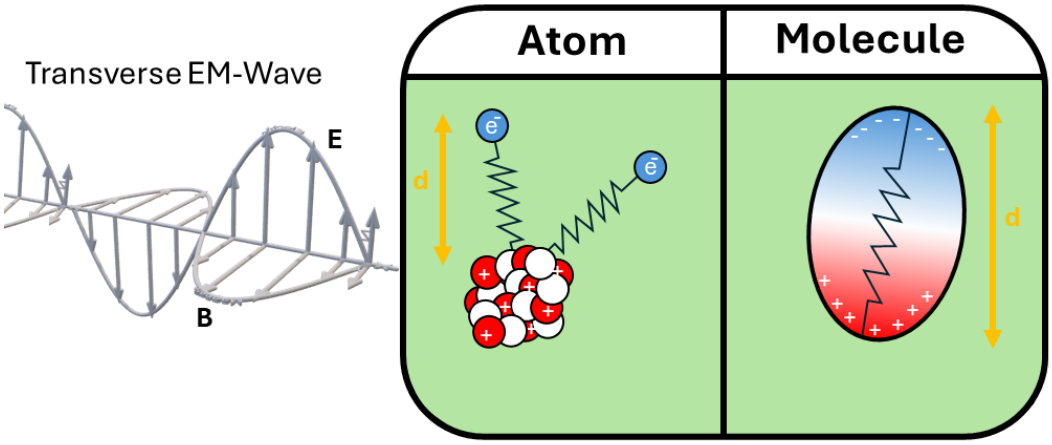

Figure 2.1: Polarization of atoms and molecules. An internal force is expected to arise that goes against the external electric field applied

The restorative forces within a particle after interacting with the applied electric field, E, can be modeled as springs according to Hook’s law with a damping condition. Both properties dependent on the intrinsic characteristics of the particle [68], equation 2.1.

$$\mu\frac{d^2r}{dt^2}+\mu\omega_0^2 r+\mu\gamma\frac{dr}{dt}=qE(t)\leftrightarrow r(t)=\frac{q}{\mu}\frac{E(t)}{\omega_0^2-\omega^2-i\gamma\omega} \tag{2.1}$$

Where ω_0 is the intrinsic frequency of the spring, μ is the reduced mass, and γ is the damping constant. The second part of equation 2.1 is the only valid solution for plane waves with frequency ω [68]. This displacement between charges, will lead to a dipole moment, p, and polarization density, P, given by equation 2.2, if the medium is isotropic and homogeneous[69].

$$p=qr\leftrightarrow P=qr\frac{N_A}{M}c \tag{2.2}$$

Where N_A, M and c are the Avogadro constant, the molar mass of the particles and mass concentration, respectively. As we know from the Maxwell equation in mediums, we get that polarization density and the external electric field are related with ϵ_r, $P=\epsilon_0(\epsilon_r-1)E$, and that the refractive index, n, can be given by $n^2=\epsilon_r$ [67]. This way, we will have a refractive index that depends on the frequency of the EM-wave and concentration of the particles, although non-linearly [68, 69]:

$$n=\sqrt{1+S\frac{\omega_0^2-\nu^2}{\left(\omega_0^2-\omega^2\right)^2+\gamma^2\omega^2}c+iS\frac{\omega\gamma}{\left(\omega_0^2-\omega^2\right)^2+\gamma^2\omega^2}c} \tag{2.3},$$

where we have that $S=q^2N_A/\mu\epsilon_0 M v^2$. For small enough concentration, c, equation (2.3), can go to $\sqrt{1+x}\approx 1+x/2$ (valid for $x<<1$). Where we have:

$$n_i\approx\frac{S}{2}\frac{\omega\gamma}{\left(\omega_0^2-\omega^2\right)^2+\gamma^2\omega^2}c=\frac{S}{2}\eta(\omega)c \tag{2.4},$$

the dispersion relation will be given by equation (2.5).:

$$\nu\approx n_r(\omega,c)\frac{\omega}{v}+ic\frac{\eta(\omega)}{2} \tag{2.5}.$$

This implies that the medium will exhibit both dispersion and absorption. The EM-wave and its corresponding intensity in the isotropic homogeneous medium, at low concentrations will be described by:

$$E(r,t) = Ee^{-\frac{\eta(\omega)c}{2}r}e^{-i\left(\omega t - n_r\frac{\omega}{v}r\right)} \rightarrow I(r) = E^2e^{-\eta(\omega)cr} \tag{2.3}$$

After crossing a distance of d, the absorbance will be given according to Beer-Lambert law [68, 70] (equation 2.4) as light intensity decreases. Although it was used ϵ_0, if the medium is contained in other medium transparent to the EM-Wave, the equation still applies, just with a new permittivity. The absorbance, A, will be given by:

$$A = \log\left(\frac{I_d}{I_0}\right) = \eta cd \tag{2.4}$$

Usually, η is named the molar absorption coefficient. Typically, non-linearity of the absorbance relative to the concentration is observed due to chemical interactions, local field effects, nearfield interactions and electromagnetic coupling [71, 72].

2.1.2 Corpuscular approach

In the corpuscular approach, considering that the particles possess rotational states, the rotational energy can only take specific values. These can generally be excited within the mid IR range [73]. Using the UV-VIS range usually leads to the excitation of electronic states for molecules [73]. The excitation of electronic states occurs through the interaction between the quantized EM-field, photon, with the electric field of the molecule: this way, the energy of the photon is transferred to the electron in a ground state, which makes the electron go to an excited state with that energy relative to the ground state [74] (Figure 2.2).

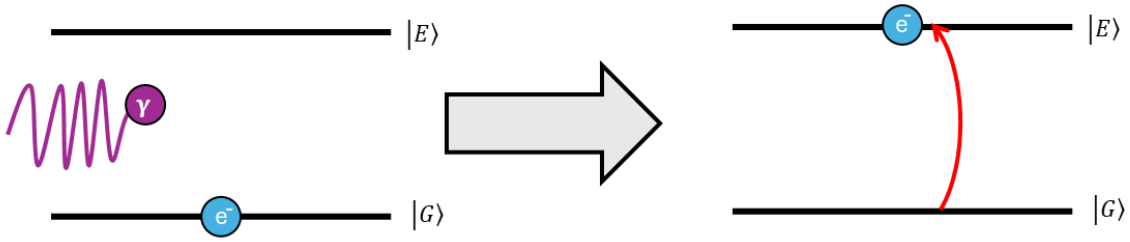

Figure 2.2: Photon, γ, absorption by an electron, e^-. The energy difference between the excited and ground state is the same as the photon energy

The simplest way to use this quantum paradigm is by modeling the photon as a point-like particle [75] that will interact with the molecules in the medium if it goes through the cross-section of the molecules [76, 77]. Assuming a circular cross-section and no interactions between the molecules, because the velocity of the photon is much bigger than the

molecular motion, the probability of one molecule interacting with the photon will be given just by the volume $p = v/V$ where $v = Sl$ and S the area of the cross-section. V is the volume of the container. This way, considering N molecules, the probability of n particles in the collision course of the photon will be given by the binomial distribution (equation 2.5) [77].

$$P(n) = \frac{N!}{(N-n)!n!}\left(\frac{v}{V}\right)^n\left(1-\frac{v}{V}\right)^{N-n} \tag{2.5}$$

Because $v << V$ and $N \to \infty$, equation 2.5 can be approximated accordingly $P(n) \approx e^{-np}\frac{(np)^n}{n!}$. This way, the probability of no particle being found by the photon during the trajectory will be given by the equation 2.6 [77].

$$P(0) \approx e^{-\frac{v}{V}N} \to \log\left(\frac{I_d}{I_d}\right) \approx -\mu Cl \tag{2.6}$$

For high intensity optical signals, multiphoton interactions with the medium start to be more common and cannot be modeled by such a simple approach [78]- It should also be noted that molecular orientation and photon polarization will influence the photon absorption which in turn also leads to deviations from what we have gotten from equation 2.6 [77].

2.2. Absorbance spectra

The first step for developing the sensor based on absorbance spectroscopy is the verification of the same absorption bands verified in chapter 1, section 1.2, for the anions NO_2^- and NO_3^-. It is crucial to determine what kind of light source will to be used. For both anions, it was possible to analyze the absorbance spectra for concentrations from 4 to 1000ppm (Table 2.1) of NO_3^- and NO_2^-, by diluting $NaNO_3$ and $NaNO_2$ in 500mL of deionized water. This was done by creating a stock solution of 1000ppm and preparing samples of 40mL.

The light source used was a tungsten-deuterium lamp (Hellma USA INC FiberLight), because it emits a spectrum in the wavelength range of 200 to 700nm (figure 2.3). A UV-Vis PMMA cuvette was used for this evaluation to avoid light absorption by the cuvette material in the region of interest. The spectra were acquired with a spectrometer (Ocean Optics XPTO) using a set of multimode optical fibers (Thorlabs FT600EMT) and collimators (Civillaser 74UV-FC) both working in the UV-Vis range.

Table 2.1: **Table of values used to quantify the concentration of NO_2^- and NO_3^- that was diluted in deionized water**

	Volume from stock(mL)	Concentration (ppm)
$NaNO_2$ and $NaNO_3$	40	1000
	20	500
	10	250
	5	125
	2.52	63
	1.24	31
	0.64	16
	0.32	8
	0.16	4

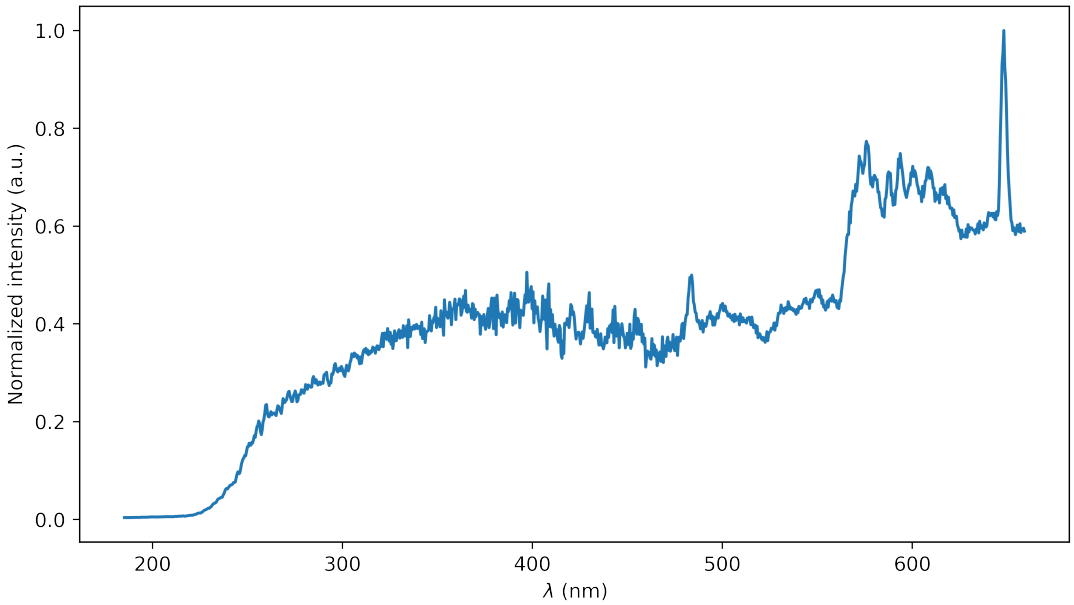

Figure 2.3: Emission spectrum of the lamp used throughout the measurements

Starting from 1000ppm, the stock solution, each concentration was approximately half of the last, because it is expected a exponential decay as described in chapter 2. For every concentration, the spectra were acquired with a sampling rate of 10Hz for approximately 1 minute, using a LabView homemade software (AgriSpec). The cuvette was covered with an optical protection to hide it from background lights in the laboratory, reducing possible errors, and the respective support was fixed to the table. The intensity of the lamp and alignment was maximized, without saturating the detector, so that the intensity of the signal relative to the background signal was as big as possible.

The absorbance spectrum of water dissolved with gaseous N_2. For this, a pipe connected to a reservoir of pressurized N_2 was placed into a beaker with deionized water. The valve of the reservoir was open for one minute. The same detection procedure detailed before was used. A schematic of the setup used is represented in Figure 2.4. The absorbance

for every wavelength was determined according to equation 2.4, where I_0 and I_d are the intensity of the optical signal with just deionized water and with the respective concentration, respectively. For every intensity, it was determined that $I_{d/0} = I_{measured} - I_{Dark}$ where $I_{measured}$ and I_{Dark} are averages of all the respective spectra registered.

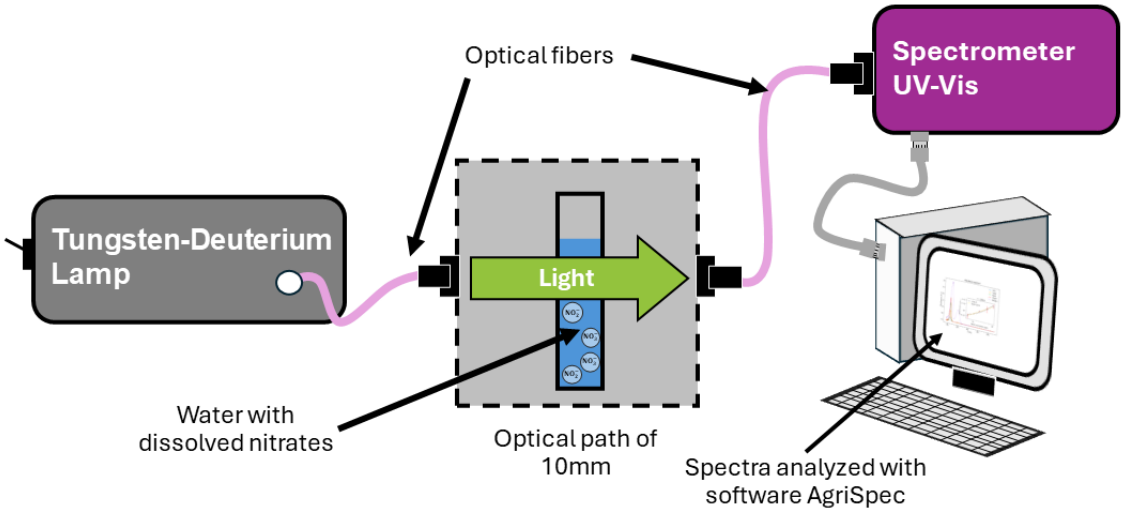

Figure 2.4: Experimental setup used to verify the absorbance spectra of nitrates and nitrites

2.3. Optical path determination

As expected by equation 2.4, increasing the optical path will lead to a more significant absorption of the optical signal. This can be explored so that the a specific range of detection can be chosen for the sensor without much complexity. The bigger the optical path, the lower the concentrations can be detected with the cost of needing a higher intensity for the light source due to water's absorbance spectra in the deep UV range [79]. This leads to other problems as a higher source of current will be needed and, most importantly, higher energy dissipation that can overheat and damage the light source. A heat sink will be needed if bigger currents (normally $\sim$100mA for LEDs) are used. An optimal optical path is one that balances each of these problems.

Two LEDs were used as light sources: LED1 (Silana UV SF1-3T9B5L1) and LED2 (Marktech Optoelectronics MTSM295UV2-F1120) for the 230 and 300nm range, respectively. It is essential that the LEDs have a small viewing angle, so that most of the optical signal emitted by the LEDs is used for the detection of NO_3^- and NO_2^-. A too small viewing angle requires a better alignment of the LED with the photodetector, which can hinder their respective testing and jeopardize results as it increases the sensitivity to possible vibrations in the system. As light detectors, two photodetectors were chosen (sglux TOCON_ABC1

and Roithner Lasertechnik GUVV-T21GH). Both have already an integrated amplification circuit, avoiding the future development of a transimpedance circuit to convert the current and amplify the signal of the photodetector. Because the photodetectors have an area of detection in the order of the $\sim$ 10mm^2 and the optical paths tested are in the order of the $\sim$ 10mm, the importance of the alignment between the LEDs and the photodetectors will increase significantly with the increase in length between them. Some of the most important characteristics of these devices are represented in table 2.2.

Table 2.2: **Different Characteristics of the LEDs and photodetectors used for the development of the sensor**

LED	**SF1-3T9B5L1**	**MTSM295UV2-F1120**
Peak Wavelength (nm)	234	295
Viewing Angle (º)	15	125
Max Forward Current (mA)	50	200
Forward Voltage (V)	5-7	5-6.5

Photodetector	**TOCON_ABC1**	**GUVV-T21GH**
Responsivity range (nm)	221-358	230-395
Max Responsivity	280 mV/nW/cm^2	1 mV/nW
Supply Voltage (V)	1.8-5.5	2.5-5.5

LED2 has a viewing angle of 125º, which is not optimal, as the optical signal starts to get lost if the respective photodetector is placed further than $\sim$ 1.5mm from the LED. A lens LC7 (*Roithner Lasertechnik*) with focal length of 7.8mm is used to collimate the optical signal from the LED for optical paths tested bigger than 7mm. This lens is made with PMMA material just like the cuvette in section 2.2 (see Appendix A for more information about the lens).

The experimental setup is represented in Figure 2.5. A support, fixed to the table, was built to hold and keep the LED and the photodetector/collimator aligned in order to minimize possible errors.The optical path between the LED and the photodetector/collimator was varied using fused quartz flow cells with 1, 5 and 10mm width. The photodetector was used to detect the expected raw electrical signal and the collimator to observe the respective spectra. For a photodetector, it was used an Arduino Due to detect the voltage of its output. Due to the maximum voltage input of the analogic pins of the Arduino Due being 3.3V, the photodetectors were supplied with 3.3V to avoid damaging them. The read data was saved using the *PuTTy* software. The collimator is connected to a spectrometer via a UV-VIS optical fiber. The spectra were captured using the *AgriSpec* software.

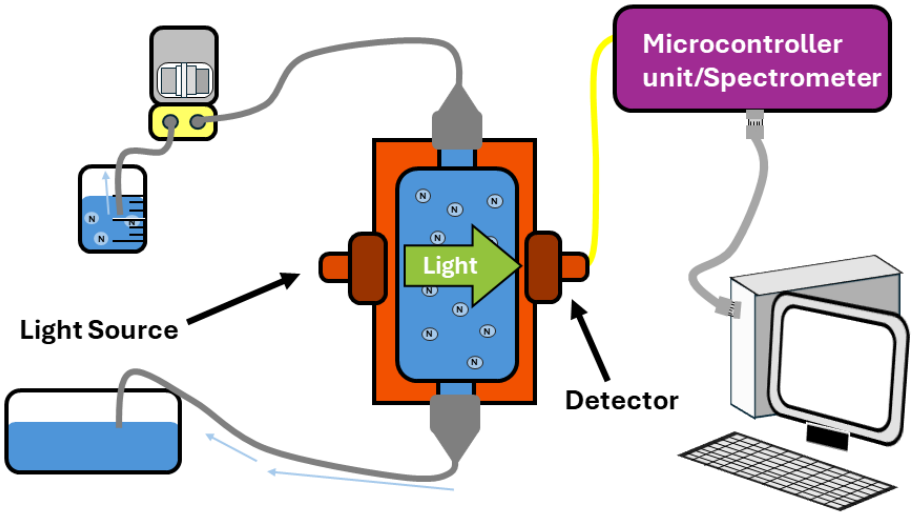

Figure 2.5: Experimental setup used to determine the optical path

Support for the flow cells was developed to increase the number of optical paths to be tested, such as the one in Figure 2.6 with a mirror. The optical signal is expected to bend due to water refraction. This way, the optical path, d will be given by equation 2.7 where θ is the angle, n_A is the refractive index of water and w_f is the width of the flow cell. The LED's and photodetectors are fixed by their respective support.

$$d = 2\frac{w_f}{\sqrt{\left(1 - \left(\frac{\sin(\theta)}{n_A}\right)^2\right)}} \tag{2.7}$$

According to the INNOAQUA project, it is expected for the sensor to detect NO_3^- and NO_2^- for concentrations of $\sim$20ppm. For every optical path, the spectrum/voltage measurements were done between 5 and 30ppm with a step of 5ppm. The medium was pumped through the flow cells with a peristaltic pump of 12V. When using photodetectors, the current supplied to LED1 was chosen to be as big as possible without saturating the photodetector or crossing the max forward current. LED2 required $\sim$ 100mA currents which led to overheating of the LED and possible damage. This issue was avoided by using a heat sink connected to the LED with a screw.

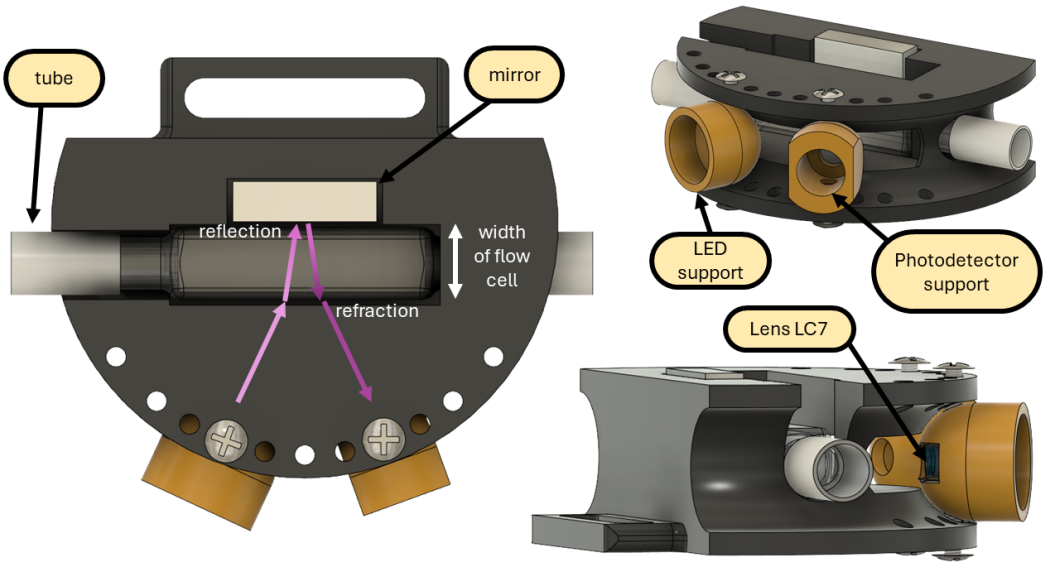

Figure 2.6: Support developed to increase the optical path for the LED/photodetector setup.

2.4. Signal Treatment

The LEDs and photodetectors were inserted in a prototype with a PCB already inserted. Each LED/photodetector followed the same setup of alignment as the one in Figure 2.5. The flowcell used had a width of 10mm. To characterize and understand the signal outputted by the sensor, it is necessary to do a calibration of each setup so that it is possible to assign a value of absorbance to a specific concentration, how much of the noise is reduced by the prototype and how it reacts with increasing temperature. To avoid possible errors like air bubble accumulation inside the tubes and the flow cell, the prototype was held to a support to keep it stable and vertically so that they could flow without difficulty.

Sensor calibration

The microcontroller used, ESP32-C6-DevKitC-1, was placed in the PCB, and the fluid system was controlled via a peristaltic pump, also connected to the PCB. This way, the fluid could be pushed through the flow cell without needing another power supply, as it was done in section 2.3. This way, to get the calibration equations for the detection LEDs, these would be turned on, and the ESP32 would save 30 thousand sample of the voltage detected for every concentration tested using a solution of $NaNO_3$ dissolved in deionized water, the same procedure done in Table 2.1. The sample frequency used was 1kHz. The tests were made for concentrations in the range of 0 to 1000ppm, from the solutions of dissolved $NaNO_3$ in deionized water. The setup used is in Figure 2.7.

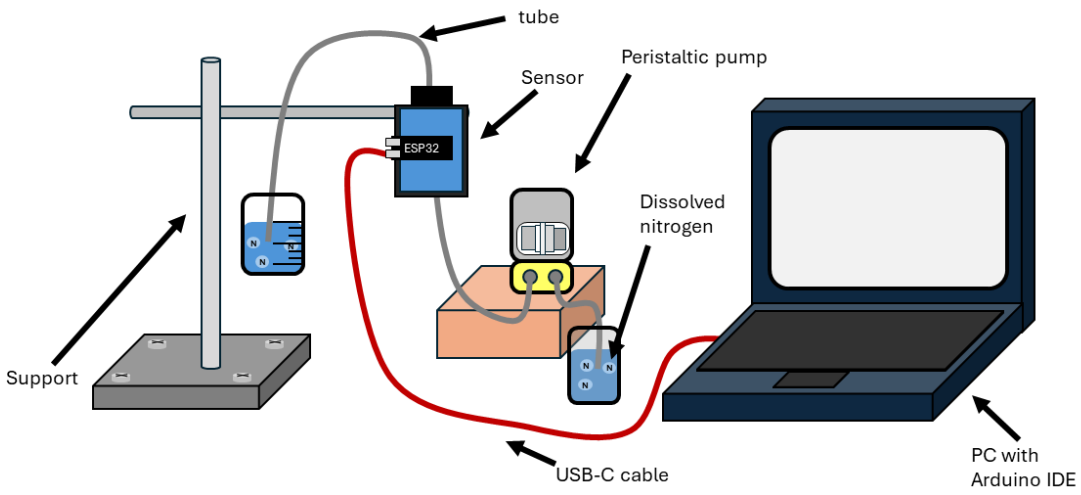

Figure 2.7: Schematic representation of the setup used for calibration of the sensor

Sensor noise reduction

To verify the reliability of each part of the system, each separated part was built in a breadboard and tested with the respective components. The noise before and after the filter and bypass capacitors were added was analyzed by detecting samples of the signal of each LED/photodetector setup for a minute without any digital processing, for example, averaging values. This way, it is possible to see how much the electronic signal varies before and after the filtering components are placed. This was tested for samples of dissolved $NaNO_3$ for concentrations ranging from 5 to 30ppm.

Thermal analysis

In general, all sensors depend on the environment's temperature and, consequently, its components. Using electronic devices will always end up heating the sensor, so even in a controlled environment, it is expected that the sensor may end up heating up. The sensor is expected to be placed in algae tanks exposed to sunlight all day. A thermal analysis needs to be done so that it is possible to understand how this factor will change the voltage detected.

There are two ways this analysis could be done. By maintaining a constant temperature and varying the concentration, registering the respective voltage values, or choosing a constant nitrate concentration in water and varying the temperature. The latter option was chosen because, to vary concentration, the peristaltic pump needs to be turned on with the environment at that T temperature, and due to its respective power consumption,

may end up damaging the circuit in which there's a lot of power dissipation when the peristaltic pump is turned on.

The setup used is represented in figure 2.8. For every concentration tested, it was ensured that the liquid was inside the flow cell; the sensor was inserted in a laboratory incubator (which can maintain a constant temperature inside) and was connected via USB-C to a PC with the Arduino IDE software so that data could be easily read in time. The sensor was powered and connected to an outside power socket. It was ensured that the wires were small enough to properly close the incubator door and maintain a constant temperature. The temperature was controlled by beginning at 27°C and increasing 5°C for each step, up to +20°C. The sensor was programmed to do measurements every two minutes. For each step, the voltage values given by the sensor were registered for 10 minutes to ensure that the whole environment was at a constant temperature. The samples tested were deionized water and concentrations of 5, 15 and 30ppm of N-NO_3^- dissolved in deionized water.

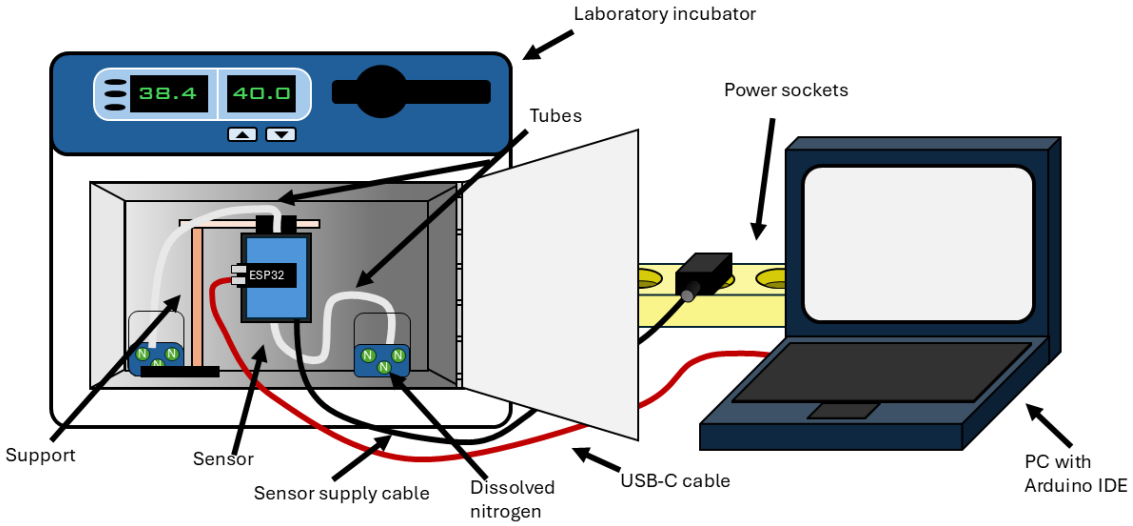

Figure 2.8: Setup used for the thermal analysis of the prototype of the sensor

Salinity analysis

The salinity response of the prototype was also tested to understand the prototype potential for also saltwater aquaculture. The setup used was similar to figure 2.7, but instead of using dissolved nitrate, solutions with different salinity percentage from 1% to 9% were used. These solutions were prepared by dissolving NaCl in deionized water. For each solution, the voltage of each LED/photodetector setup was registered for almost 30 seconds.

2.5. Sensor testing

2.5.1 Setup

To use the prototype built an aquarium tank was used where seawater was placed with the macroalgae. An air system inside the tank was built to force the circulation of water, avoiding the accumulation of algae and facilitating the dissolution of nutrients in water. The aquarium was inside an open box next to the window so that sunlight could reach the algae (as these are photosynthetic). A filter was placed inside the aquarium so that the sensor's tube could be placed there, avoiding the possibility of algae being pushed through the tubes. The entire setup used is represented schematically in Figure 2.9. The sensor was positioned in two ways (1 and 2, in Figure 2.9) relative to the window to see how sunlight could affect the sensor response. Each measurement is done every thirty minutes, approximately. Beyond testing the aquarium water, deionized water was also tested to see how the signal's voltage varied, compared with the first.

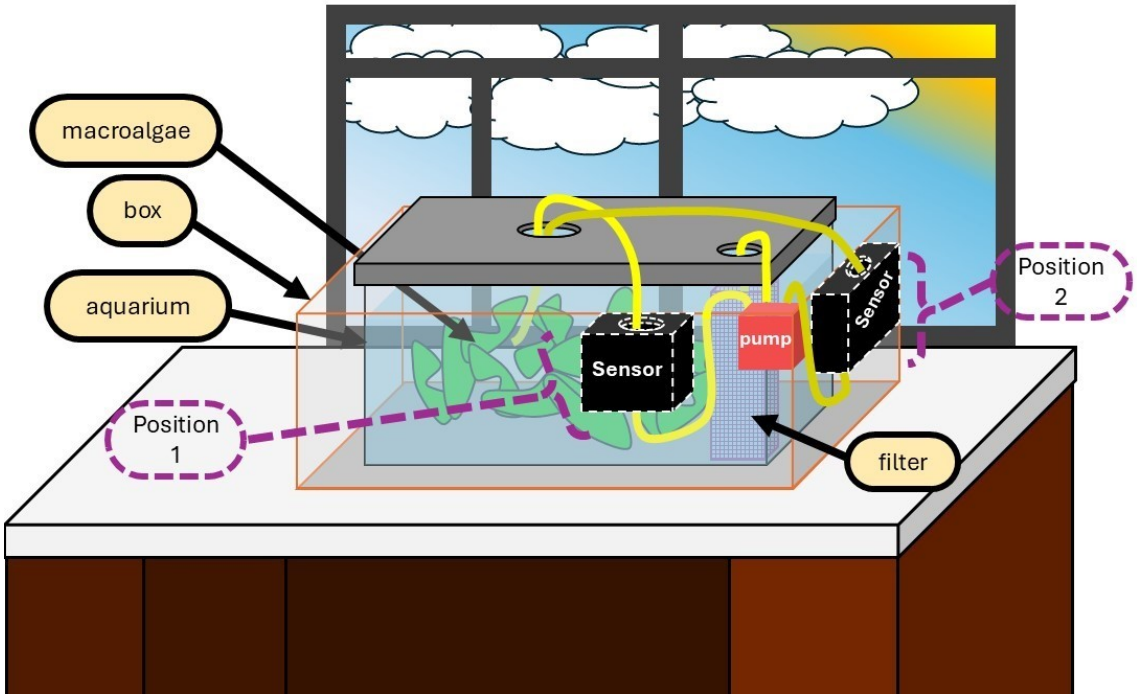

Figure 2.9: Schematic representation of the setup used to test the filters in water with algae

To know if the sensor is giving reliable values, a colorimetric approach was used to determine the amount of dissolved nitrates in water. This way, it is possible to compare these values with the sensor. These were done with a DR1900 Portable Spectrophotometer (**Hach**) following its internal protocols LCK138 for total nitrogen and LCK339 for total nitrate dissolved.

2.5.2 Code developed

To make each part of the circuit work, the ESP-32 needs to be programmed as this will be the basic procedure for its future use in the algae tanks. This is important as every part of the prototype can work sequentially and the measurement can be done correctly. For that, two code scripts were written using the Arduino IDE and Visual Studio code with a Python compiler software for, respectively, controlling the ESP-32 and saving the data collected by the prototype.

ESP-32 control code

The Arduino IDE was used due to its large number of libraries, making it easier to write a control code for the ESP-32, as SPI protocols and I^2C communication protocols have to be used, for example. Because the Arduino IDE is an environment that uses a variant of the C++ programming language, each variable and object has to be defined beforehand. The libraries included were: "`SPI.h`", "`Arduino.h`", "`math.h`", "`esp_sleep.h`", "`Wire.h`" and "`Adafruit_ADS1X15.h`". Before writing the setup code, the functions "`writePot`", "`A230`" and "`A300`" were defined to control the potentiometers that define the LED intensity and as the calibration functions of the LEDs, respectively.

To avoid consuming too much energy between every measurement, the ESP32 is put in deep sleep. This way, all the code can be written in the "`setup()`" function as every time the microcontroller wakes up, this function is called. After defining each pin that is going to be used as input or output in the "`setup()`" function, the SPI communication starts and LEDs are turned. SPI communication also lets the signal to be amplified to be also controlled, and the peristaltic pump is turned on via a potentiometer. The voltage across the terminals of the peristaltic pump is increased for 9 seconds. The SPI communication can be turned off, and the Serial monitor can be turned on with a baud rate of 115200. The I^2C communication protocol is started by defining the SCL and SDA pins and initializing the an ADC. The ESP32 will save the 3000 values from the ADC for both LEDs and average this array with a sampling rate of 100Hz. The voltage measurements are done separately so that each LED/photodetector setup in the sensor don't influence each other. After this, the respective nitrate concentrations are determined and written in the serial. The SPI communication is restarted to turn off the LEDs. After the LEDs are turned off, the microcontroller is put in deep sleep for a certain amount of time, typically, 30 minutes. This whole cycle is repeated. The whole code described is in Appendix D, section D.1.

Visual Studio code

To save and analyze the data that was being registered by the sensor, the microcontroller needs to communicate with another device. This could be done with another microcontroller or a computer. Communication is, in principle, going to be done via wireless. In the laboratory, this is not needed. Communication can be done via USB-C and connected to a computer near the sensor to facilitate this process. Moreover, a Python script was written to register and save the data coming via the USB-C cable so that this data is saved in a text (txt) file and, with that data, a graph is drawn and updated in real-time.

Because two processes are happening in parallel, the graph and registering the data, a thread was created so that both process's could be done at the same time. Some python libraries had to be imported: "`serial`", "`matplotlib.pyplot`", "`datetime`", "`threading`" and "`time`". To register and read the data from the USB-C cable, the function "`read_serial`" was defined.

After starting the thread for the function "`read_serial`", the plot is drawn with the lists: "`tim`" and "`ls`" that are updated each time the serial is read. The "`ls`" list is only updated with the concentration determined by the LED with the wavelength of $\sim$230nm, but this could be changed as needed. The whole code is represented in Appendix D, section D.2.

3. Experimental Results

3.1. Absorbance Spectrum

The results obtained for the spectra of absorbance are represented in Figure 3.1. It was impossible to show all the results for $\lambda < 250$nm, because for concentrations higher than 30ppm for NO_2^- and 120ppm for NO_3^-, the optical signal intensity variation between the concentrations tested was smaller than the resolution of the spectrometer.

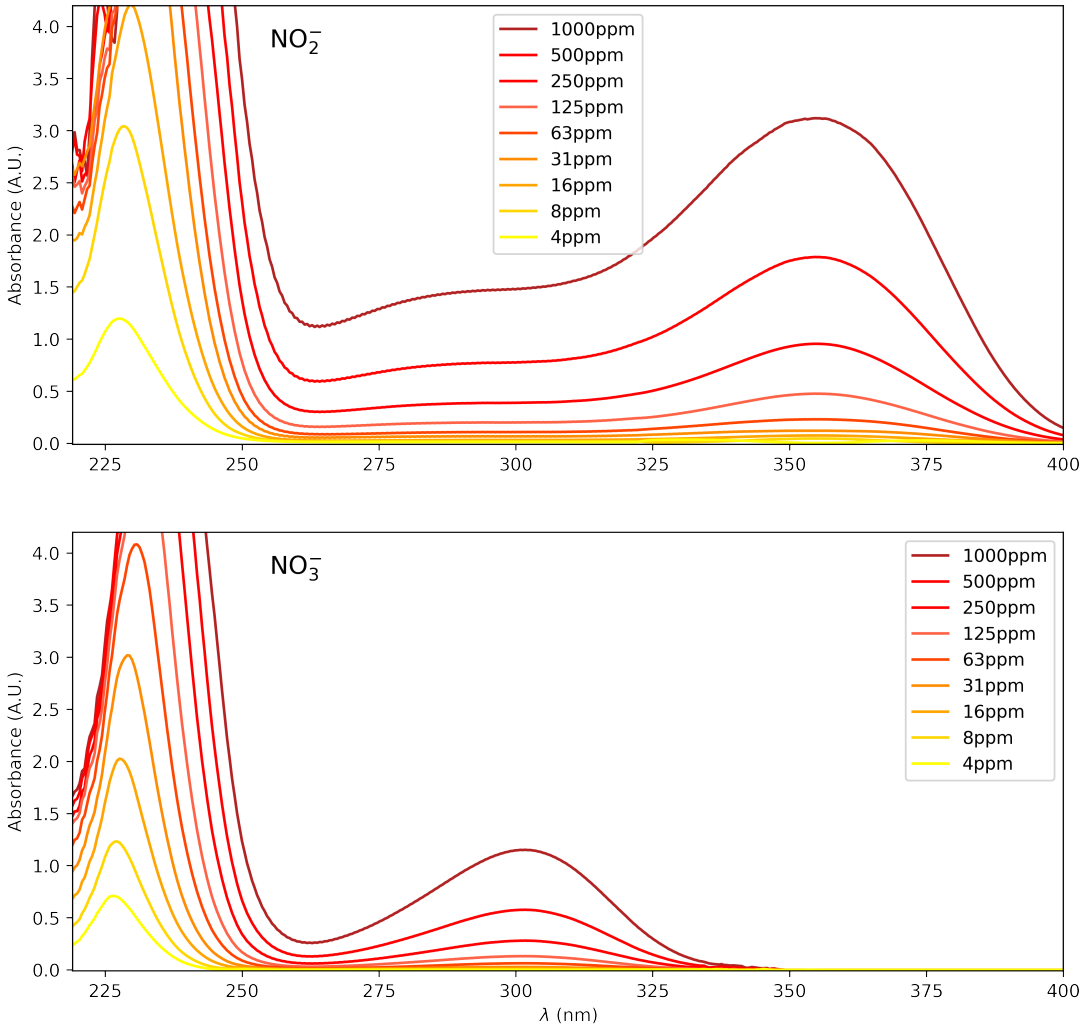

Figure 3.1: Absorption spectra of NO_3^- and NO_2^- observed for concentrations between 4 and 1000ppm

For NO_3^-, two absorption peaks can be observed: the first around ∼230nm and the second at ∼300nm. The first and second wavelength peaks agree with what was observed by other spectroscopy analyses of NO_3^- done [64, 80]. For NO_2^-, its possible to observe three main peaks: first peak at ∼230nm, second peak at ∼364nm and third peak at

$\sim$300nm. This third peak is less noticeable than the other two, so the analysis will focus on the first and second peaks. This behavior also agrees with what was observed by other spectroscopy analyses of NO_2^- [81, 82], although both were able to observe the third more clearly. Similar to NO_3^-, the observed peaks show the same spectral behavior and differences between them, with both peaks showing higher absorbance levels for NO_2^-. Comparing both peaks, it can be easily seen that the first peak is way more sensitive to the presence of NO_3^- than the second peak as by Figure 3.2, the first peak seems to have a logarithmic tendency. By tracing how the intensity of the light profile, $p = I/I_0$, decreases with an increase in concentration, it is possible to observe that for the whole range of concentrations detected, the first peak is more sensitive to absorbance than the second peak.

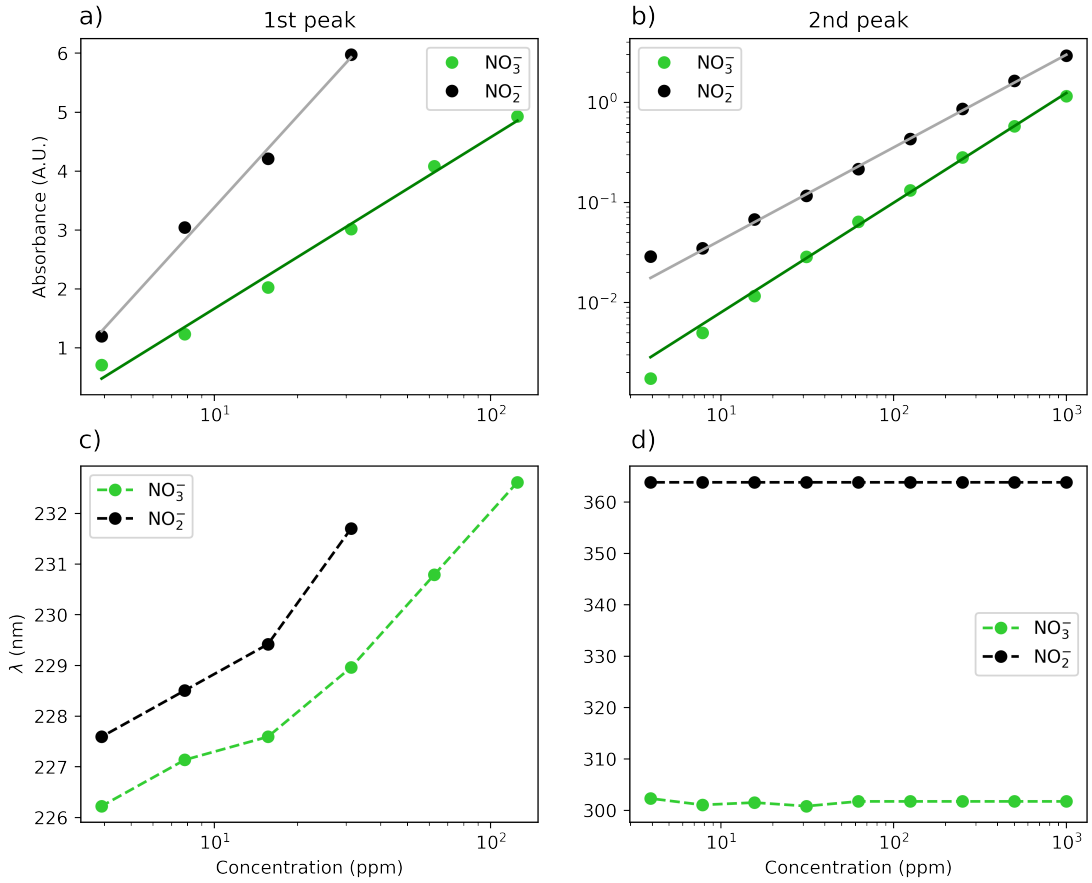

Figure 3.2: Absorbance (a) and b)) and wavelength shift (c) and d)) for both peaks with increasing concentration of NO_3^- and NO_2^-

For the first peak, it is possible to see a **bathochromic shift** in NO_3^- and NO_2^- (Figure 3.2, c)). This may result from an intermolecular interaction between the NO_3^- molecules that shifts the molecular energy states [83]. No shift in the range of concentrations analyzed is noticeable for the second peak.

It is possible to compare the results in Figure 3.1 with the spectra obtained by dissolving gaseous nitrogen in deionized water (figure 3.3). Just like what was observed in 3.1, it has a verified a peak of absorbance at ∼230nm.

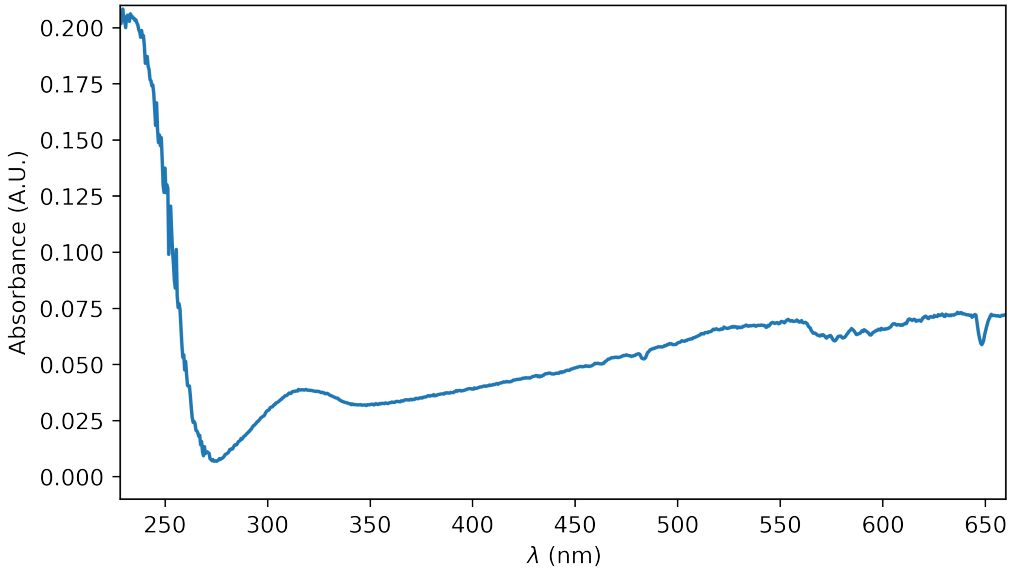

Figure 3.3: Absorbance spectra of dissolved nitrogen in water

In general, sodium nitrate is the primary reference for calibrating and building these nitrate sensors. This way, the presence of only two absorbance peaks motivates using LEDs instead of lamps to develop a lower-cost sensor. If a photodetector is going to be used, the voltage, V_{ph}, needs to be as sensitive as possible to the decrease of intensity made by the absorbance of the chemical species. Because the interval of voltage to be detected is limited, to maximize the decrease in light intensity due to the presence of NO_3^- and NO_2^-, the ratio $V_{ph}/V_{ph_0} = f$ needs to be maximized.

$$f = \frac{V_{ph}}{V_{ph_0}} = \frac{\int_{\lambda_{min}}^{\lambda_{max}} I(\lambda, c) \times F(\lambda) d\lambda}{\int_{\lambda_{min}}^{\lambda_{max}} I(\lambda, 0) \times F(\lambda) d\lambda} = \frac{\int_{\gamma} I_A(\lambda, c) \times F(\lambda) d\lambda + \int_{\beta} I_r(\lambda) \times F(\lambda) d\lambda}{\int_{\gamma} I_A(\lambda, 0) \times F(\lambda) d\lambda + \int_{\beta} I_r(\lambda) \times F(\lambda) d\lambda} \quad (3.1)$$

For equation 3.1, the intensity of the light source was separated between the regions where absorbance will exist and where it will not, $I(\lambda, c) = I_A(\lambda, c) + I_r(\lambda)$, and $F(\lambda)$ is the integration function of the photodetector. This way, because our window of detection of voltages is limited, we want to decrease factor $\int_{\beta} I_r(\lambda) \times F(\lambda) d\lambda$ so that this bias voltage wont be added by the photodetector.

This way, the sensor's sensitivity can be increased by decreasing. decreasing the intensity of the light source where no absorption is observed or choosing a photodetector with

a smaller integration region in these specific regions. On the contrary, increasing the intensity of light where absorption exists and maximizing the integration area of this region will enhance sensitivity if $r \neq 0$. Since the absorption is limited (only two peaks), using LEDs that match these wavelengths is the easiest and most cost-effective way to optimize sensitivity. This is seen in Figure 3.4, where a uniform integration of the spectra was assumed. Comparing an integration for the full (from 200 to 600nm) and for half range (from 200 to 400nm), it is clear how using a light source with similar emission spectrum as the absorbance wavelengths of the chemical species is essential to observe more significant absorbance values and, consequently, more extensive sensitivities.

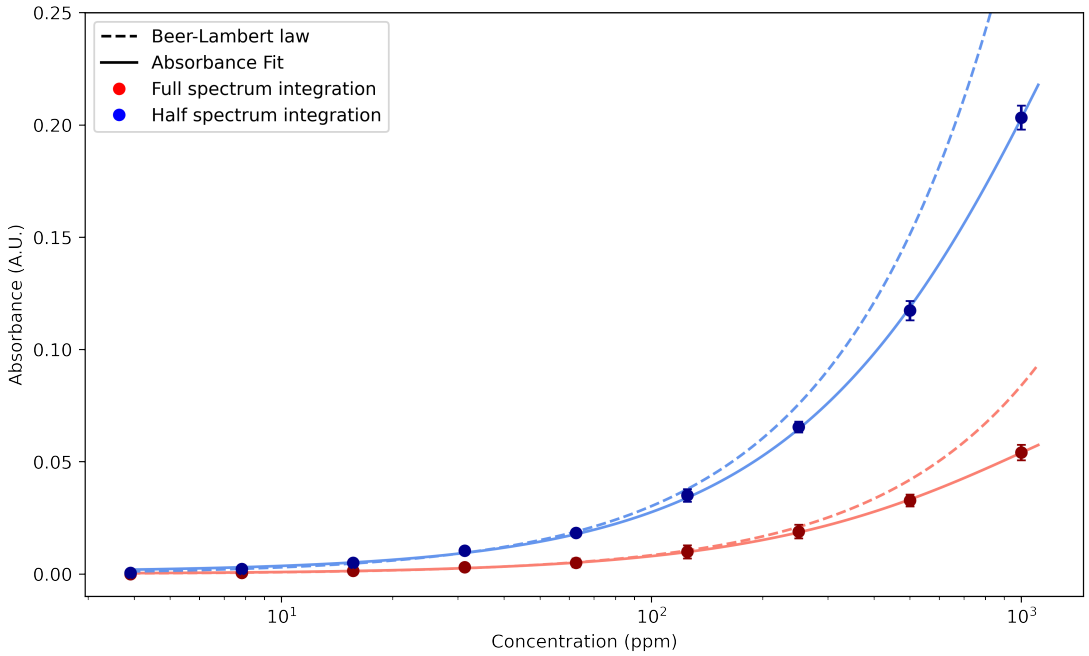

Figure 3.4: Integrated intensity for full and half spectra, comparing the Beer-lambert law with 3.2

Figure 3.4 compares what is expected by taking in account only Beer-Lambert law, equation 2.4, with equation 3.2, that takes into account the integration of the spectra by the photodetector where there is also no absorption, I_r. It is possible also to see how for higher concentrations, these considerations should be taken in account when predicting the absorbance behavior as the Beer-Lambert law starts diverging.

$$A_r = \ln\left(\frac{I_A e^{-\mu c} + I_r}{I_A + I_r}\right) \tag{3.2}$$

The biggest problem with using an LED instead of a lamp in this situation is how deep UV LEDs, below 300nm, are rare and still in development. These do not have the same optimizations as IR and VIS LEDs and can carry problems of fast deterioration as the

ones based on GaN [84] and low external quantum efficiency [85], for example. These are not the best characteristics for building a wirelessly controlled sensor, as they require constant LED maintenance. If only the sensor takes measurements between big time intervals, this deterioration problem can be delayed.

3.2. Optical Path Determination

To develop an optical sensor based on how light is transmitted through a medium, the optical path length is integral to understanding how much the optical signal will interfere with the medium. This way, because the two wavelengths chosen to explore (near $\sim$230nm and $\sim$300nm) react differently for the same concentrations (Figure 3.1), it is expected that both have different optimal optical paths.

3.2.1 Optical path for LED1 setup

As expected, near $\sim$230nm, increasing the optical path length distance leads to higher absorption. This occurs because as the optical signal interacts with more particles in the medium, more photons get absorbed: the increase in length of the optical path increases the number of absorbing particles. This sets up an essential step in developing a sensor as adjusting the optical path length can be used to increase the sensor's sensitivity and define its operational range.

Figure 3.5 represents the absorbance spectra relative to water, captured for every optical path tested in the 5 to 30ppm concentration range of dissolved nitrates. It is easy to verify that the increase in optical path leads to an increase in absorbance. Comparing the peaks between the optical paths for the same concentrations, it is possible to observe that the increase in the optical path also leads to the redshift of the absorbance peak. The redshift must be associated with the total number of particles the optical signal interacts with, not just with the concentration of NO_3^- . By identifying the absorption peak, it is possible to observe that linearity is lost as the concentration and optical path increase. This is not the same problem observed in section 3.1 where the integral of the range not absorbed starts to be higher than the one absorbed. This behavior must be intrinsically related with to the molecules just as the redshift.

In figure 3.6, the spectrometer results were defined by integrating the spectra of the LED for every concentration and deionized water. For both detection methods, photodetector and spectrometer, the absorption of the medium also increases with the increase in optical path. This is also according to what was expected. The photodetector approach

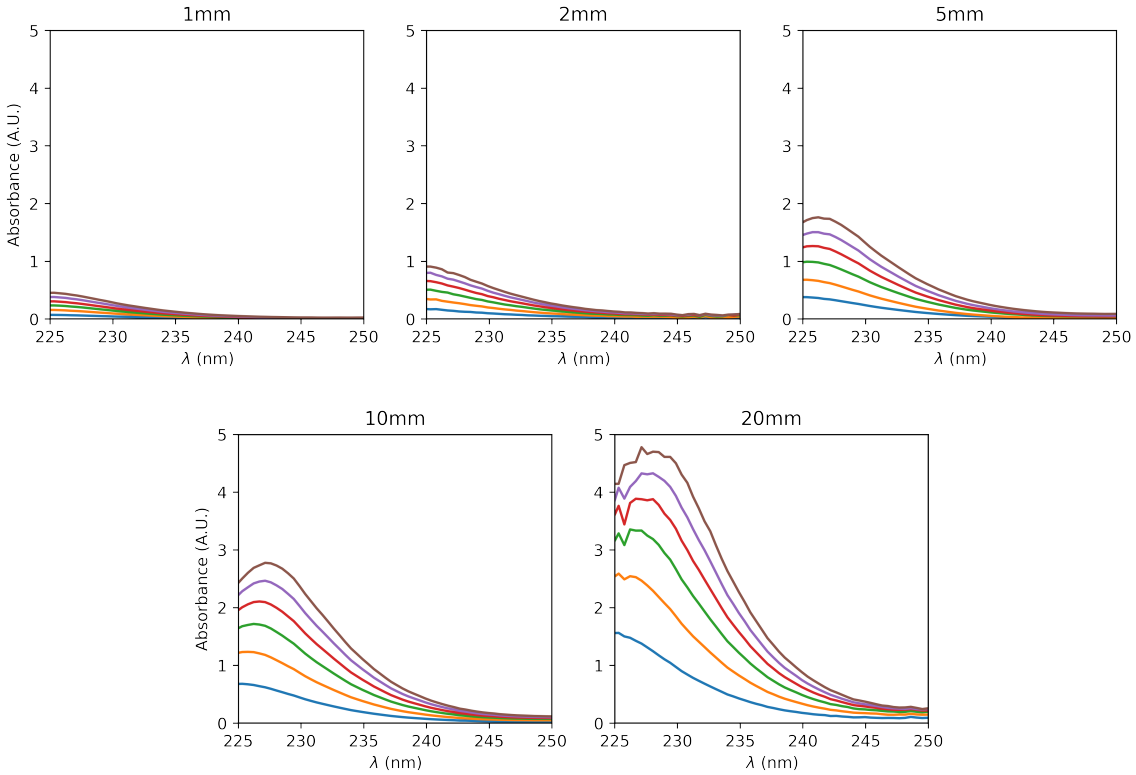

Figure 3.5: Absorbance spectra near 230nm for different concentrations and optical paths

shows less signal variation for the same concentrations than for the spectrometer. This makes sense because the spectral responsivity of the respective photodetector is not uniform, especially between the wavelength range of 225 and 250nm where the normalized responsivity goes from 0.125 to 0.625. Observing linear behavior for optical paths lower than d=10mm is possible. For the optical path of d=20mm, a logarithmic fit was used for both setups. This is explained by the fact that the intensity of the absorbed range is as small or smaller than the range that was not absorbed by the medium.

Because the analogic signal will be converted to a digital signal by a microcontroller analog-to-digital converter with 12 bits, the minimum voltage variation is given by $V_m = 3.3/2^{12} \approx 0.8$ mV. The voltage output of the photodetector will decrease with the increase in concentration, this way, the variation of the signal's voltage is given by $\Delta V = V(c) - V(c + \Delta c)$. Solving equation 3.3 gives the minimum concentration variation that can be detected by the photodetector for each optical path.

$$\Delta V(c, \Delta c) = V_m \tag{3.3}$$

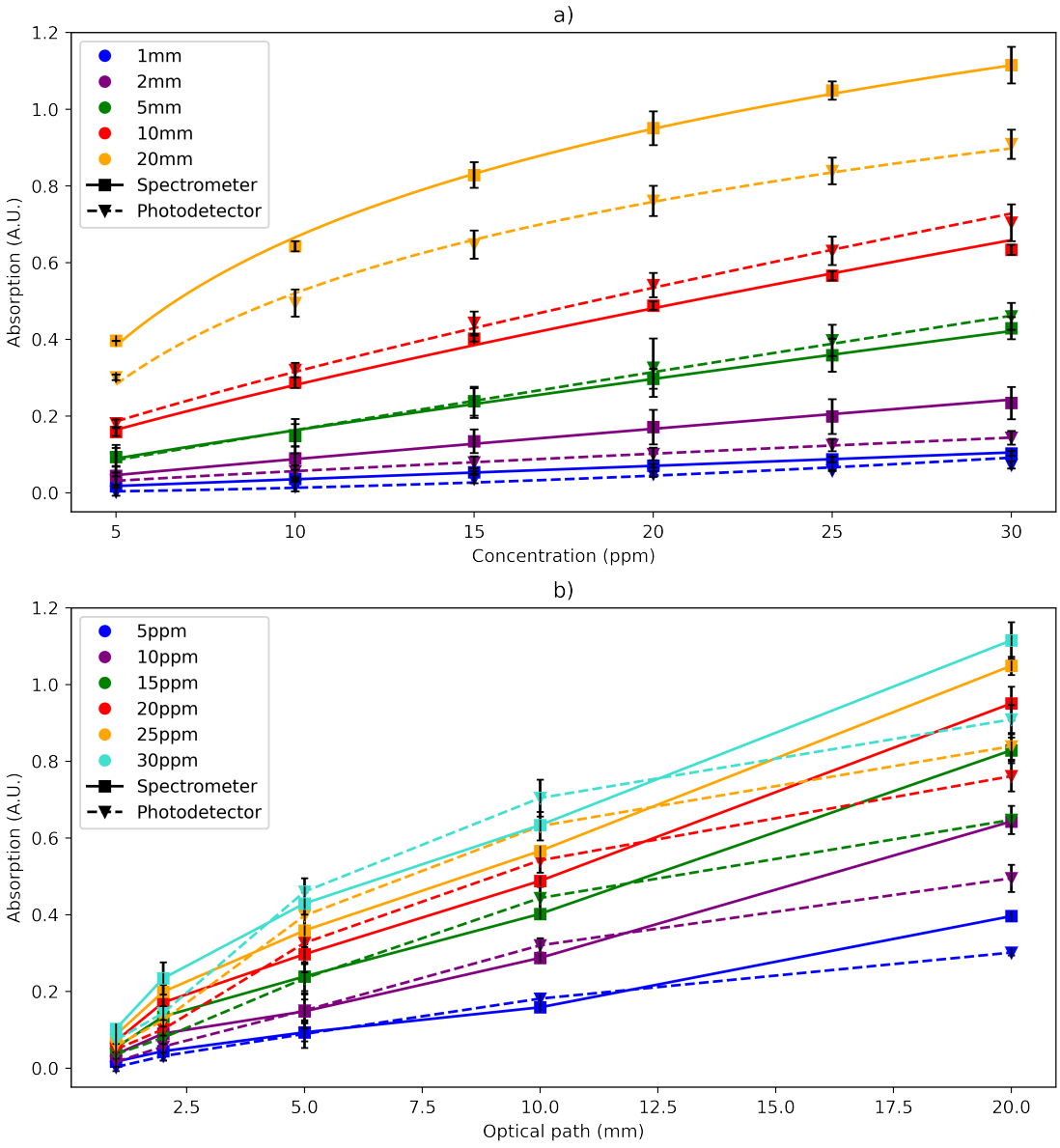

Figure 3.6: Absorption for LED1 using a spectrometer and the respective photodetector for different optical paths (a)) and concentrations (b))

For the concentrations tested $V_m \ll \Delta V$, so $\Delta V \approx (dV/dc)\,\Delta c$. The minimum concentration variation that can be detected because of the number of bits of the ADC is given by equation 3.4.

$$\Delta c = \frac{V_m}{\left(\frac{dV}{dc}\right)} \tag{3.4}$$

This is shown in Figure 3.7 for every optical path tested based on the experimental fits shown in Figure 3.6. It is possible to observe that although for an optical path of 20mm the whole voltage variation in the concentration range explored is higher, as the concentration

increases, the minimum concentration variation increases more than for an optical path of 5 and 10mm. Beyond the fact that the decrease in intensity of the optical signal due to the increased concentration leads to the transparent part of the spectrum being as big as the absorbed part, the increase in concentration also leads to a redshift. Because the photodetector has a steep increase in responsivity in the same wavelength range where the redshift occurs, some of the voltage output decreases end up being mitigated, muffling the minimum concentration variation that could be detected. The results in Figure 3.7 corroborate the option of choosing an optical path of 10mm for the concentration range of 5 to 30ppm, as the respective distance that best suits a smaller concentration variation that can be detected throughout the whole procedure. However for a distance of 5mm, the results are similar to the 10mm results and could also be chosen as the optical path. For d =10mm, the resolution varies between $\approx$ 0.01 and 0.03 ppm and for an optical path of d =20mm, the resolution varies between $\approx$ 0.005 and 0.05 ppm.

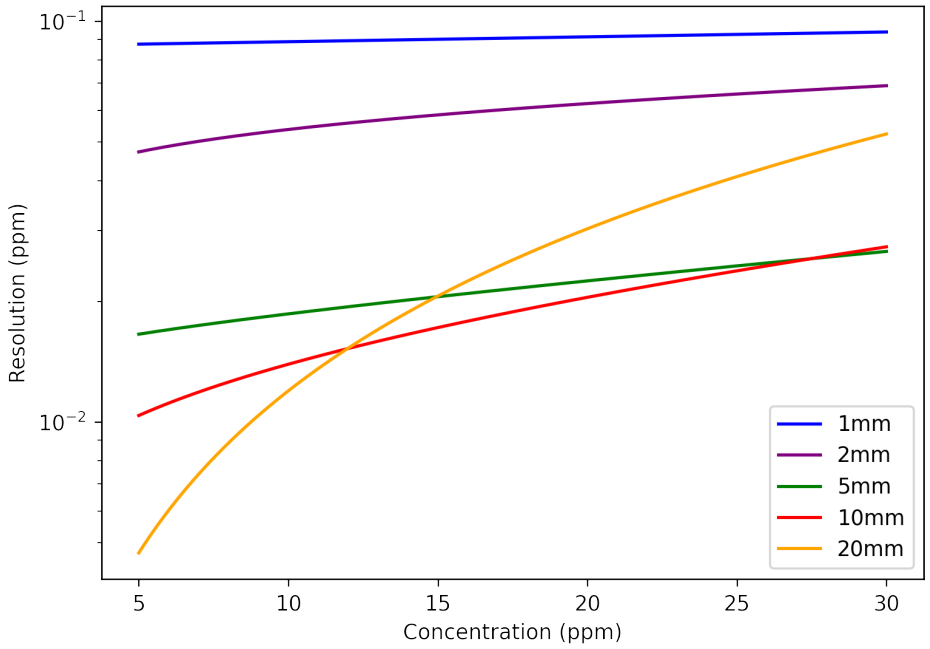

Figure 3.7: Minimum concentration variation that can be detected for every optical path for LED1

3.2.2 Optical path for LED2 setup

For the identified peak at $\sim$300nm, it was not possible to test the optical path of 5mm, as the optical signal had a width higher than the cuvette used, even when using the LC7 lens, and it was hard to fix the LED2. Using a cuvette forces it to be taken away and put in place again for every concentration, allowing different parts of the optical signal to be

transmitted through it. This problem could have been solved if the support could fix the cuvette when LED2 setup was used.

From Figure 3.8, it is possible to observe the results obtained for all optical paths tested. The results agree with the fact that increasing the optical path leads to an increase in the absorption values obtained. These results have the same justification as what was discussed in subsection 3.2.1. It is easy to conclude that the results also do not follow what was expected from the Beer-Lambert law: for the same concentrations, for an optical path of 10mm, the absorption does not reach half of the values from 20mm although the distance is half. It should be expected that the increase in optical path only leads to increased interactions between light and the molecules. From what is observed, this kind of procedure idealizes the interaction between the light and the particles, where each particle does not interact with any other, which might not be sufficient to explain the results.

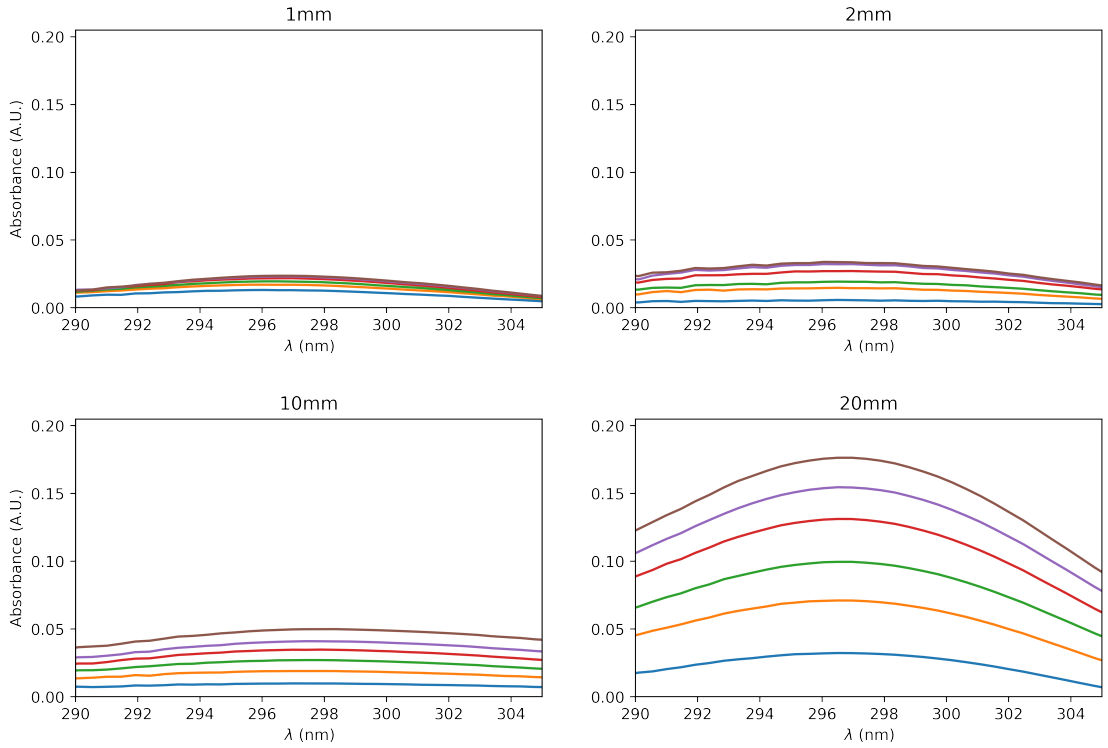

Figure 3.8: Absorbance spectra near 300nm for different concentrations and optical paths

Figure 3.9, shows how for every optical path tested, the integrated absorption of the spectra obtained in the spectrometer and the data measured with the photodetector has a linear behavior with the increase in concentration. Compared with Figure 3.6, it confirms how the absorbance at ∼300nm reaches lower values. For the optical path of 20mm, the error of the measurements is due to the setup used, which requires a precise alignment and even careful handling, which could lead to misalignment and interfere with the intensity of

the detected optical signal. One big obstacle had to do with the pumping intensity of the peristaltic pump that, if big enough, would create undesired movement due to the flow of water through the tubes and flowcell, even when the setup was immobilized in the optical workstation. This vibration would misalign the photodetector and the LED, as well as the LED and the support holding the lens. It is also possible to observe that the results from the photodetector and the spectrometer are closer to $\lambda \sim$300nm peak than for $\lambda \sim$230nm.

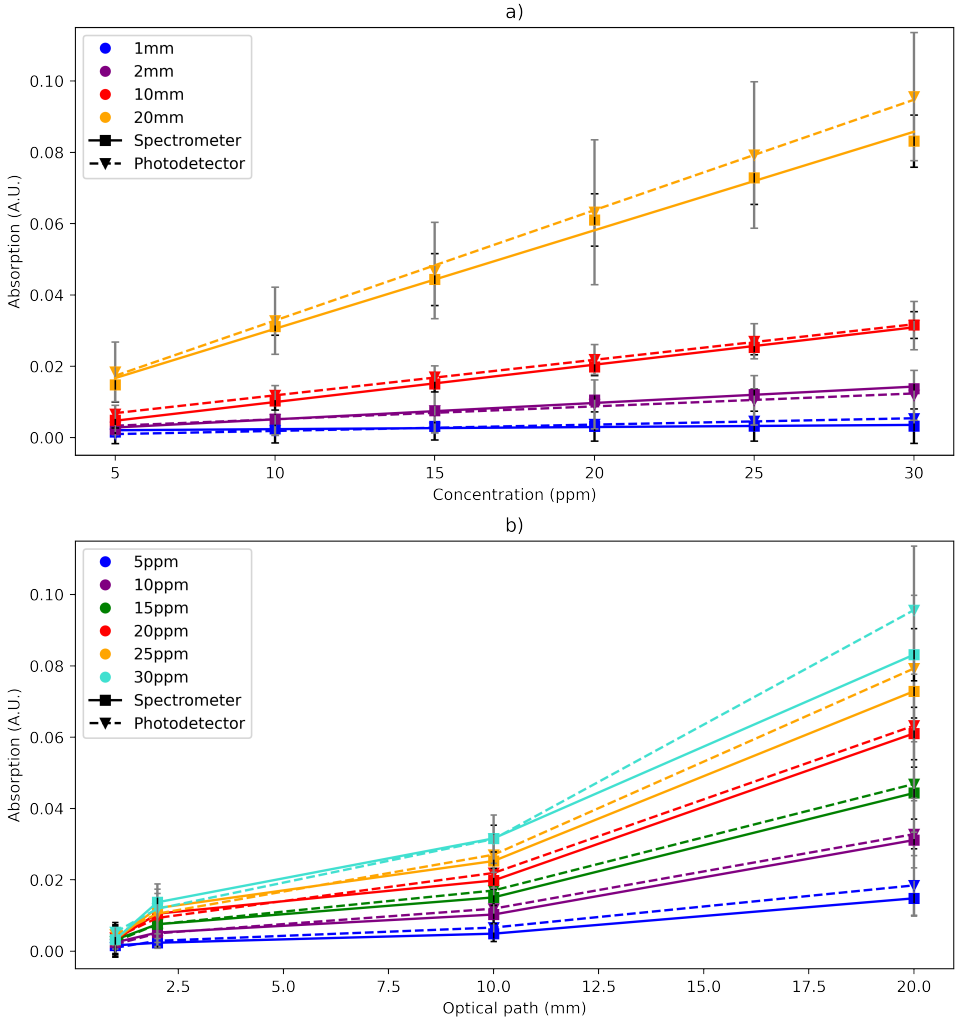

Figure 3.9: Absorption for LED2 using a spectrometer and the respective photodetector for different optical paths (a)) and concentrations (b))

Contrary to what is seen in Figure 3.6, the photodetector absorption measurements showed higher values than those from the spectrometer. This could be due to the spectral responsivity of the GUVV-T21GH photodetector, which has higher values at wavelengths where light is absorbed and lower where there is no absorption. This gives a more sensitive response from the photodetector than if the range not absorbed from the emission spectra of LED2 had the same responsivity as the range where absorption can be detected.

The results in Figure 3.10 show the maximum resolution achievable when using the whole voltage range of the microcontroller's ADC. Due to the slight voltage variation measured for the tested concentrations, only linear behavior is observed. This leads to a constant resolution for the range of concentrations tested for all optical paths. The higher the optical path, the better the sensor's resolution without compromising the range, contrary to what was observed for $\lambda \sim 230$nm. For the optical paths tested, the higher, the better. Therefore, 20mm is the best option for an optical path as the resolution achieved is about 0.08ppm while for 10mm, for example, is 0.25ppm. If only one flowcell is to be used for the sensor, consequently, only one optical path for both LEDs, the best option would be an optical path of 10mm, as it is undoubtedly the best for LED1 and is not far away from the results for 20mm for LED2.

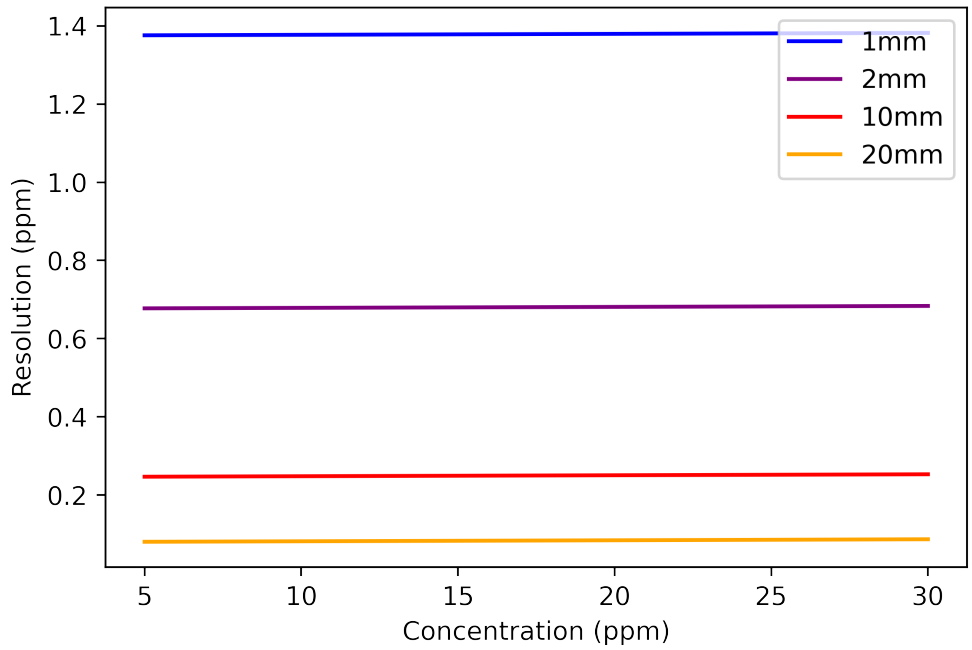

Figure 3.10: Minimum concentration variation that can be detected for every optical path for LED2

3.3. Prototype development

By having LED1 and LED2 setups together, it is possible to develop a sensor prototype that includes the circuit that will control the different parts of the sensor and a first design of how the setups will be implemented together cost-effectively. In figure 3.11 is represented a block diagram of the different systems can be implemented and how they can communicate.

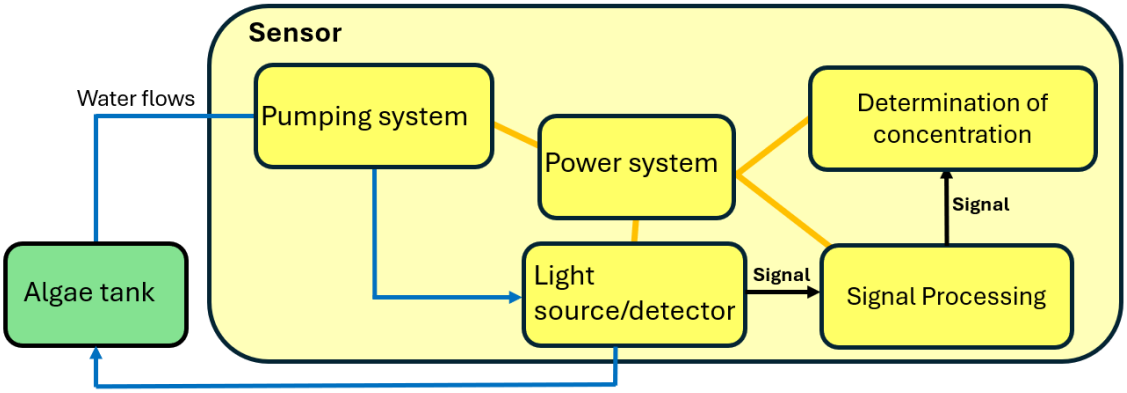

Figure 3.11: Block diagram of the sensor and respective control systems

3.3.1 Circuit developed

By choosing an optical path of 10mm for both LEDs, it is now possible to develop the circuit that will control them. In principle, the sensor will have to pump water from a reservoir, the LEDs will then have to light up, and the photodetectors will detect it so the microcontroller can analyze the signal. It is possible to separate these procedures into three different circuits: LED control circuit, filter/photodetector circuit and peristaltic pump control circuit,

LED control circuit

Both LED/photodetector setups used for NO_3^- and NO_2^- detection require different signal treatments as problems must be overcome.

Due to LED1's slight viewing angle, the photodetector saturation is easily achievable with small electric currents ($<$5mA) and requires sensitive control of the current being supplied to the LED. As an example, if the impedance of the LED, $R_L \sim 10^3\Omega$, was way more significant than that of the potentiometer to be used, a simple voltage divider with resistors parallel to the LED would be enough to control its intensity as the voltage supplied to the LED, V_S, is given by equation 3.5. V_S is the voltage the transformer supplies to the circuit, and R_1 is the resistance that limits it.

$$V_L = \frac{V_s}{R_1 + \frac{R_L R_P}{R_L + R_P}} R_P \approx \frac{V_s}{R_1 + R_P} R_P \tag{3.5}$$

The main problems of digital potentiometers are related to their nature and the energy they dissipate. For digital potentiometers with significant resistance values, bigger than $10^4\Omega$, the main limiting factor is the maximum current which is related to their supply voltage, typically $\sim$ 1V. Only small currents of $\lesssim 10\mu$A can be applied [86]. For minor resistance, the current still is a limiting factor as smaller resistance values with currents minor than 10mA end up overheating the digital potentiometer, damaging itself and the devices next to it. This forces the use of currents below that limiting factor, making using a simple voltage divider circuit impossible.

A more complex approach could be using resistors in series connected to a buffer circuit to separate the impedance of the LED. This is ideal when supplying the LEDs with currents of $\sim$ 10mA, but LED2 needs a current of at least 100mA so the respective photodetector can detect an optimized signal. The approach to solving these problems was using a voltage regulator (figure 3.12), LM317, and a digital potentiometer, MCP42151. The voltage regulator LM317 has an input voltage range of 4.25 to 40V [87]; an output voltage range adjustable from 1.25 to 37V and an output current greater than 1.5A. As the digital potentiometers force a lower limit for the resistor values, the LM317 forces an upper limit because of the noise current given by the ”ADJ” pin which is between 10 and 100 μA. Using resistors in the order of the 100 kΩ would add noise voltage term in the order of $\sim$ 1V. So a resistor with approximately 1kΩ will be needed.

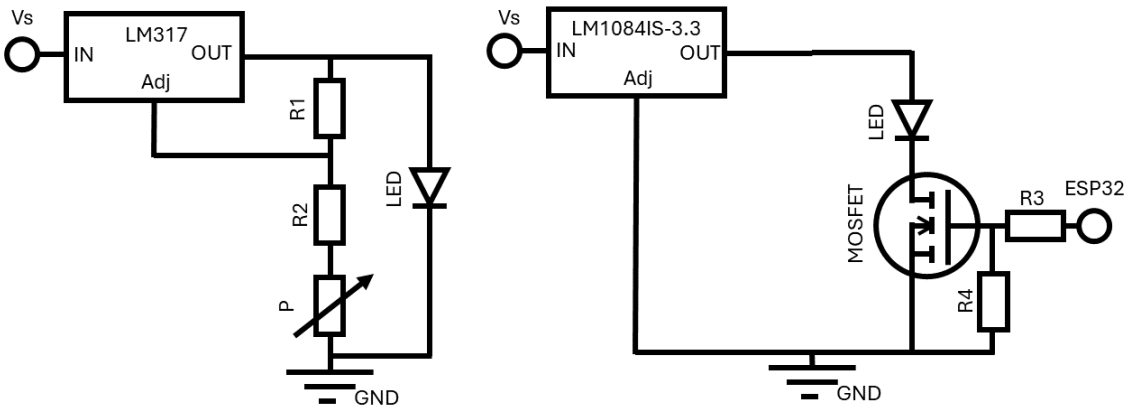

Figure 3.12: Circuit used for the supply of the LEDs. The left circuit is used for the measurement LEDs as a precise calibration is needed. The right circuit is used for the LED to measure the presence of potential contaminants

For the LM317, between the ”ADJ” and ”OUT” pin is recommended a resistor of 240 Ω

to keep a difference of 1.25V between the terminals, but to maximize the control of the LED, the bigger this value, the lower each step voltage between each position of the potentiometer: it was possible to verify that using a resistor of 900 Ω is still a valid option to keep the 1.25V between the terminals [87]. By varying the position of the potentiometer, it is possible to vary the voltage supplied to the LED. As mentioned, the potentiometer's terminals only have a maximum of 3.3V. For the measurement of LEDs, a precise calibration of their intensity is needed, so the resistance values of R1 and R2 will define the voltage interval between the terminals of the LED: V_{max} and V_{min}. An LED will be also used for qualitative measure of possible contaminants, LED3 (VAOL-5EUV8T4), For this LED, instead a LM317, it is easier and enough to use a LM1084IS-3.3 that directly outputs a constant voltage of 3.3V.

$$V_{min} = V_r \left(1 + \frac{R_2}{R_1}\right) \tag{3.6}$$

$$V_{max} = V_r \left(1 + \frac{R_2 + P_{max}}{R_1}\right) \tag{3.7}$$

By changing the value of the potentiometer, we can control the intensity of the LED. The parameters expected to be seen for each LED are shown in Table 3.1. To turn on or off LED3, the MOSFET is the PSMN5R0, which controls both states by supplying the gate of the MOSFET with voltage of 3.3V from the ESP32.

Table 3.1: **Parameters expected for the circuit built for LED supply**

LED	**R1 (Ω)**	**R2 (Ω)**	**V$_{min}$ (V)**	**V$_{max}$ (V)**
LED1	820	1800	3.99	7.29
LED2	820	2200	4.6	7.9
LED3	$\emptyset$	0	3.3	3.3

Filter/photodetector circuit

The 3.3V output pin of the ESP32-C6-DevKitC-1 supplies each photodetector. For the signal treatment, the filter used for all LEDs is a low-pass Sallen-Key active filter with a cutoff frequency of 100mHz and a decay of -40dB/decade for filtering (a preliminary study of the filter is described in appendix B). This is implemented right before the microcontroller detects the signal where R1=1MΩ, R2=2.2MΩ, C1=680nF and C2=2.2µF. The amplification circuit displayed in the circuit on the right in Figure 3.13 is only to be implemented for the GUVV-T21GH photodetector because, for the preliminary studies done, even with

a lens, the detected signal is still low, $<$0.5V. The op-amp used is an AD823 which can be supplied with $\sim$12V coming from the supply and has an input voltage below the GND when supplied with just V+=Vs and V−=GND. The amplification is given by equation 3.8 and the signal filter by equation 3.9, where $\tau_{ij} = R_i C_j$.

$$V_O = V_i \left(1 + \frac{P}{R_3}\right) \tag{3.8}$$

$$\left|V_O(\omega)\right| = \frac{\left|V_i(\omega)\right|}{\sqrt{\left(\omega^2 \tau_{11}\tau_{22} + 1\right)^2 + \left(\tau_{11} + \tau_{21}\right)^2 \omega^2}} \tag{3.9}$$

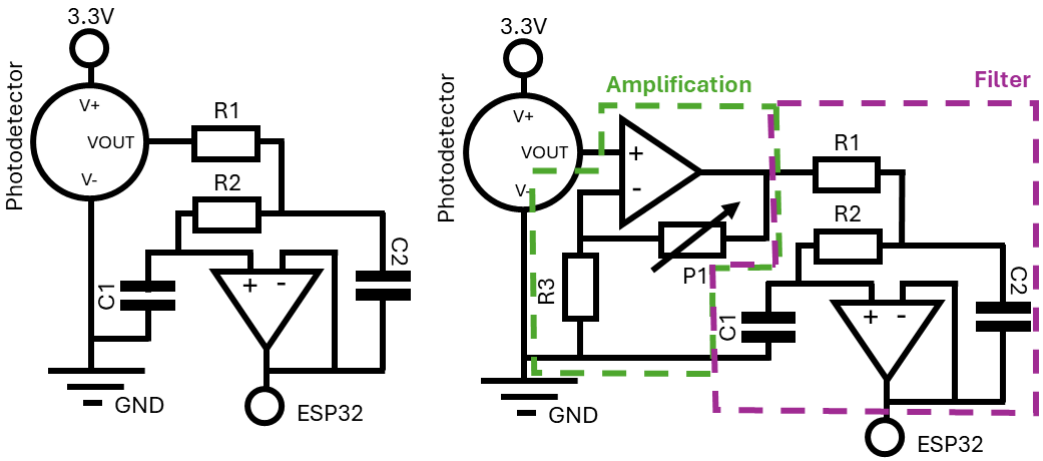

Figure 3.13: Circuit used to treat the signal coming from the photodetector. The left circuit is used for the TOCON_ABC1 photodetector; the right circuit is used for the GUVV-T21GH photodetector

.

It is expected to observe noise in the circuit. The first is coming from the supply of the LED, which will affect the luminosity of the optical signal and, consequently, the signal detected by the photodetector. Noise coming from the supply of the photodetector is also expected, just as noise from the power supply that is responsible for the supply of the op-amps and digital potentiometers. This noise can be removed by bypass capacitors near these devices supply pads on the built-in PCB. Electromagnetic noise from the circuit is also expected to interfere with the VOUT of the photodetector as inductance and capacitance phenomena are expected, especially when using PCB as the electric routes are closer to each other: space between the paths of $\sim$1mm.

Peristaltic pump control circuit

The ESP32 board also controls the peristaltic pump, which circulates water containing dissolved nitrates and nitrites. The pump operates up to 12V with approximately 0.4A. The voltage across its terminals is regulated by the LM317 voltage regulator combined with one of the potentiometers embedded in the digital potentiometer MCP42151 (figure 3.14). A MOSFET is placed so the peristaltic pump can be turned on or off.

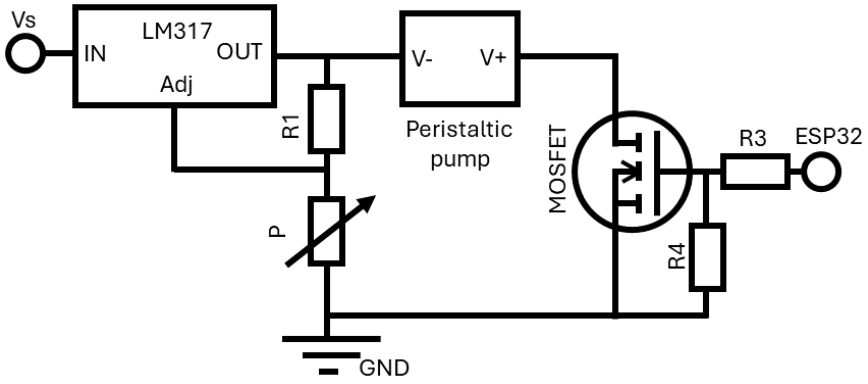

Figure 3.14: Circuit used to control the peristaltic pump.

The digital potentiomenter MCP42151 has two potentiometers embedded. Hence, two electronic components are needed for the whole circuit. Their general connections are displayed in Figure 3.15 where the MO and CLK are the ”Master Output” and ”Clock” pins of the microcontroller. ”CSx” corresponds to a generic ”Chip Selection” pin that is used to turn the communication on or off. The entire circuit is in Appendix C, figure C.1.

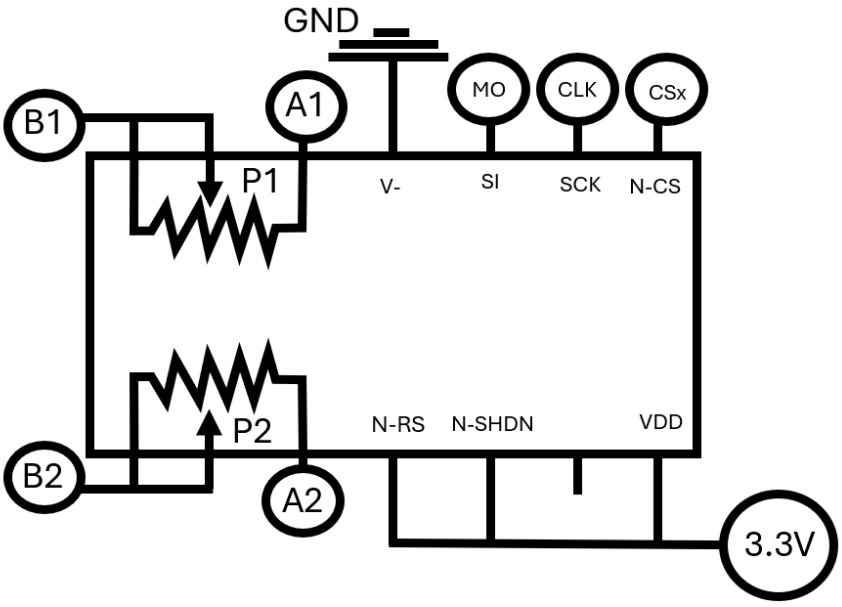

Figure 3.15: Circuit used to control the peristaltic pump.

3.3.2 Sensor design

A sensor with different optical paths for each LED/photodetector setup could be achieved by having two flow cells serially connected, as it is expected that the absorbance peaks have different optimal optical paths for the concentration ranges the setup will explore. Even if it was not possible to find in the market a flow cell with a particular optical path or if these were too expensive, to force a certain optical path, a setup like the one in Figure 2.6 could be implemented if the mirror was not centered, giving more space to implement the other LED/photodetector setups with only one flow cell being used. This approach would be too complex, as achieving alignment for one of the LEDs would be difficult since it would imply an angle of incidence not perpendicular to the plane of the flow cell. This would imply a deviation of the optical ray due to the medium's refractive index, which can vary depending on the concentration of other chemical species. A more straightforward approach can be implemented as shown in figure 3.16 where each LED is aligned with the photodetector, with the angle of incidence of the optical ray being perpendicular to the flow cell walls.

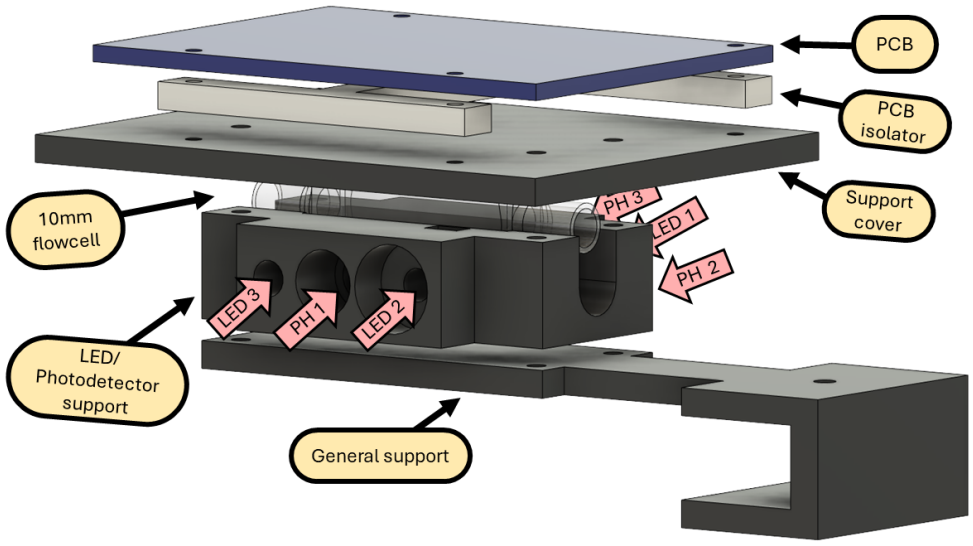

Figure 3.16: First prototype of the nitrate/nitrite sensor

The photodetector and the LEDs were alternated on each side to avoid any unwanted excitation of the photodetectors from the LEDs, except their respective LED. Another valid approach to this problem would be turning on the LEDs and the measurement at different instants, one pair LED/photodetector after the other. This would have the downside of increasing the sensor's response time.

Because this sensor has a fluid system implemented, the risk of damage to the circuits due to possible water leakage is high. This way, the PCB was placed as far/isolated from the fluidic system as possible. Because the prototype shown in Figure 3.16 needs to be placed vertically to avoid the accumulation of bubbles in the flow cell, a cover needs to be fixed to the LED/Photodetector support to keep it in place. This implies the use of screws that could damage the PCB by short-circuit if not for the use of a PCB insulator to avoid possible contact.

The PCB was designed so that the LED and photodetectors contacts could reach it without difficulty and be attached/detached easily. Each part of the full circuit was designed in the PCB so that there was a clear distinction between them, while keeping the whole board as tight and organized as possible. This is represented in figure 3.17.

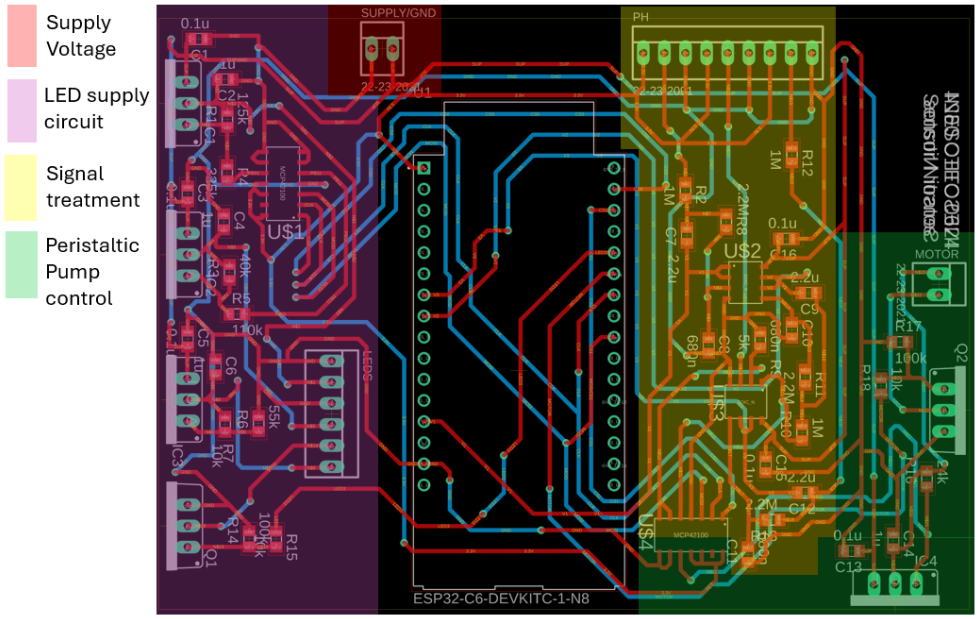

Figure 3.17: PCB design with each part of the circuit represented in colors

3.4. Signal testing

3.4.1 Electronic noise analysis

One important consideration is that before section 2.4, the LEDs were powered by a low-noise power supply. However, the developed sensor must operate with a cheap transformer that outputs 12V with higher noise levels.

In Figure 3.18 it is possible to understand that the noise is in fact reduced for both LED setups, after adding the filter and bypass capacitors. It should be noted that although the microcontroller ADC, theoretically, should have 12bit resolution and, consequently,

expected to have a resolution of 0.8mV for a window of 3.3V, practically this was not observed. The ADC could only reach a resolution of approximately 20mV. This can jeopardize the results and it is not taking full advantage of bypass capacitors and the filter.

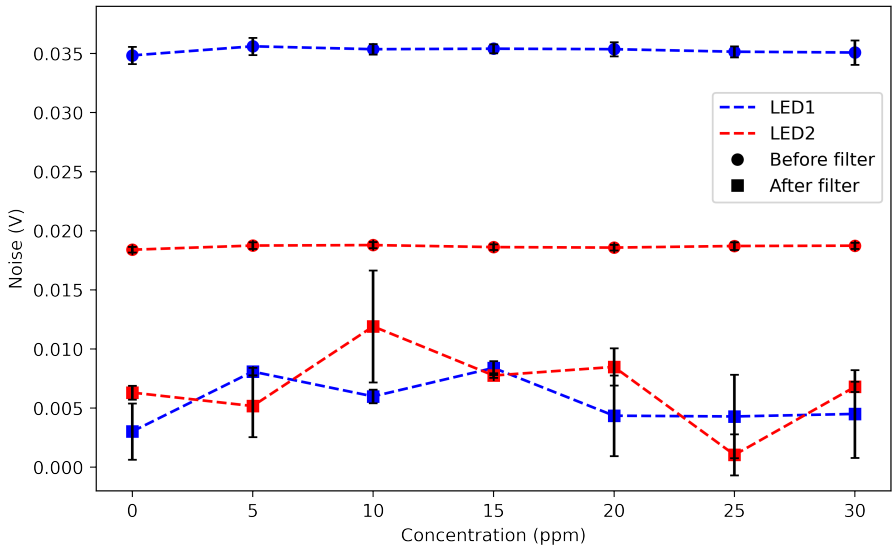

Figure 3.18: Noise observed for both LED/photodetector setups for different concentrations, before and after the bypass capacitors and filters being added

For the concentrations tested in Figure 3.18, it is possible to conclude that the noise stays constant as was expected, once electrical components only add the noise. Averaging these results, for LED1, the noise is reduced by a factor of 6.38; for the LED2, the noise is reduced by a factor of 2.75. After the filter is applied , it is also possible to see that the noise is not as stable as before. This must be neither a product of the filter nor the bypass capacitors but of the ADC of the microcontroller. As the noise starts to be lower than 20mV, the resolution starts to be comparable to the signal's noise. This means that for any measurement, if some value from the voltage signal crosses the voltage limits that define the bit n and the bit $n+1$, a noise term is added when analyzing it.

3.4.2 Calibration

Beyond the simple noise analysis, one of the most critical aspects of designing a sensor is the calibration process, which converts the detected voltage into a concentration value. There are two main approaches for this calibration: one is to use a calibration that directly converts the voltage to a specific concentration, and the other is to use a reference to calculate absorbance first and then apply a calibration to convert this value into a concentration. Although the circuit can control the voltage and maintain the applied voltage to ensure stable signal from the LEDs, the expected deterioration of the LED with time and

the sensor's temperature will change the light intensity in the output of the LED. A simple voltage calibration will end up depending on some uncontrollable factors. An approach using the voltage value of deionized water as reference should be a better option so that the absorbance can be calculated to make a calibration. Figure 3.19 represents the calculated absorbance and respective concentration for both LED's used. It was possible to find expressions that fit the behavior observed.

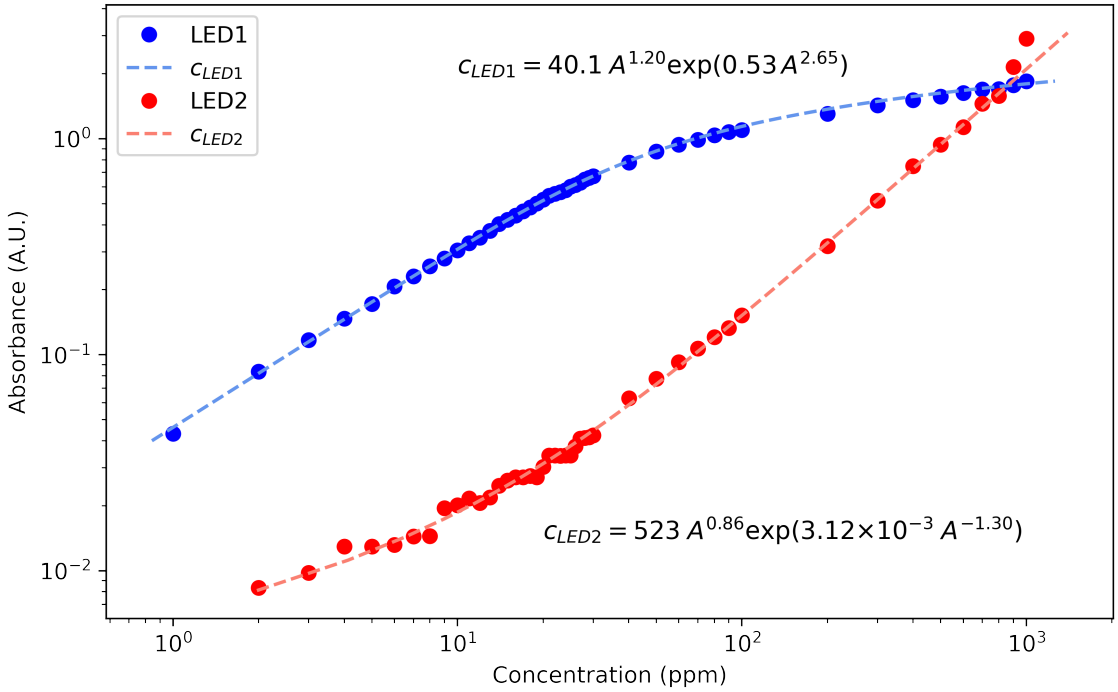

Figure 3.19: Concentration for every measure of absorbance for both LEDs and their respective calibration fit

In Figure 3.19, both axes are on a logarithmic scale because the range of concentrations analyzed was from 1 to 1000ppm and the absorbance calculated also ranged from values of approximately 10^{-2} to 1. For LED1 it is possible to observe for values of absorbance higher than 10^{0} a behavior similar to polynomial between both physical quantities in these scales; for values of absorbance smaller than 10^{0}, in these scales, the physical quantities have a linear behavior between them. This way, the calibration expression used is represented in equation 3.10 where c_{LED1} is the concentration in ppm and $A = \log(V_m/V_A)$ (V_m and V_A are the voltage measured by the sensor for any sample and for deionized water, respectively).

$$c_{LED1} = 4.01 \times 10^{1}\, A^{1.20} \exp\left(0.53\, A^{2.65}\right) \tag{3.10}$$

For LED2, for most of the absorbance values (10^0 >A> 2×10^{-2}), the behavior is linear between each logarithmic of the physical quantities, showing a turning point for A< 2×10^{-2} in which there is a fast increase in concentration with smaller values of absorbance, which was already expected by what was seen in sections 3.1 and 3.2. The calibration equation used for this LED is in equation 3.11.

$$c = 5.23 \times 10^2 A^{0.86} \exp\left(\frac{3.12 \times 10^{-3}}{A^{1.30}}\right) \tag{3.11}$$

Figure 3.20 represents the calibration's relative error for every concentration tested for both LEDs. For the LED with emission $\sim$ 230nm, the relative error of calibration stays smaller than 3% for every concentration smaller than 60ppm. As the concentration of the medium increases, the error in measurement starts to increase, reaching a relative error higher than 10%, which is too big. A similar thing happens for the other LED, but reversely: for concentrations higher than 60ppm, the calibration error stays smaller than 5%, but increases for values higher than 10% for small concentrations.

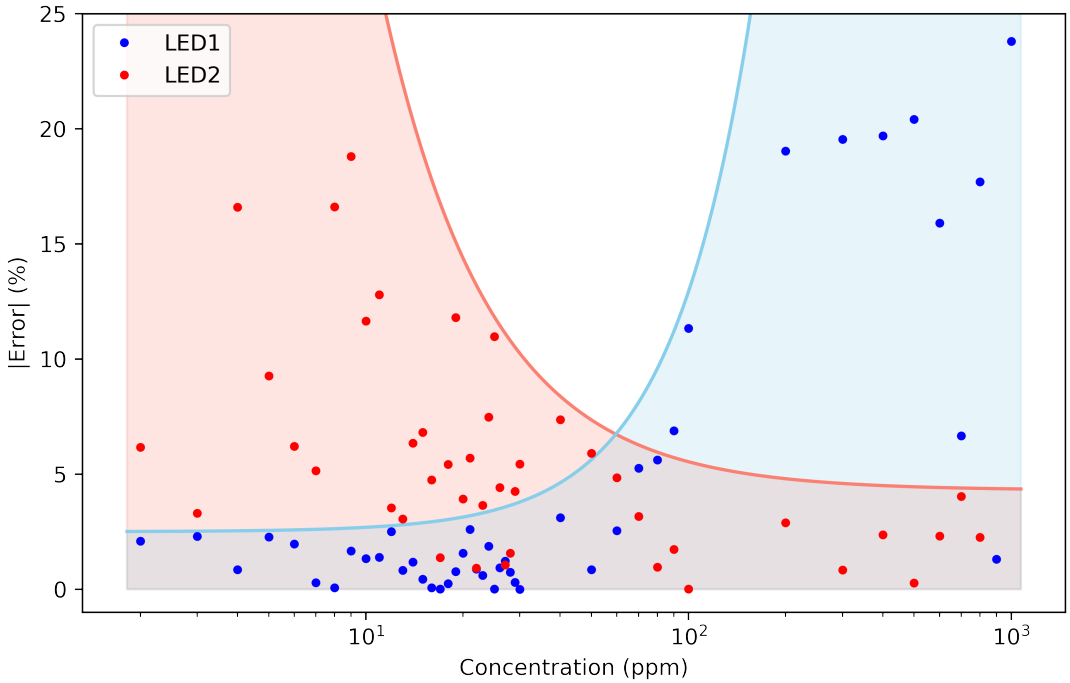

Figure 3.20: Relative error observed for both calibrations.

Figure 3.20 cements the idea that both LEDs can be used to increase the sensor's detection range. When the concentration reaches 65ppm, corresponding approximately to an absorbance of 1 and 0.1 for the LED1 and LED2, respectively, the LED used to determine the concentration can be switched. Therefore, LED1 is calibrated for a range between 1

to 65ppm and LED2 is calibrated for a range of 65 to 800ppm. It should be noted that this method is only valid if no chemical species that share these absorption wavelengths are diluted in the medium.

Table 3.2 shows the concentration in $NaNO_3$ samples prepared so that the nitrate diluted in deionized water is 5 to 30ppm, as the sensor is built to determine concentrations in this range. For each test, the different samples of $NaNO_3$ were prepared. Comparing with the results determined by the calibration in equation 3.10, it is possible to observe that for all the tests, the calibration values are close to the nitrate concentration of the samples prepared. Giving on average an overall error(%) of 2% Differences from what was expected must be the product of not just the error of the calibration and the sensor, but also the sample preparation.

Table 3.2: **Values determined by the sensor for each of the samples prepared for LED1**

N-NO_3 (ppm)	**Calibration values (ppm)**				
	Test 1	**Test 2**	**Test 3**	**Test 4**	**Test 5**
5	5.5	5.1	4.9	5.0	4.9
10	9.8	9.9	10.0	9.8	9.9
15	15.4	14.8	13.9	14.3	15.1
20	19.9	19.4	18.8	19.5	20.0
25	26.4	24.5	24.1	24.4	25.0
30	30.9	29.7	28.9	29.4	29.8

Table 3.3 is similar to Table 3.2, but uses the values detected for the LED/photodetector used for $\sim$ 300nm range. It shows that the calibration in equation 3.10 is less reliable than equation 3.11 for this range. As it is possible to see, there is much variation in the voltage values detected by the sensor, and consequently, the concentration determined. This wavelength, with this optical path, is not a reliable way to detect nitrate in these ranges, leaving LED1 as the only reference for detection.

Table 3.3: **Values determined by the sensor for each of the samples prepared for LED2**

$NaNO_3$ (ppm)	**Calibration values (ppm)**				
	Test 1	**Test 2**	**Test 3**	**Test 4**	**Test 5**
5	3.8	2.3	1.3	1.9	2.5
10	15.7	8.5	5.7	7.5	5.7
15	14.7	15.3	11.0	13.7	8.8
20	17.2	21.0	15.4	19.7	12.0
25	24.9	24.7	18.8	26.0	15.6
30	26.2	27.6	21.6	32.3	18.9

3.4.3 Thermal response

The built prototype has black paint, which, if exposed to sunlight, will absorb it and heat the prototype's structure. Most of the electronics in the PCB work with currents in the order of 10mA with small voltages ($\sim$ 1V), which is not enough for the PCB to heat up. Nevertheless, the LEDs work with higher voltages and currents, especially LED2, where the dissipated power is close to 1W (although this LED is equipped with a heat sink) and the part of the circuit responsible for controlling the peristaltic pump has an electric current of 400mA and a voltage drop across the LM317 of 8V so there is a lot of dissipated power, but this should not be enough as these components are isolated from each other, so the sensor temperature increase must come with the type of environment in which is placed. Because the sensor will be placed in tanks exposed to sunlight all day, it is expected that, even if protected, it will heat up, so this must be considered.

Figure 3.21 represents how the voltage from the photodetector for LED1 changes with the increase in temperature for different concentrations of N-NO_3^-, starting from a temperature of 27°C. For LED2, this was not explored since is not the one that will be used to determine the concentrations in this range.

For the tested concentrations, there is no change in behavior between them with the increase in temperature. This is good as it confirms that for these temperatures ($<$50°C), the physical behavior of the nitrate diluted must be constant. It is assumed that between the concentrations tested, this behavior still applies. It is also possible to observe a linear behavior with the increase in temperature, which means that for every ΔT temperature increase, the voltage increases with a factor of $\gamma \times \Delta T$. This factor,γ, can be obtained with the slope of the linear fit in figure 3.21 (equation 3.12).

$$\gamma = 1.51 \times 10^{-2}\ (^{\circ}C)^{-1} \tag{3.12}$$

It is possible to add the equation 3.10 to this error factor. Because the voltage measured by the ESP32, V_m, is going to deviate from the one assumed by the calibration, V_c, then $V_m = V_c\,(\gamma\Delta T + 1)$. If the sensor is calibrated using deionized water when is at a temperature T_0, the absorbance measured is going to be given by $A_m = -\log\left(V_c / V_{0,T_0}\right) - \log\left(\gamma\Delta T + 1\right)$. The latter term is the temperature error that needs to be added to equation 3.10. The updated calibration is given by equation 3.13, where $\Delta T = T - T_0$.

$$c = 4.01 \times 10^{1}\left(A_m + \log\left(\gamma\Delta T + 1\right)\right)^{1.20} \exp\left(0.53\left(A_m + \log\left(\gamma\Delta T + 1\right)\right)^{2.65}\right) \tag{3.13}$$

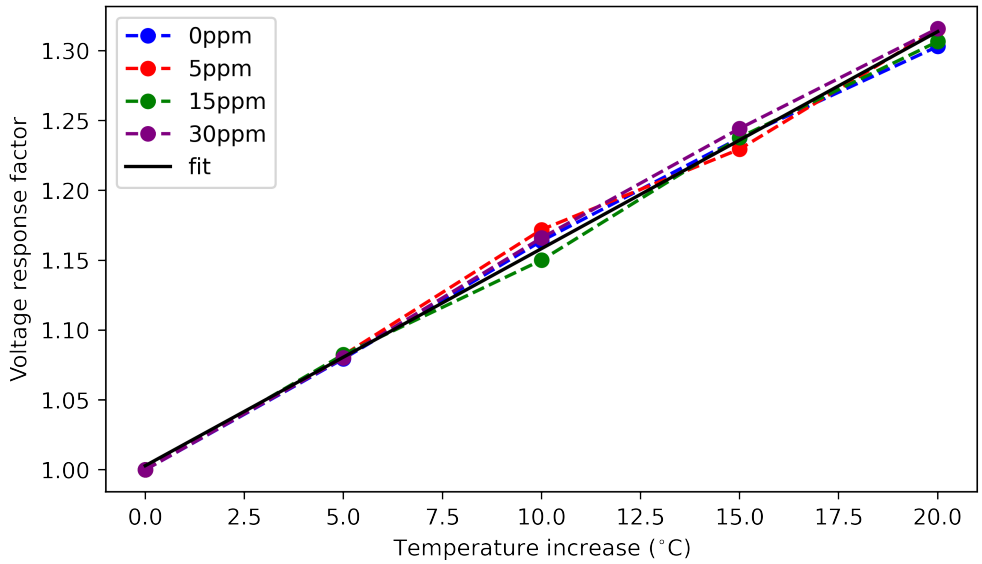

Figure 3.21: Voltage detected change with the increase in temperature.

The increase in temperature also increases the detected signal detected from the LED, because of its semiconductor nature leading to its increase in conductivity: more energy is given to excite electrons in the valence band to the conduction band, winning over the increase in electron scattering that would be expected in conductors. As the system heats up, because the voltage applied is constant, this increase in conductivity leads to an increase in current, which, for a LED, is intrinsically related to the number of photons emitted by itself. As more electrons are in the conduction band, more of it can decay to valence bands, emitting a higher number of photons that will be detected by the photodetector, increasing the voltage detected by the microcontroller. One big problem with the prototype built is in the fact that the TOCON_ABC1 photodetector is very sensitive, so, to avoid its oversaturation, the current that goes through the respective LED is in the orders of 1mA which makes it easily prone to noise coming from temperature variations, for example. To avoid these problems, one could have found a way to apply higher values of current in the LED, without overheating it, by changing the photodetector with a transimpedance amplifier or instead of applying a constant voltage to the signal, applying a constant electric current (Figure 3.22)

Figure 3.23 represents how, for different concentrations, the temperature increase would affect the sensor's value. The x-axis corresponds to the concentration that the calibration would determine if the temperature stayed constant. It is possible to see that as the temperature increases, the error grows, especially as the concentration gets smaller. As the temperature increases, the voltage detected increases, leading and leads the sensor to determine a value smaller in concentration than expected. For higher concentrations,

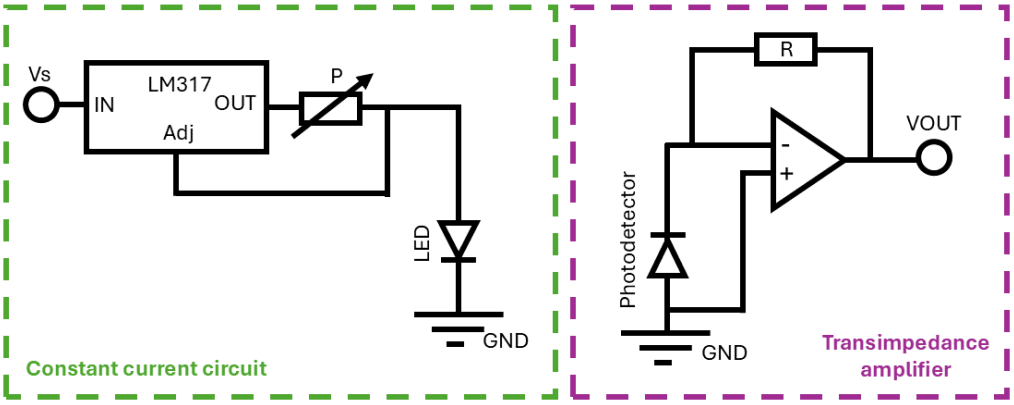

Figure 3.22: Constant current and transimpedance amplifier circuits that could have been implemented to lower the thermal noise

the error gets reduced and almost constant. For a temperature increase of just 2°C, it is possible to see that the error varies between 7% and 25%. These kind of variations are too high to be ignored, and it would be expected that even if the sensor is hidden from sunlight, the environment's temperature will affect the sensor's response.

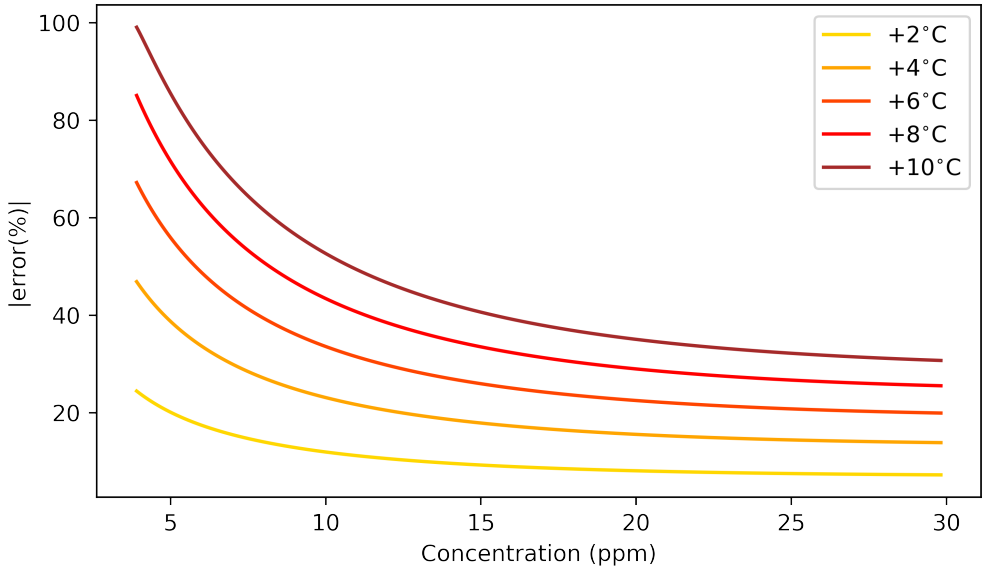

Figure 3.23: Error of the calibration used for different increase in temperature

3.4.4 Salinity response

Because the sensor has only been tested with deionized water and it has to be tested in a saltwater algae tank, it is also important to understand how the salinity will change the intensity of light that arrives at the photodetector and how the respective voltage will change. It is expected that the increase in salinity not only can end up increasing the absorbance of some wavelengths, but also change the refraction index of the water, bending some of the light rays. The results obtained for each LED photodetector setup are displayed in

figure 3.24, where voltage ratio is calculated as the ratio between the voltage obtained for each salinity and the voltage obtained when salinity(%) is 1%. It is interesting to see that

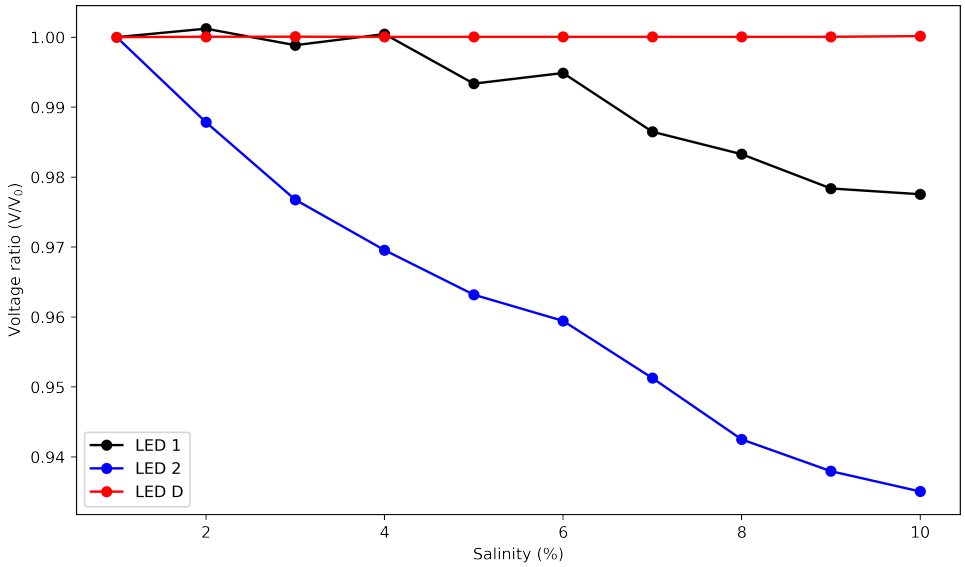

Figure 3.24: Voltage ratio between the voltage at salinity value x and voltage at salinity value of 1% for each LED setup.

for the LED that is used for detection of contaminants ($\lambda \sim 380$nm), there is no deviation detected for the voltage detected. This makes this LED rather useless for the detection of salinity in water. For LED 1 ($\lambda \sim 230$nm) and LED 2 ($\lambda \sim 300$nm), the voltage ratio decreases, meaning that the intensity of light that is arriving at the photodetector is smaller. For LED 1, for salinity(%) values smaller that 4%, there is barely any change in the voltage, as for bigger salinity values, the voltage only decreases for approximately 98% of its original value. LED2 depends more with salinity, as its voltage decreases to 94% of what was obtained for a salinity of 10%. For LED2, this could mean that the results would be jeopardized, but It is expected that for a controlled aquaculture environment, the salinity won't change much. This parameter is intrinsically related with the kind of culture that we want to cultivate. This way, it is not expected that the salinity in such an environment will have big variations, so, if the sensor is calibrated with water from the salinity of the environment, we can assume that the absorbance behavior observed for nitrate will be the same for each LED/photodetector setup.

3.5. Sensor Testing

3.5.1 Algae aquarium measurements

The first time the sensor was placed, the circuit was still not updated and was placed in position 1, as mentioned in section 2.5.1. The results were registered for 5 days, every

thirty minutes, beginning at 1:36pm. The concentrations determined by both LEDs is shown in figure 3.25. By just analyzing the y axis of both LEDs, the concentrations given by LED2 is way bigger than the other. Because it is expected that the concentration of nitrate ions in water with algae is in the orders of 10ppm and because the values the sensor gives must be the same or higher than the real values, the lower concentration must be the one closer to the real one. This is the concentration given by LED1 which is in the orders of $\sim$20ppm. This is close enough to what was expected for the algae tank.

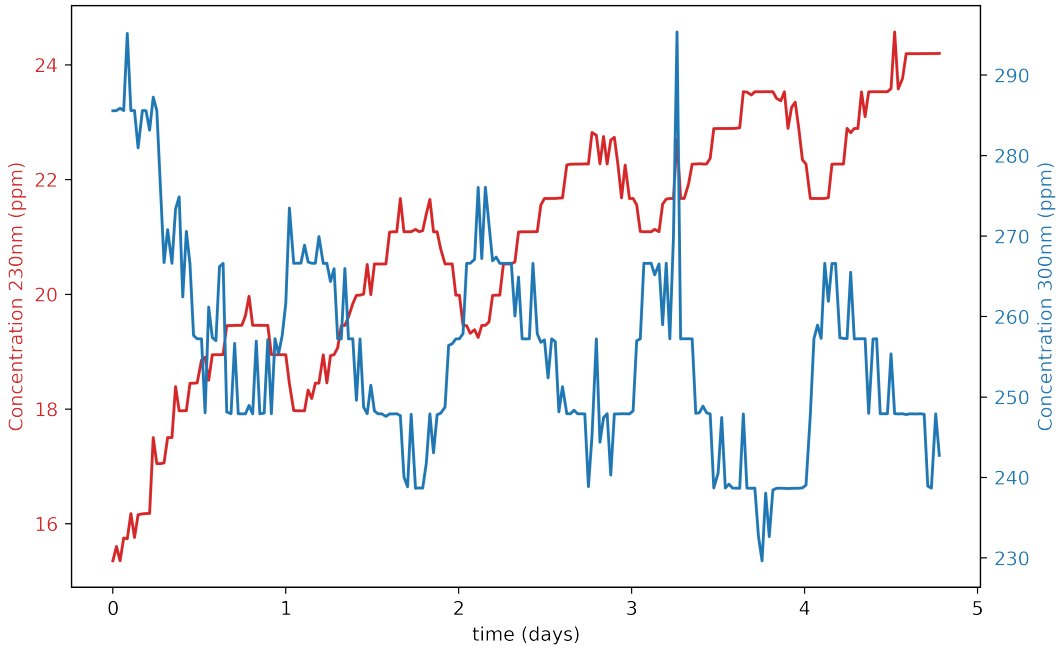

Figure 3.25: Values of concentration given by values coming from both LED1 (red) and LED2(blue)

By colorimetric methods, using the DR1900 Portable Spectrophotometer (Hach) and the protocol LCK138, which measures total concentration of N dissolved, it was possible to estimate a concentration of 15.3ppm in the aquarium, in which only 0.39ppm comes from the dissolved nitrates, using protocol LCK339, which only measures nitrate ions concentration. The value given by protocol LCK138 is close enough to the values given by the LED1, although we calibrated using $NaNO_3$ solutions.

To verify why both LEDs give such a different value in concentration, it is possible to observe and analyze the aquarium water spectrum represented in Figure 3.26. In this spectrum, the results show the same peak in absorbance near the wavelength of $\lambda \approx$ 230nm, which is similar to figures 3.1 and 3.3. This peak is most prominent when the nitrogen is dissolved in water. The most significant difference from these other spectra is for $\lambda >$240nm where it is possible to see an increase in absorbance with the decrease

in wavelength. Some of this absorbance must be the product of particles in suspension in the aquatic medium, as using filters of different sizes shows a decrease in absorbance in the whole spectra. For the filter with size 7-10μm, for higher wavelengths, the filter influence is visible and proves in fact that the turbidity is a factor to take into account. For the filter with a size of 0.2μm there is a substantial decrease in absorbance in the whole spectrum, which makes sense. As the filter pores are smaller, the water is more pure, and fewer suspended particles are responsible for light scattering and absorption.

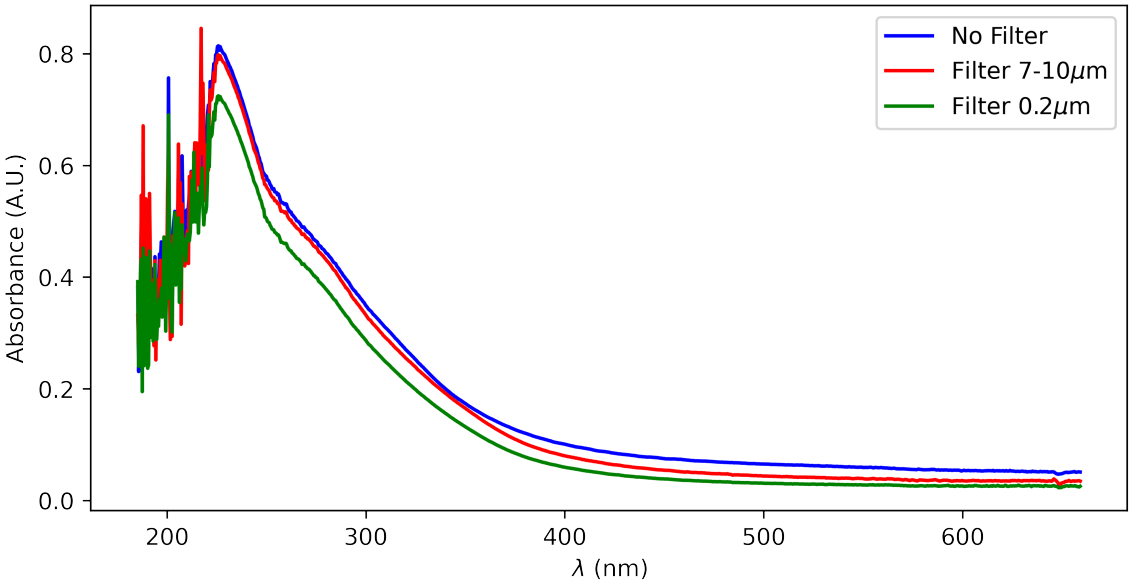

Figure 3.26: Spectrum of the aquarium water for different filters

In Figure 3.25, it is possible to see an oscillatory behavior in both LEDs. By doing a Fourier analysis, it is possible to see a frequency peak corresponding to a cycle for 23-25 hours. This is a day cycle and must indicate a temperature dependence from the sensor. It is known that the increase in temperature leads to a decrease in the concentration measured in LED1. Because the measurements were done starting at 1:36pm, it is possible to observe that this decrease happens around the same time each day when the aquarium is exposed to sunlight, causing the sensor to heat up. For the five days, despite some oscillation, the concentration from the LED1 showed an overall increase in behavior. This was not expected, because the algae consume the dissolved nitrate, so the observed behavior must be a decrease or constant concentration over time. The observed behavior could be due to the possible deterioration of the LED, accumulation of dirt on the flowcell walls or air bubbles, that could be a product of a cut in the tube, as it was possible to see an increasing number of bubbles throughout the days. To isolate this behavior from the dissolved nitrate, the flowcell was cleaned, the sensor was placed away from any sunlight interference and the signal behavior was analyzed with deionized water (figure 3.27).

In Figure 3.27, it is possible to see that LED2 stays relatively constant, although a decrease follows a slight increase. Compared with the LED1, the voltage detected in deionized water decreases for the first day and for the second day also stays relatively constant. This might indicate that the increase in concentration observed in Figure 3.25 might come from the dirtiness of the aquarium water. As time passed, it was also possible to observe new bubbles in the tubes. It was observed that the bubbles of air stuck in the flowcell might also explain this behavior because it is placed vertically with the LED/photodetector with LED1 above the other LED/photodetector. As the bubbles of air reached the flowcell, due to the water being pumped by the peristaltic pump, most bubbles would get stuck in it and pile up in a bigger bubble that would grow up from top to bottom of the flowcell, explaining why the decrease in voltage signal was possible to observe in one LED and not in the other. This bubble would not be filled even after the peristaltic pump was activated. This must be because of the adhesion forces of water in the tube. Once the peristaltic pump stopped, the bubble would stay in the flowcell without being filled, which shows that this problem must be treated from the beginning and cannot be fixed during measurements. The bubbles of air observed were product of a cut in the tubes that was identified. This was fixed by substituting the damaged tubes.

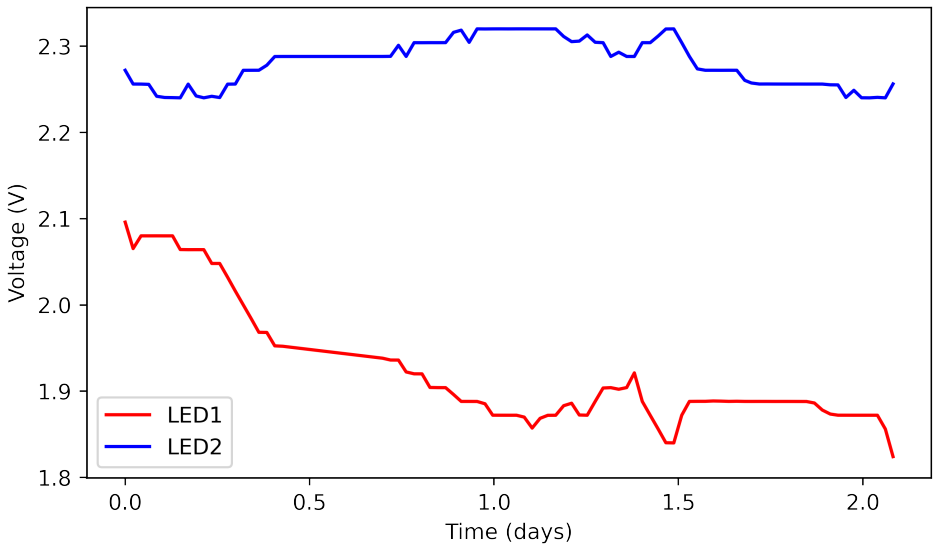

Figure 3.27: Voltage values detected from both LEDs in deionized water

3.5.2 Circuit update

As was expected and verified, temperature plays an important role in the voltage the ESP32 will detect. To improve the noise of voltage signal detected by the ADC of the microcontroller and to supply the ESP32 without the use of USB-C cable (as this sensor

is expected to be implemented in algae tanks, the data has to be transferred via wireless, leaving the option to supply the ESP32 with the USB-C cable), the circuit used had to be changed and updated with the addition of the thermistor MF52A 103, the ADC ADS1015 and a voltage regulator circuit with output of 5V. The addition of the ADC DS1015 also verifies if the step behavior observed for both LEDs in Figure3.25 comes from the already faulty ADC of the microcontroller, which is another problem to identify.

Adding a voltage regulator with 5V output allows the prototype to use wireless communication to send data. For example, this could be by Bluetooth, Wi-Fi or zigbee. The device's input and output were connected to the supply voltage and the 5V pin of the ESP32. This 5V can also be used to supply the temperature sensor circuit: a 10kΩ resistor is in series with the thermistor. The voltage across the terminals of the thermistor is detected, giving a specific temperature that can be determined by the calibration in the respective datasheet [88]. The supply of the ADC used was done by the 5V output of the voltage regulator. Because the device works with an I^2C communication protocol, the GPIO18 and GPIO9 were connected to the SDA and SCL pins. The address pin was connected to the GND so the address byte could be defined as 0x48 [89]. The "Ax" pins of the ADC were connected so that the voltage across the thermistor could be measured, as well as the voltage from the photodetectors after going through the signal filter. The entire circuit is displayed in Appendix C, Figure C.2.

3.5.3 Algae aquarium measurements with updated circuit

After updating the sensor's circuit to detect temperature using the thermistor and a new ADC, the sensor was placed in position 2 (figure 2.9) and the voltage from the LEDs was detected. The calibration before and after considering the temperature is represented in figure 3.28 along with the temperature detected by the thermistor with time, beginning at time 1:21pm . Comparing with the results in 3.25, it is easy to see how the ADC improves the results and avoids the step behavior observed previously.

The temperature profile shows an inverted behavior to the concentration, especially for the calibration results before the temperature is considered: as the temperature increases, the concentration decreases. Although the position of the sensor was changed so that less sunlight would reach it, there is a temperature peak for approximately a day, with the respective concentration reaching the lowest. This corroborates the hypothesis that the sensor's temperature is critical to take in account. Comparing the results before and

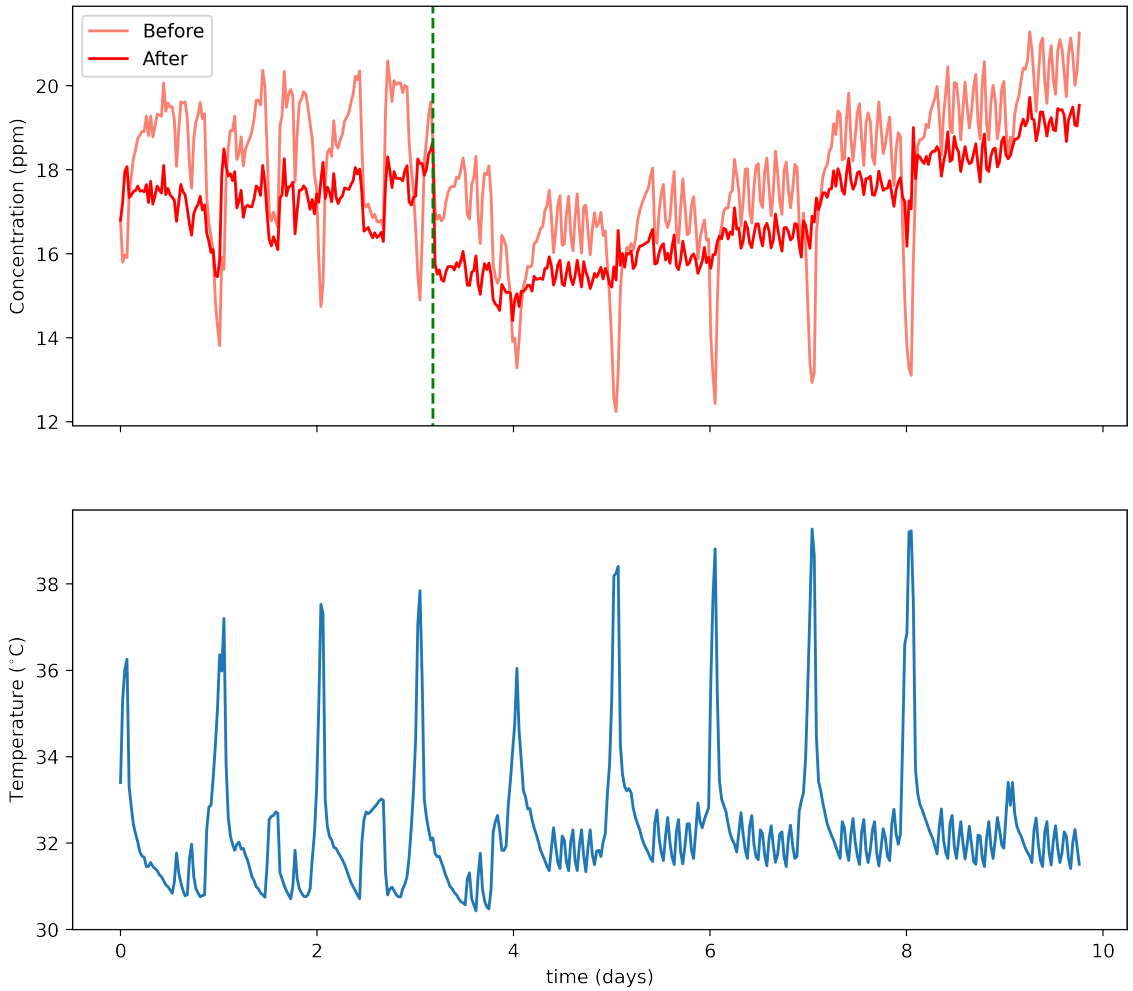

Figure 3.28: Concentrations determined by the calibration for LED1 before and after taking the temperature in consideration (red, above); temperature of the sensor with time (blue, below)

after taking into account the temperature in the calibration, the amplitude of the concentration throughout the days goes from 9.1 to 5.3ppm, respectively. The oscillatory behavior observed between temperature peaks in the concentration values has a period of approximately 2-3 hours and should also be a product of temperature oscillations in the laboratory as these are also found in the temperature profile, although, after taking the temperature in account for the calibration, the oscillation is still visible

In Figure 3.28, it is possible to separate the concentration profile into two different parts: for the first 3 days, the concentration values had an almost Gaussian distribution with an average of 17.3ppm and a standard deviation of 0.6 ppm. Comparing with the colorimetric approach done at the beginning of this measurement, where a concentration of about 14.3ppm of dissolved nitrogen in water was determined, it was possible to understand that the updates in the circuit were essential to sensor's accuracy.

After 3.2 days (green dashed line in figure 3.28), a substantial amount of saltwater, almost 20% of volume increase, was inserted in the aquarium which caused the concentration to decrease as just expected. Right after the sudden decrease in concentration, it is possible to see an increase for the rest of the days, where every time, after the peak of temperature, the concentration increased suddenly from 0.5 to 1ppm and stayed relatively constant until another peak appeared. The concentration should be expected to stay constant (as no nutrients were placed in those days) once it decreases, but this is not seen. One might conjecture that this could come from the fact that every time the LED gets heated, its internal components give a slightly different value. Another hypothesis might be that the concentration of nitrate can increase due to the evaporation of water. As the sunlight reaches the aquarium and heats it up, some water can be evaporated, leading to the increase in concentration. This cannot be verified as no colorimetric measurement was done to see if with time, this increase was possible to see.

Although LED2 cannot be used to give accurate concentration values, it is possible to trace its voltage profile during those days and see if the same behavior was observed between each temperature peak. Just like what was observed in Figure 3.28, Figure 3.29 represents the voltage profile throughout the days and the respective average value every day, without the temperature peaks, and it is possible to see that the voltage/concentration has a decreasing/increasing tendency, although not so notorious, which gives weight to the hypothesis that what is being seen might be the dissolved nitrate in the aquarium increasing or any damage to the PCB everytime it heats up.

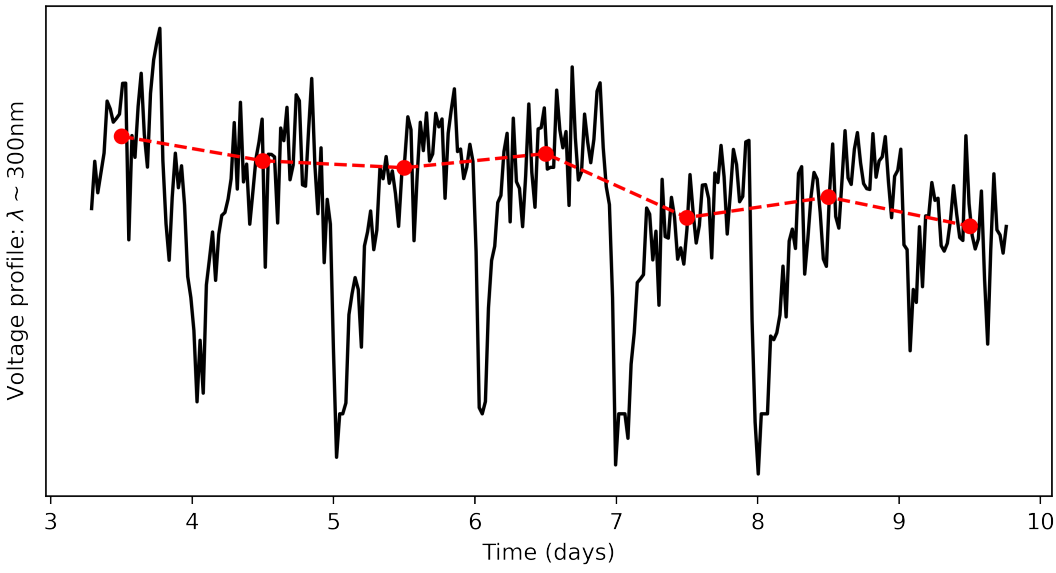

Figure 3.29: Voltage profile for the LED with peak emission near 300nm (black) and the average value of each day (red)

To verify if the behavior is from aquarium water, the sensor response from LED1 was analyzed with a reservoir of deionized water for 4 days, with the same procedure of every 30 minutes water gets pumped from this reservoir and the concentration values determined with the calibration, (Figure 3.30). Just like what was observed and discussed earlier, the voltage detected decreased each time the temperature peaked, although this should not be observed because it should have been constant throughout all those days. This shows that the temperature variations may not just influence the voltage instantly, which is not ideal when building a sensor that will be used in algae tanks that are exposed to sunlight daily.

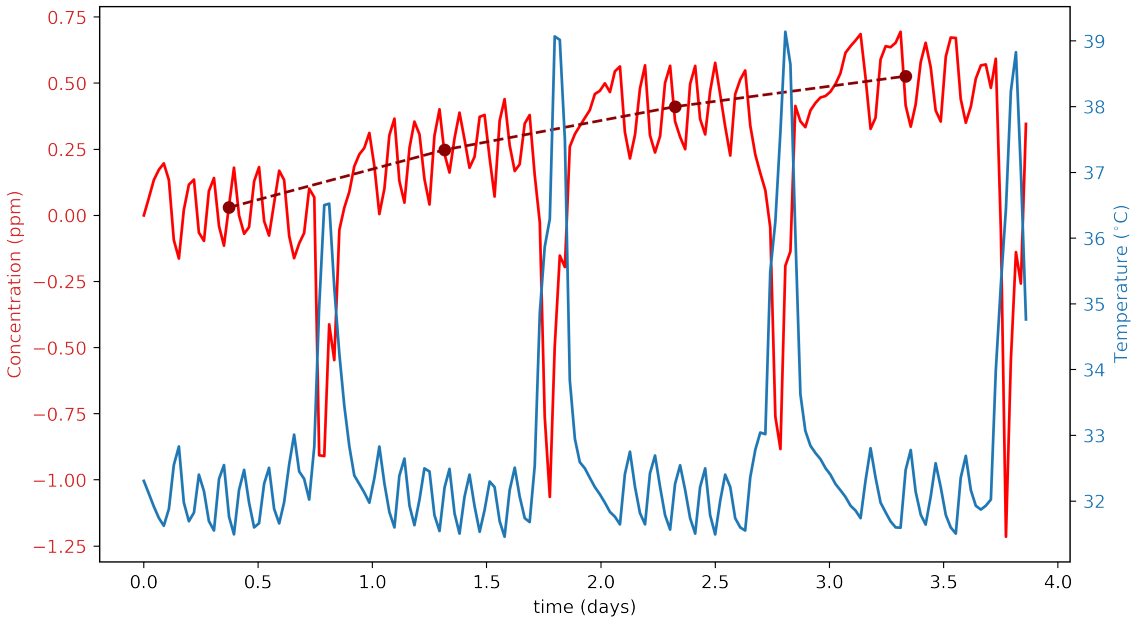

Figure 3.30: Concentrations determined by the calibration in deionized water (red) and average value of each day (dark red); temperature throughout the days (blue)

In figure 3.31 is presented the concentrations determined by LED1 for a period of 1 month, already thermally corrected, and the respective temperature for each instant of measurement. No longer is seen systematically the step-increase that was verified in figure 3.28. The values determined had periods where they stayed relatively constant, but overall the behavior can be separated in three parts. For approximately 15 days is seen an increase in concentration, from 14 to 22ppm, and then it decreases rather fast for 10 days after (with a slight increase in day 20) for about 15ppm, and then, in the last days, it increases between 16 to 18ppm where it stays rather constant between these results. The peak observed in day 28 is most probably an outlier and could be that some small algae passed the filter and entered the flowcell, as it only corresponds to a single point, although we can not be certain as no observations to the prototype were done to verify this hypothesis.

Unfortunately, no colorimetric measurements were done for the algae tank water during this period and so it is impossible to verify if this variation is truly comes from the variation of the concentration of nitrates in the tank. Because algae only consume these ions, this increase in concentration could be due to the addition of the nutrients that would have been added to the algae to feed them, although these were not also registered when they were done.

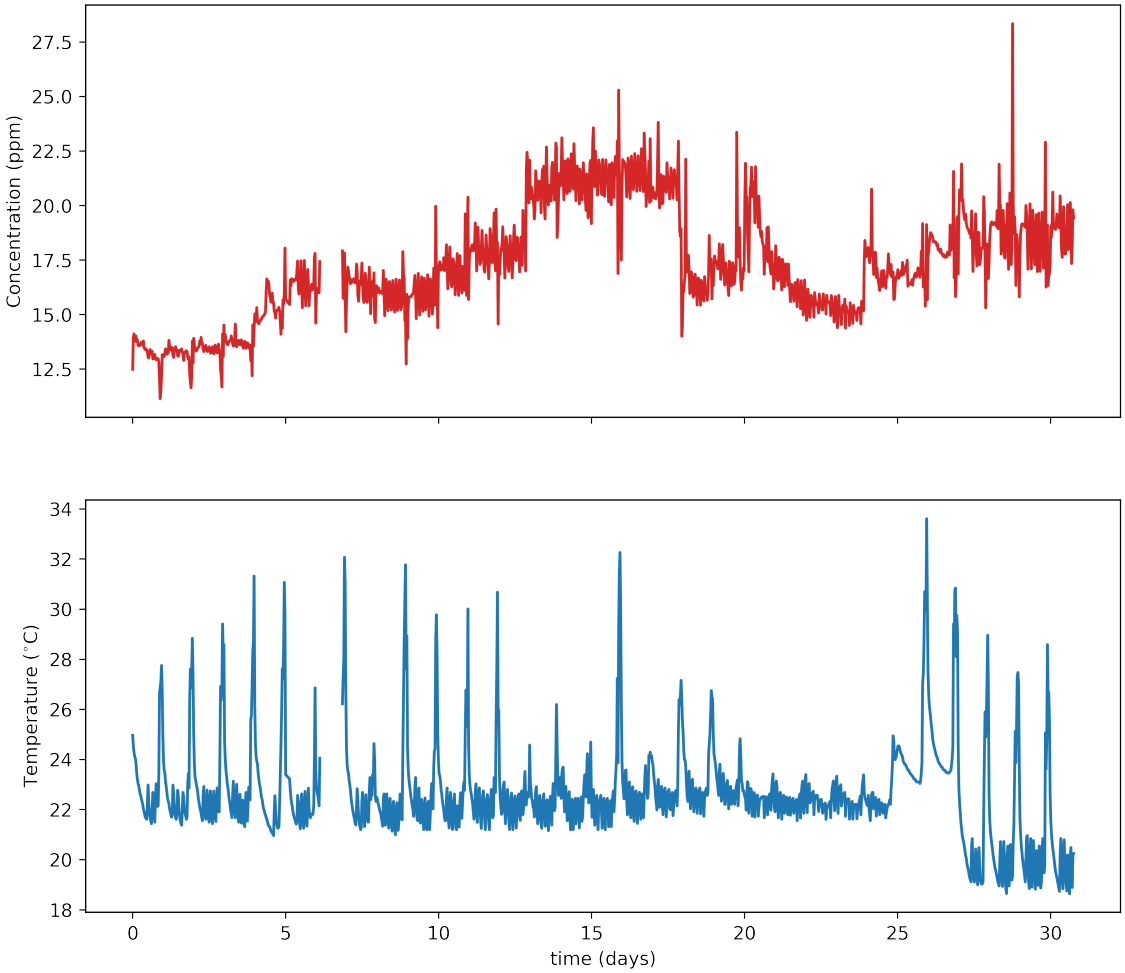

Figure 3.31: Concentrations determined by the LED1 setup after the temperature correction (red, above); temperature of the sensor with time (blue, below)

At least we know that between day 25 and day 26 that the laboratory's air conditioner was turned off and so the oscillation of 2 hours, that started to be apparent up to day 4 in figure 3.28 for both temperature and concentrations measurements, disappeared for both measurements in figure 3.31. This meant that this oscillation was not due to any kind of electronics interference, but actually from the thermal regulation of the laboratory.

4. Conclusions

The main objective of developing a cost-effective and reliable optical sensor to be tested and used in an algae tank has been successfully achieved. The absorbance wavelengths of dissolved NO_2^- and NO_3^- were effectively used to determine concentrations across different ranges. By exploring the relationship between increased nitrate concentration in the aquatic medium, optical path, and absorption at wavelengths near 230nm and 300nm, it was determined that an optical path of 10mm is optimal for the former and 20mm for the latter. The use of two different optical paths would have been ideal, but would jeopardize the simplicity of the sensor design and cost. By using only LEDs and photodetectors with spectral emission and optical response near these wavelengths, a prototype sensor was developed with a detection range from 1 to 10^3ppm, which is higher than many comparable sensors, without losing accuracy across the range. Firstly, this prototype was tested in a controlled environment where the concentration of dissolved nitrate ranged from 5 to 30ppm. This way, it was possible to see that LED1 ($\lambda \sim$230nm) setup has potential for sensing systems, showing an average error of 2% for all the samples prepared. This LED1 setup also showed almost no variation with salinity tests, which reinforces its potential use not only for freshwater, but also saltwater measurements

During the the algae aquarium measurements, it was observed that the temperature and turbidity of the water significantly impact the sensor response due to its internal circuitry. By estimating that the voltage signal would increase by a factor of 1.02 for every increase of 2°C, the inclusion of a thermistor was able to correct some of the fluctuations observed, although improvements can be done in the thermal response calibrations like better measurement methods: increasing the temperature in smaller intervals would lead to a better calibration curve, although this would take a longer period of time; increasing the temperature range tested is also ideal as for most of the year temperatures are smaller than 30°C. Testing The addition of filters to decrease the turbidity seems to be imperative to obtain accurate values as these were probably the reasons for the different values determined between the prototype, 17.3ppm, and the colorimetric methods, 14.3ppm. Alternatively, to maintain the sensor low cost and as sustainable as possible, calibration and communication with a turbidimeter, already being developed for the algae tanks, could be a solution. Before the sensor determines the concentration value using its calibration, the turbidimeter can measure turbidity and feed this data into the sensor's calibration process, similar

to the resistance value from the thermistor. This would require a calibration to be made for the sensor for a range of values of turbidity that would be expected in these algae tanks.

In conclusion, the sensor has great potential to be implemented not only for algaculture but also in other applications where dissolved nitrate needs to be detected and monitored. The detection range can be chosen by adjusting the the optical path and so this kind of design can be implemented with low cost and in a more sustainable way compared to other methods, such as colorimetric techniques that require reagents. As UV-A LED research improves, the development of sensors like the one developed throughout this thesis will become even more affordable. Although there are factors that can dramatically change the accuracy values, it's possible to adapt to them, specially in this project where a turbidimeter is also in development. Beyond these advantages, sensor's simple design facilitates its maintenance, as only the LEDs require periodic replacement.

This thesis was focused in developing a first prototype, but a lot work still needs to be done for this sensor to be used for algae tanks. Improvements in the electronics can still be made, such as increasing the ADC detection range and raising the photodetector voltage supply from 3.3 to 5V. Because LED1 saturates the respective photodetector with small currents of below 1mA when aligned, a lot of noise is added and makes the setup more sensitive to deterioration that is expected with time. This change would increase the accuracy and precision of the results by letting higher currents be applied to the LED, "drowning" the noise current. Therefore, a lower fraction of intensity detected by the photodetector would be from noise current. Additionally, instead of supplying the LEDs with constant voltage, these should be controlled with constant electric current. Because the photodetector would be easily saturated, the circuit used required a precise control of a digital potentiometer to turn the LED on and off. With the hypothetical constant current circuit, this precise control would require also a digital potentiometer that would share the same electric current going through the LED and this would potentially damage it, if the window of detection was higher, this precise control would not be necessary and the digital potentiometer could be replaced by a resistor and be turned on and off by a MOSFET just like the peristaltic pump. The software that is going to be developed to control the sensor is also important to complete the project. For this software, a user-friendly interface will have to be developed so that the sensor parameters can be easily changed and the concentration easily monitored by having a real-time graph updating each time the sensor makes a measurement. Likewise, the wireless communication between the sensor and the software also needs development. The design for the sensor also needs

to be developed so that the PCB can be hidden and the sensor structure more sturdy.

References

[1] R. Lal, “Restoring soil quality to mitigate soil degradation,” *Sustainability*, vol. 7, no. 5, pp. 5875–5895, 2015. [Cited on page 1.]

[2] T. Newbold, L. N. Hudson, S. L. Hill, S. Contu, I. Lysenko, R. A. Senior, L. Börger, D. J. Bennett, A. Choimes, B. Collen *et al.*, “Global effects of land use on local terrestrial biodiversity,” *Nature*, vol. 520, no. 7545, pp. 45–50, 2015. [Cited on page 1.]

[3] R. L. Naylor, R. J. Goldburg, J. H. Primavera, N. Kautsky, M. C. Beveridge, J. Clay, C. Folke, J. Lubchenco, H. Mooney, and M. Troell, “Effect of aquaculture on world fish supplies,” *Nature*, vol. 405, no. 6790, pp. 1017–1024, 2000. [Cited on page 1.]

[4] P. Smith, M. Bustamante, H. Ahammad, H. Clark, H. Dong, E. A. Elsiddig, H. Haberl, R. Harper, J. House, M. Jafari *et al.*, “Agriculture, forestry and other land use (afolu),” in *Climate change 2014: mitigation of climate change. Contribution of Working Group III to the Fifth Assessment Report of the Intergovernmental Panel on Climate Change*. Cambridge University Press, 2014, pp. 811–922. [Cited on page 1.]

[5] L. Pereira, *Edible seaweeds of the world*. CRC Press, 2016. [Cited on pages 1 and 2.]

[6] J. S. Lucas, P. C. Southgate, and C. S. Tucker, *Aquaculture: Farming aquatic animals and plants*. John Wiley & Sons, 2019. [Cited on pages 1 and 2.]

[7] T. V. R. Pillay *et al.*, *Aquaculture: principles and practices.* Fishing news books, 1990. [Cited on page 1.]

[8] W. Mook, M. Chakrabarti, M. Aroua, G. Khan, B. Ali, M. Islam, and M. A. Hassan, “Removal of total ammonia nitrogen (tan), nitrate and total organic carbon (toc) from aquaculture wastewater using electrochemical technology: a review,” *Desalination*, vol. 285, pp. 1–13, 2012. [Cited on pages 1 and 3.]

[9] J. Bostock, B. McAndrew, R. Richards, K. Jauncey, T. Telfer, K. Lorenzen, D. Little, L. Ross, N. Handisyde, I. Gatward *et al.*, “Aquaculture: global status and trends,” *Philosophical Transactions of the Royal Society B: Biological Sciences*, vol. 365, no. 1554, pp. 2897–2912, 2010. [Cited on page 1.]

[10] R. J. Shields and I. Lupatsch, “Algae for aquaculture and animal feeds,” *J Anim Sci*, vol. 21, no. 1, pp. 23–37, 2012. [Cited on pages 1 and 2.]

[11] L. Valente, A. Gouveia, P. Rema, J. Matos, E. Gomes, and I. Pinto, “Evaluation of three seaweeds gracilaria bursa-pastoris, ulva rigida and gracilaria cornea as dietary ingredients in european sea bass (dicentrarchus labrax) juveniles,” *Aquaculture*, vol. 252, no. 1, pp. 85–91, 2006. [Cited on page 2.]

[12] J. Cai, A. Lovatelli, J. Aguilar-Manjarrez, L. Cornish, L. Dabbadie, A. Desrochers, S. Diffey, E. Garrido Gamarro, J. Geehan, A. Hurtado *et al.*, “Seaweeds and microalgae: an overview for unlocking their potential in global aquaculture development,” *FAO Fisheries and Aquaculture Circular*, no. 1229, 2021. [Cited on page 2.]

[13] M. Ottinger, K. Clauss, and C. Kuenzer, “Aquaculture: Relevance, distribution, impacts and spatial assessments–a review,” *Ocean & Coastal Management*, vol. 119, pp. 244–266, 2016. [Cited on page 2.]

[14] S. Action, “World fisheries and aquaculture,” *Food and Agriculture Organization*, vol. 2020, pp. 1–244, 2020. [Cited on page 2.]

[15] M. Verdegem and R. Bosma, “Water withdrawal for brackish and inland aquaculture, and options to produce more fish in ponds with present water use,” *Water Policy*, vol. 11, no. S1, pp. 52–68, 2009. [Cited on pages 2 and 3.]

[16] B. G. Paul and C. R. Vogl, “Impacts of shrimp farming in bangladesh: Challenges and alternatives,” *Ocean & Coastal Management*, vol. 54, no. 3, pp. 201–211, 2011. [Cited on page 2.]

[17] J. A. Hargreaves, “Nitrogen biogeochemistry of aquaculture ponds,” *Aquaculture*, vol. 166, no. 3-4, pp. 181–212, 1998. [Cited on page 2.]

[18] M. Troell, N. Kautsky, M. Beveridge, P. Henriksson, J. Primavera, P. Rönnbäck, and C. Folke, “Aquaculture,” in *Encyclopedia of Biodiversity (Second Edition)*, second edition ed., S. A. Levin, Ed. Waltham: Academic Press, 2013, pp. 189–201. [Cited on page 3.]

[19] C. Kuenzer, P. Leinenkugel, M. Vollmuth, and S. Dech, “Comparing global land-cover products–implications for geoscience applications: an investigation for the trans-boundary mekong basin,” in *Remote Sensing the Mekong*. Routledge, 2018, pp. 6–33. [Cited on page 3.]

[20] H.-H. Nguyen, “The relation of coastal mangrove changes and adjacent land-use: A review in southeast asia and kien giang, vietnam,” *Ocean & coastal management*, vol. 90, pp. 1–10, 2014. [Cited on page 3.]

[21] F. Páez-Osuna, A. Gracia, F. Flores-Verdugo, L. P. Lyle-Fritch, R. Alonso-Rodrıguez, A. Roque, and A. C. Ruiz-Fernández, “Shrimp aquaculture development and the environment in the gulf of california ecoregion,” *Marine Pollution Bulletin*, vol. 46, no. 7, pp. 806–815, 2003. [Cited on page 3.]

[22] R. H. Bosma, C. T. Hanh, J. Potting, P. Anh, V. Dung, M. Fransen, H. Hien, P. Hong, N. Minh, T. Tuan *et al.*, “Environmental impact assessment of the pangasius sector in the mekong delta,” Wageningen University, Tech. Rep., 2009. [Cited on page 3.]

[23] F. C. Cabello, “Heavy use of prophylactic antibiotics in aquaculture: a growing problem for human and animal health and for the environment,” *Environmental microbiology*, vol. 8, no. 7, pp. 1137–1144, 2006. [Cited on page 3.]

[24] A. Ciji and M. S. Akhtar, “Nitrite implications and its management strategies in aquaculture: a review,” *Reviews in Aquaculture*, vol. 12, no. 2, pp. 878–908, 2020. [Cited on page 3.]

[25] J. A. Camargo, A. Alonso, and A. Salamanca, “Nitrate toxicity to aquatic animals: a review with new data for freshwater invertebrates,” *Chemosphere*, vol. 58, no. 9, pp. 1255–1267, 2005. [Cited on page 3.]

[26] M. H. Ward, T. M. DeKok, P. Levallois, J. Brender, G. Gulis, B. T. Nolan, and J. VanDerslice, “Workgroup report: drinking-water nitrate and health—recent findings and research needs,” *Environmental health perspectives*, vol. 113, no. 11, pp. 1607–1614, 2005. [Cited on pages 3 and 6.]

[27] M. M. Dorgham, “Effects of eutrophication,” *Eutrophication: Causes, Consequences and Control: Volume 2*, pp. 29–44, 2014. [Cited on page 3.]

[28] P. Han, Q. Lu, L. Fan, and W. Zhou, “A review on the use of microalgae for sustainable aquaculture,” *Applied Sciences*, vol. 9, no. 11, p. 2377, 2019. [Cited on pages 3 and 4.]

[29] E. Sanz-Luque, A. Chamizo-Ampudia, A. Llamas, A. Galvan, and E. Fernandez, “Understanding nitrate assimilation and its regulation in microalgae,” *Frontiers in plant science*, vol. 6, p. 163887, 2015. [Cited on page 3.]

[30] H. Li, S. Chen, K. Liao, Q. Lu, and W. Zhou, “Microalgae biotechnology as a promising pathway to ecofriendly aquaculture: a state-of-the-art review,” *Journal of Chemical Technology & Biotechnology*, vol. 96, no. 4, pp. 837–852, 2021. [Cited on page 4.]

[31] L. C. Meher, D. V. Sagar, and S. Naik, “Technical aspects of biodiesel production by transesterification—a review,” *Renewable and sustainable energy reviews*, vol. 10, no. 3, pp. 248–268, 2006. [Cited on page 4.]

[32] Q. Hu, M. Sommerfeld, E. Jarvis, M. Ghirardi, M. Posewitz, M. Seibert, and A. Darzins, “Microalgal triacylglycerols as feedstocks for biofuel production: perspectives and advances,” *The plant journal*, vol. 54, no. 4, pp. 621–639, 2008. [Cited on page 4.]

[33] L. Rodolfi, G. Chini Zittelli, N. Bassi, G. Padovani, N. Biondi, G. Bonini, and M. R. Tredici, “Microalgae for oil: Strain selection, induction of lipid synthesis and outdoor mass cultivation in a low-cost photobioreactor,” *Biotechnology and bioengineering*, vol. 102, no. 1, pp. 100–112, 2009. [Cited on page 4.]

[34] S. A. Scott, M. P. Davey, J. S. Dennis, I. Horst, C. J. Howe, D. J. Lea-Smith, and A. G. Smith, “Biodiesel from algae: challenges and prospects,” *Current opinion in biotechnology*, vol. 21, no. 3, pp. 277–286, 2010. [Cited on page 4.]

[35] L. Peng, D. Fu, H. Chu, Z. Wang, and H. Qi, “Biofuel production from microalgae: a review,” *Environmental Chemistry Letters*, vol. 18, pp. 285–297, 2020. [Cited on page 4.]

[36] Sep 2024. [Online]. Available: https://innoaquaproject.eu/ [Cited on page 5.]

[37] J. M. Ebeling and M. B. Timmons, “Recirculating aquaculture systems,” *Aquaculture production systems*, pp. 245–277, 2012. [Cited on page 5.]

[38] J. Van Rijn, “Waste treatment in recirculating aquaculture systems,” *Aquacultural Engineering*, vol. 53, pp. 49–56, 2013. [Cited on page 5.]

[39] OECD and T. Chopin, *Integrated Multi-Trophic Aquaculture*. OECD, 2010. [Online]. Available: https://www.oecd-ilibrary.org/content/component/9789264088726-15-en [Cited on page 5.]

[40] M. E. E. Alahi and S. C. Mukhopadhyay, “Detection methods of nitrate in water: A review,” *Sensors and Actuators A: Physical*, vol. 280, pp. 210–221, 2018. [Cited on page 6.]

[41] J. Davis, K. J. McKeegan, M. F. Cardosi, and D. H. Vaughan, “Evaluation of phenolic assays for the detection of nitrite,” *Talanta*, vol. 50, no. 1, pp. 103–112, 1999. [Cited on page 6.]

[42] A. Calvo-López, E. Arasa-Puig, M. Puyol, J. M. Casalta, and J. Alonso-Chamarro, “Biparametric potentiometric analytical microsystem for nitrate and potassium monitoring in water recycling processes for manned space missions,” *Analytica chimica acta*, vol. 804, pp. 190–196, 2013. [Cited on page 6.]

[43] W. Xuejiang, S. V. Dzyadevych, J.-M. Chovelon, N. J. Renault, C. Ling, X. Siqing, and Z. Jianfu, “Conductometric nitrate biosensor based on methyl viologen/nafion®/nitrate reductase interdigitated electrodes,” *Talanta*, vol. 69, no. 2, pp. 450–455, 2006. [Cited on page 6.]

[44] M. Y. Chong, M. Z. M. Jafri, L. H. San, and T. C. Ho, “Detection of nitrate ions in water by optical fiber,” in *2012 International Conference on Computer and Communication Engineering (ICCCE)*. IEEE, 2012, pp. 271–273. [Cited on page 6.]

[45] M. Tabatabai and W. Dick, “Simultaneous determination of nitrate, chloride, sulfate, and phosphate in natural waters by ion chromatography,” Wiley Online Library, Tech. Rep., 1983. [Cited on page 6.]

[46] P. S. Ellis, A. M. H. Shabani, B. S. Gentle, and I. D. McKelvie, “Field measurement of nitrate in marine and estuarine waters with a flow analysis system utilizing on-line zinc reduction,” *Talanta*, vol. 84, no. 1, pp. 98–103, 2011. [Cited on page 6.]

[47] A. Al Noman, J. N. Dash, X. Cheng, H.-Y. Tam, and C. Yu, “Mach-zehnder interferometer based fiber-optic nitrate sensor,” *Optics Express*, vol. 30, no. 21, pp. 38 966–38 974, 2022. [Cited on pages 6 and 8.]

[48] P. Singh, M. K. Singh, Y. R. Beg, and G. R. Nishad, “A review on spectroscopic methods for determination of nitrite and nitrate in environmental samples,” *Talanta*, vol. 191, pp. 364–381, 2019. [Cited on pages 6 and 8.]

[49] W. G. Crumpton, T. M. Isenhart, and P. D. Mitchell, “Nitrate and organic n analyses with second-derivative spectroscopy,” *Limnology and Oceanography*, vol. 37, no. 4, pp. 907–913, 1992. [Cited on page 6.]

[50] R. Norman and J. Stucki, “The determination of nitrate and nitrite in soil extracts by ultraviolet spectrophotometry,” *Soil Science Society of America Journal*, vol. 45, no. 2, pp. 347–353, 1981. [Cited on pages 6 and 7.]

[51] E. W. Rice, L. Bridgewater, A. P. H. Association *et al.*, *Standard methods for the examination of water and wastewater*. American public health association Washington, DC, 2012, vol. 10. [Cited on page 6.]

[52] K. M. Miranda, M. G. Espey, and D. A. Wink, “A rapid, simple spectrophotometric method for simultaneous detection of nitrate and nitrite,” *Nitric oxide*, vol. 5, no. 1, pp. 62–71, 2001. [Cited on page 7.]

[53] B. Jahn, R. Linker, S. Upadhyaya, A. Shaviv, D. Slaughter, and I. Shmulevich, “Mid-infrared spectroscopic determination of soil nitrate content,” *Biosystems Engineering*, vol. 94, no. 4, pp. 505–515, 2006. [Cited on page 7.]

[54] B. Gao, A. C. Walhof, D. A. Laird, F. Toor, and J. P. Prineas, “Analytical evaluation of mobile in situ soil nitrate infrared sensor designs for precision agriculture,” *IEEE sensors journal*, vol. 21, no. 18, pp. 20 200–20 209, 2021. [Cited on page 7.]

[55] R. Linker and A. Shaviv, “Nitrate determination using anion exchange membrane and mid-infrared spectroscopy,” *Applied spectroscopy*, vol. 60, no. 9, pp. 1008–1012, 2006. [Cited on page 7.]

[56] S. Motomizu, H. Mikasa, and K. Tôei, “Fluorometric determination of nitrite in natural waters with 3-aminonaphthalene-1, 5-disulphonic acid by flow-injection analysis,” *Talanta*, vol. 33, no. 9, pp. 729–732, 1986. [Cited on page 8.]

[57] Y. Moo, M. Matjafri, H. Lim, and C. Tan, “New development of optical fibre sensor for determination of nitrate and nitrite in water,” *Optik*, vol. 127, no. 3, pp. 1312–1319, 2016. [Cited on pages 8, 9, and 10.]

[58] M. Nehir, M. Esposito, C. Begler, C. Frank, O. Zielinski, and E. P. Achterberg, “Improved calibration and data processing procedures of opus optical sensor for high-resolution in situ monitoring of nitrate in seawater,” *Frontiers in Marine Science*, vol. 8, p. 663800, 2021. [Cited on pages ix and 10.]

[59] N. A. Aljaber, B. R. Mhdi, S. K. Ahmmad, J. F. Hamode, M. M. Azzawi, A. H. Kalad, and S. M. Ali, “Design and construction fiber sensor detection system for water nitrite pollution,” *IOSR J. Eng.*, vol. 4, no. 2, pp. 37–43, 2014. [Cited on page 8.]

[60] J. Camas-Anzueto, A. Aguilar-Castillejos, J. Castañón-González, M. Lujpán-Hidalgo, H. H. De Leon, and R. M. Grajales, "Fiber sensor based on lophine sensitive layer for nitrate detection in drinking water," *Optics and Lasers in Engineering*, vol. 60, pp. 38–43, 2014. [Cited on page 8.]

[61] T. B. Pham, H. Bui, H. T. Le, and V. H. Pham, "Characteristics of the fiber laser sensor system based on etched-bragg grating sensing probe for determination of the low nitrate concentration in water," *Sensors*, vol. 17, no. 1, p. 7, 2016.

[62] N. A. A. Kadir, N. Irawati, A. A. A. Jafry, N. M. Razali, A. Hamzah, and S. W. Harun, "Sodium nitrate sensor based on d-shaped fiber structure," *Measurement*, vol. 163, p. 107927, 2020. [Cited on page 8.]

[63] J. N. Dash, N. Negi, and R. Jha, "Graphene oxide coated pcf interferometer for enhanced strain sensitivity," *Journal of Lightwave Technology*, vol. 35, no. 24, pp. 5385–5390, 2017. [Cited on page 8.]

[64] E. Murray, P. Roche, K. Harrington, M. McCaul, B. Moore, A. Morrin, D. Diamond, and B. Paull, "Low cost 235 nm ultra-violet light-emitting diode-based absorbance detector for application in a portable ion chromatography system for nitrite and nitrate monitoring," *Journal of Chromatography A*, vol. 1603, pp. 8–14, 2019. [Cited on pages ix, 9, and 25.]

[65] M. S. Shur and R. Gaska, "Deep-ultraviolet light-emitting diodes," *IEEE Transactions on electron devices*, vol. 57, no. 1, pp. 12–25, 2009. [Cited on page 9.]

[66] M. Aman, G. Jasmon, H. Mokhlis, and A. Bakar, "Analysis of the performance of domestic lighting lamps," *Energy policy*, vol. 52, pp. 482–500, 2013. [Cited on page 10.]

[67] M. Born and E. Wolf, *Principles of optics: electromagnetic theory of propagation, interference and diffraction of light*. Elsevier, 2013. [Cited on pages 11 and 12.]

[68] T. G. Mayerhöfer and J. Popp, "Beer's law–why absorbance depends (almost) linearly on concentration," *ChemPhysChem*, vol. 20, no. 4, pp. 511–515, 2019. [Cited on pages 11, 12, and 13.]

[69] ——, "Beer's law derived from electromagnetic theory," *Spectrochimica Acta Part A: Molecular and Biomolecular Spectroscopy*, vol. 215, pp. 345–347, 2019. [Cited on page 12.]

[70] D. F. Swinehart, “The beer-lambert law,” *Journal of chemical education*, vol. 39, no. 7, p. 333, 1962. [Cited on page 13.]

[71] T. G. Mayerhöfer, A. V. Pipa, and J. Popp, “Beer’s law-why integrated absorbance depends linearly on concentration,” *ChemPhysChem*, vol. 20, no. 21, pp. 2748–2753, 2019. [Cited on page 13.]

[72] T. G. Mayerhöfer, S. Pahlow, and J. Popp, “The bouguer-beer-lambert law: Shining light on the obscure,” *ChemPhysChem*, vol. 21, no. 18, pp. 2029–2046, 2020. [Cited on page 13.]

[73] C. N. Banwell and E. M. McCash, *Fundamentals of molecular spectroscopy*. Indian Edition, 2017. [Cited on page 13.]

[74] C. C. Gerry and P. L. Knight, *Introductory quantum optics*. Cambridge university press, 2023. [Cited on page 13.]

[75] G. N. Lewis, “The conservation of photons,” *Nature*, vol. 118, no. 2981, pp. 874–875, 1926. [Cited on page 13.]

[76] W. D. Bare, “A more pedagogically sound treatment of beer’s law: A derivation based on a corpuscular-probability model,” *Journal of Chemical Education*, vol. 77, no. 7, p. 929, 2000. [Cited on page 13.]

[77] M. Berberan-Santos, “Beer’s law revisited,” *Journal of Chemical Education*, vol. 67, no. 9, p. 757, 1990. [Cited on pages 13 and 14.]

[78] D. L. Andrews, “A simple statistical treatment of multiphoton absorption,” *American Journal of Physics*, vol. 53, no. 10, pp. 1001–1002, 1985. [Cited on page 14.]

[79] Y. Ozaki, Y. Morisawa, A. Ikehata, and N. Higashi, “Far-ultraviolet spectroscopy in the solid and liquid states: a review,” *Applied Spectroscopy*, vol. 66, no. 1, pp. 1–25, 2012. [Cited on page 16.]

[80] R. A. Morton and R. Riding, “Absorption spectra of nitrates the region 300,” *Proceedings of the Royal Society of London. Series A, Containing Papers of a Mathematical and Physical Character*, vol. 113, no. 765, pp. 717–731, 1927. [Cited on page 25.]

[81] C. Opländer and C. V. Suschek, “The role of photolabile dermal nitric oxide derivates in ultraviolet radiation (uvr)-induced cell death,” *International Journal of Molecular Sciences*, vol. 14, no. 1, pp. 191–204, 2012. [Cited on page 26.]

[82] A. Barolet, I. Litvinov, and D. Barolet, “Light-induced nitric oxide release in the skin beyond uva and blue light: red & near-infrared wavelengths,” *Nitric Oxide*, vol. 117, pp. 16–25, 2021. [Cited on page 26.]

[83] F. C. Bononi, Z. Chen, D. Rocca, O. Andreussi, T. Hullar, C. Anastasio, and D. Donadio, “Bathochromic shift in the uv–visible absorption spectra of phenols at ice surfaces: insights from first-principles calculations,” *The Journal of Physical Chemistry A*, vol. 124, no. 44, pp. 9288–9298, 2020. [Cited on page 26.]

[84] M. Maraj, L. Min, and W. Sun, “Reliability analysis of algan-based deep uv-leds,” *Nanomaterials*, vol. 12, no. 21, p. 3731, 2022. [Cited on page 29.]

[85] H. Hirayama, S. Fujikawa, and N. Kamata, “Recent progress in algan-based deep-uv leds,” *Electronics and Communications in Japan*, vol. 98, no. 5, pp. 1–8, 2015. [Cited on page 29.]

[86] *7/8-Bit Single/Dual SPI Digital POT with Volatile Memory*, MICROCHIP. [Online]. Available: https://pt.mouser.com/datasheet/2/268/22060b-3443475.pdf [Cited on page 37.]

[87] *LM317 3-Terminal Adjustable Regulator*, Texas Instruments. [Online]. Available: https://pt.mouser.com/datasheet/2/389/lm217-1849593.pdf [Cited on pages 37 and 38.]

[88] *ANTC THERMISTOR OF MF52 TYPE SERIES SPECIFICATION*, Vinnakoda. [Online]. Available: https://www.gotronic.fr/pj2-mf52type-1554.pdf [Cited on page 54.]

[89] *ADS101x Ultra-Small, Low-Power, I2C-Compatible, 3.3-kSPS, 12-Bit ADCs With Internal Reference, Oscillator, and Programmable Comparator*, Texas Instruments. [Online]. Available: https://cdn-shop.adafruit.com/datasheets/ads1015.pdf [Cited on page 54.]

A. Lens testing

A.1. Objective

Because LED2 has a viewing angle too big and the optical path will be bigger than the focal length of the LC7 lens, if we just use the LED, the signal detected by the GUVV-T21GH photodetector is too small. The use of a lens can be a good solution to overcome this problem. To analyze if this approach is successful, we have to see the absorption spectrum of the lens material (PMMA) and verify its focal distance.

A.2. Methodology

To observe the absorption spectrum of the lens, we used a tungsten-deuterium lamp and a UV-VIS spectrometer (*OceanOptics*). Both are connected to a collimator via a UV-VIS optical fiber. To verify that the spectra observed is the the absorbance spectra of the lens, the space between the collimators and the lens was minimized so that the lens effect of the lens doesn't affect the results. The collimator size was smaller the lens which facilitated this analysis. These three parts were aligned and the spectra of the tungsten-detuterium lamp spectrum was observed before and after putting the lens.

To verify the focal distance of the lens, it was used the LED2 and the GUVV-T21GH photodetector. The three components were aligned and the distance between the LED was changed between 1 and 9mm with a step of 1mm. The distance of the lens to the photodetector was kept constant.

A.3. Results

The absorbance spectra of the lens is represented in figure A.1. It's possible to observe that there is absorbance through all the wavelengths detected. It's clear that the lens absorbs mostly wavelengths $<$ 280nm. With an absorbance peak in $\sim$ 250nm. For the emission range of the LED2, the absorbance is almost constant,$\sim$ 5dB, which is small enough to be used. This lens could have not been used for LED1 because the peak in absorbance of PMMA is close to 230nm. If for some reason, this LED needed to be collimated, a lens of UV fused sillica would be the option.

By figure A.2, it's possible to verify that the focal distance of the lens must be between 7mm$< d_f <$8mm. The photodetector was saturated for 7mm and 8mm, giving an output voltage of 3.3V. To avoid the saturation of the photodetector, the LED could have been

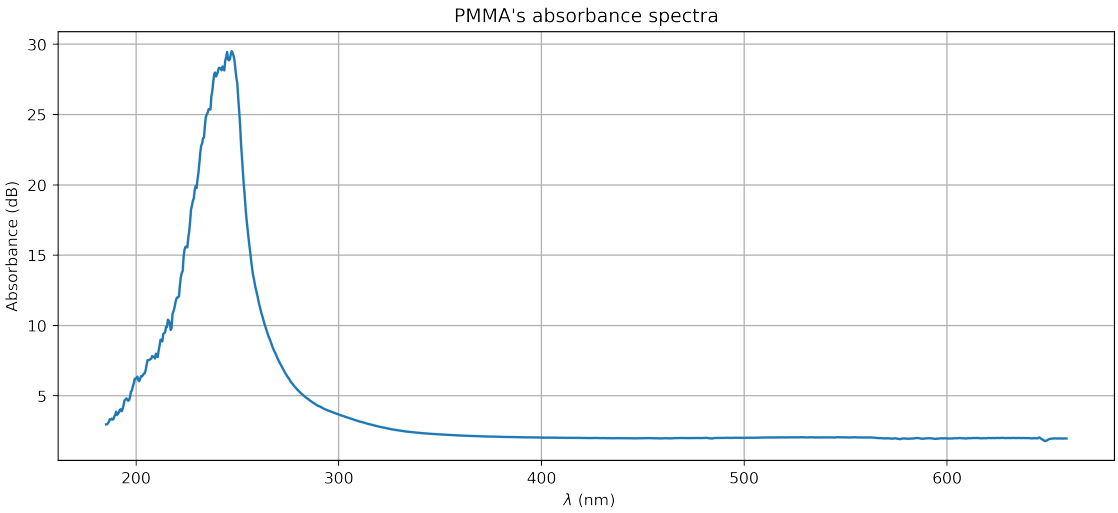

Figure A.1: Absorbance spectra of the lens

supplied with smaller currents. More tests should have been made too. The results in Figure A.2 This are in accordance with the datasheet, where is given a focal distance of 7.8mm for the lens. A lens with a smaller focal length would be the optimal approach and improvement so more light could be collimated. Because the focal length of the lens is between 7 to 8mm, and this lens has an height of 5.5mm, only 40º of the 120º will be used.

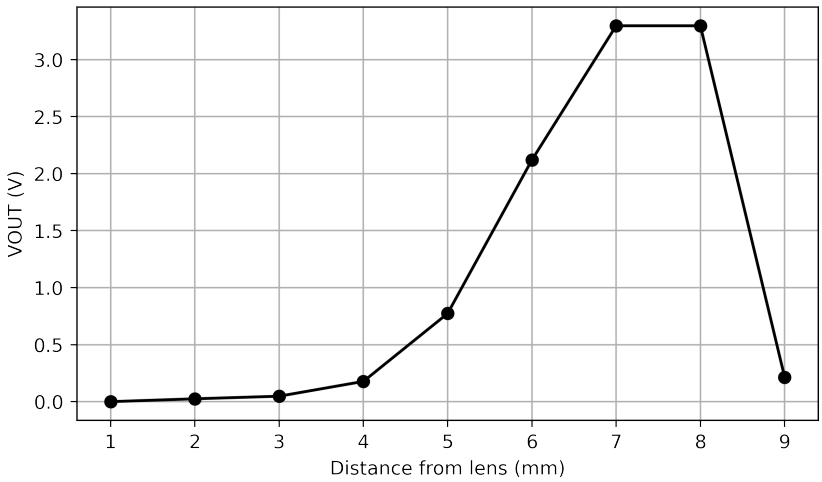

Figure A.2: Photodetector voltage output vs distance between the LED and the lens

B. Filter testing

B.1. Objective

Many times, when designing an electronic circuit in PCB, many changes have to be done. To avoid this issue and to verify if the circuit truly works, the filter was built and the voltage before and after going through the filter was observed. The same circuit was used so that SPI communication with a microcontroller would be tested.

B.2. Methodology

To test if the filter worked, the circuit used is displayed in figure B.1. The setup is built with the LED1 and the TOCON_ABC1 photodetector. The supply is given by a simple voltage divider circuit controlled by a potentiometer MCP42100 with a coupled buffer circuit or unity gain amplifier, op-amp LM1084, to separate the impedance of the LED/photodetector from the rest. The voltage output of the photodetector and of the filter was registered with an Arduino Due. Because the potentiometer used was in the order of 10kΩ, the resistors used had to be adjusted for those orders too. These were also supplied with 3.3V which limits the voltage between the terminals of the potentiometer. The filter being tested is a low-pass sallen key active filter with a cutoff frequency of 100mHZ and a decay of -40dB/decade.

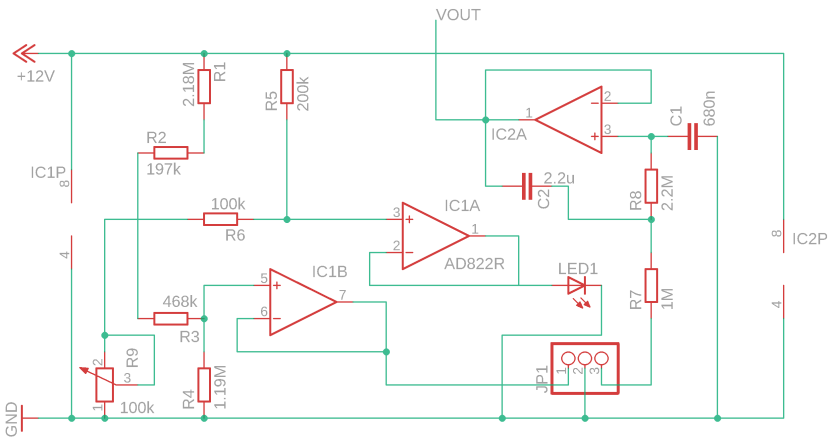

Figure B.1: Circuit used to verify if the electric filter works

The measurements were done by comparing the voltage measured before and after the signal going through the filter. It was used the standard solution of $NO^{3}\_$ and $NO^{2}\_$ diluted in distilled water and the concentration was varied between 0 to 30ppm. The sample frequency of the Arduino was chosen to be as big as possible so that every value could

be recorded and taken in account. The optical path chosen is 10mm. The supply for the whole circuit was done by using a transformer connected from the AC power plugs to the breadboard with an output voltage and current of 12V and 2A, respectively.

B.3. Results

In figure B.2 is shown the probability distribution of the values measured by the Arduino pin for each concentration. The narrower the probability distribution, the more precise is each measurement and less fluctuations/noise is found. By comparing how narrower is each probability distribution before (top) and after (top), after using the filter, by just choosing any random sample of values measured for each concentration, it's possible to distinguish between variations of 5ppm for the range tested, existing really small overlap between the 20 and 25ppm and 25 and 30ppm distributions. This was not observed before the signal goes through the filter as only for 5 and 10ppm distributions is where it's found no overlap. The increase in concentration for both states seem to imply a narrower distribution as for both, from 5ppm to 30ppm it's possible to see a narrowing of the distributions.

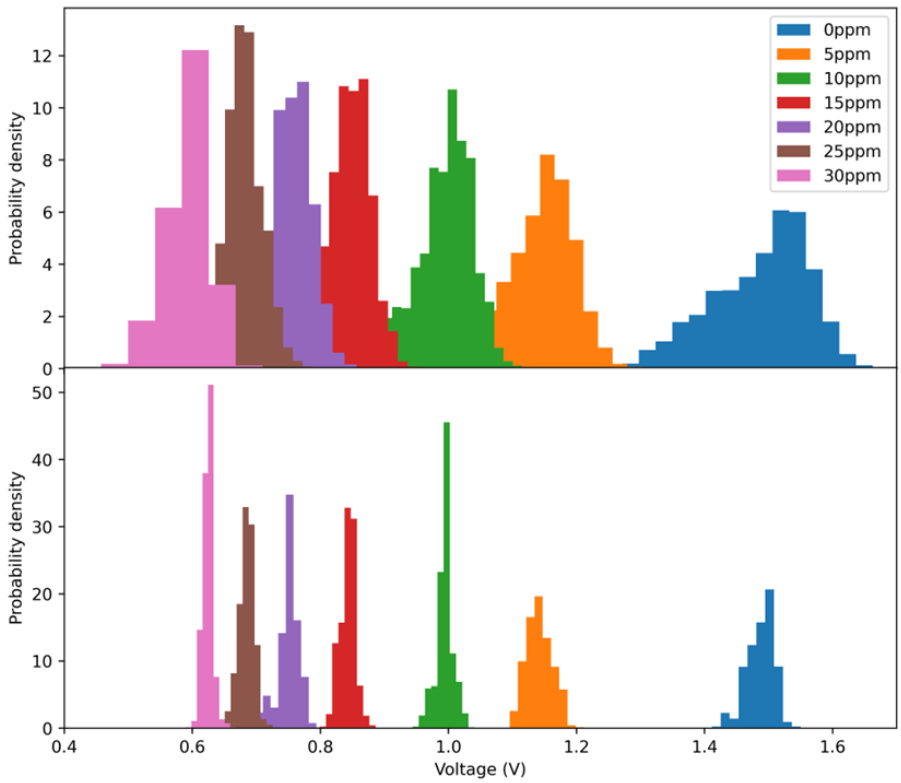

Figure B.2: Signal value distribution for every concentration before and after the filter being used.

C. Full circuit

C.1. Before update

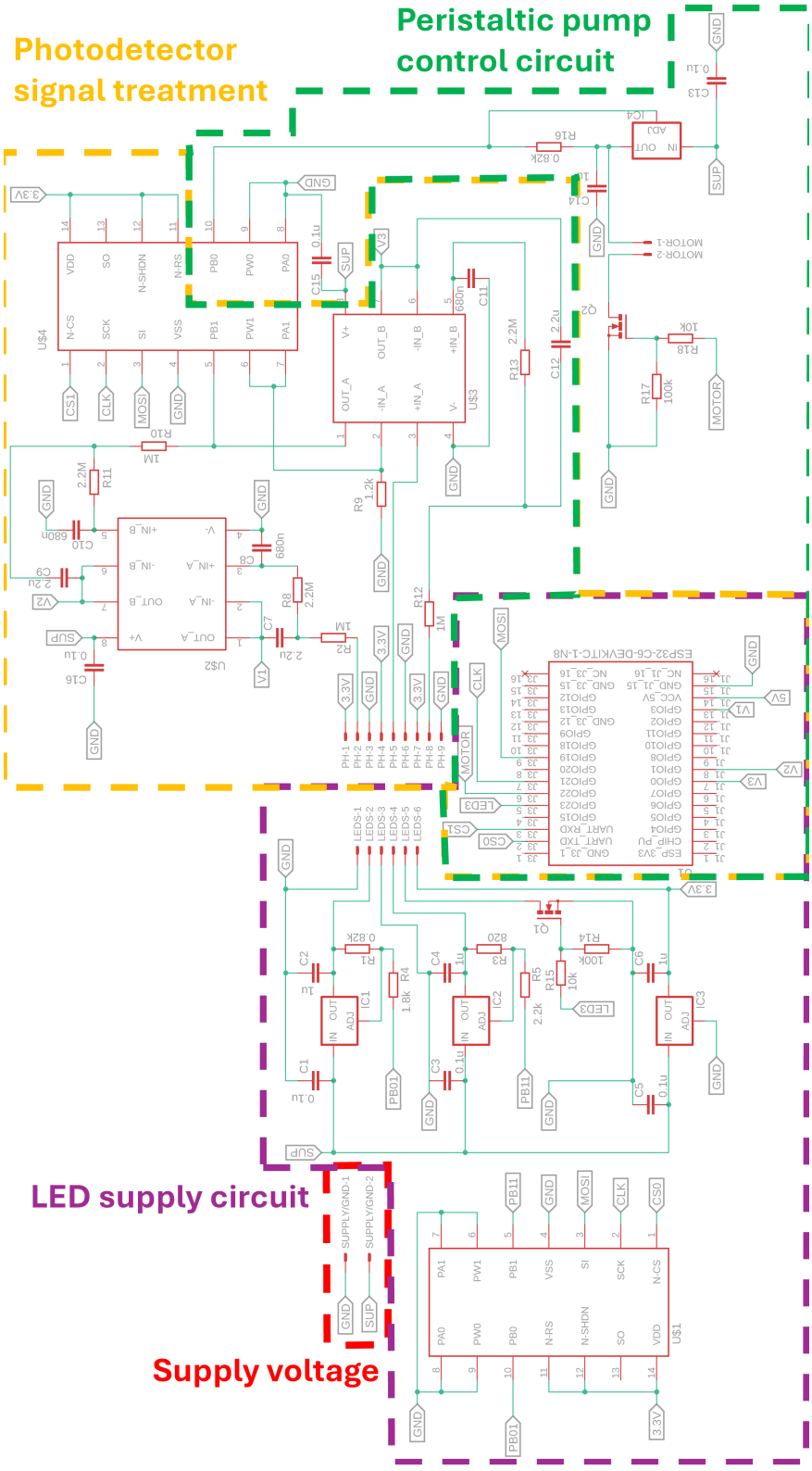

Figure C.1: Full circuit schematic with each zone represented.

C.2. After update

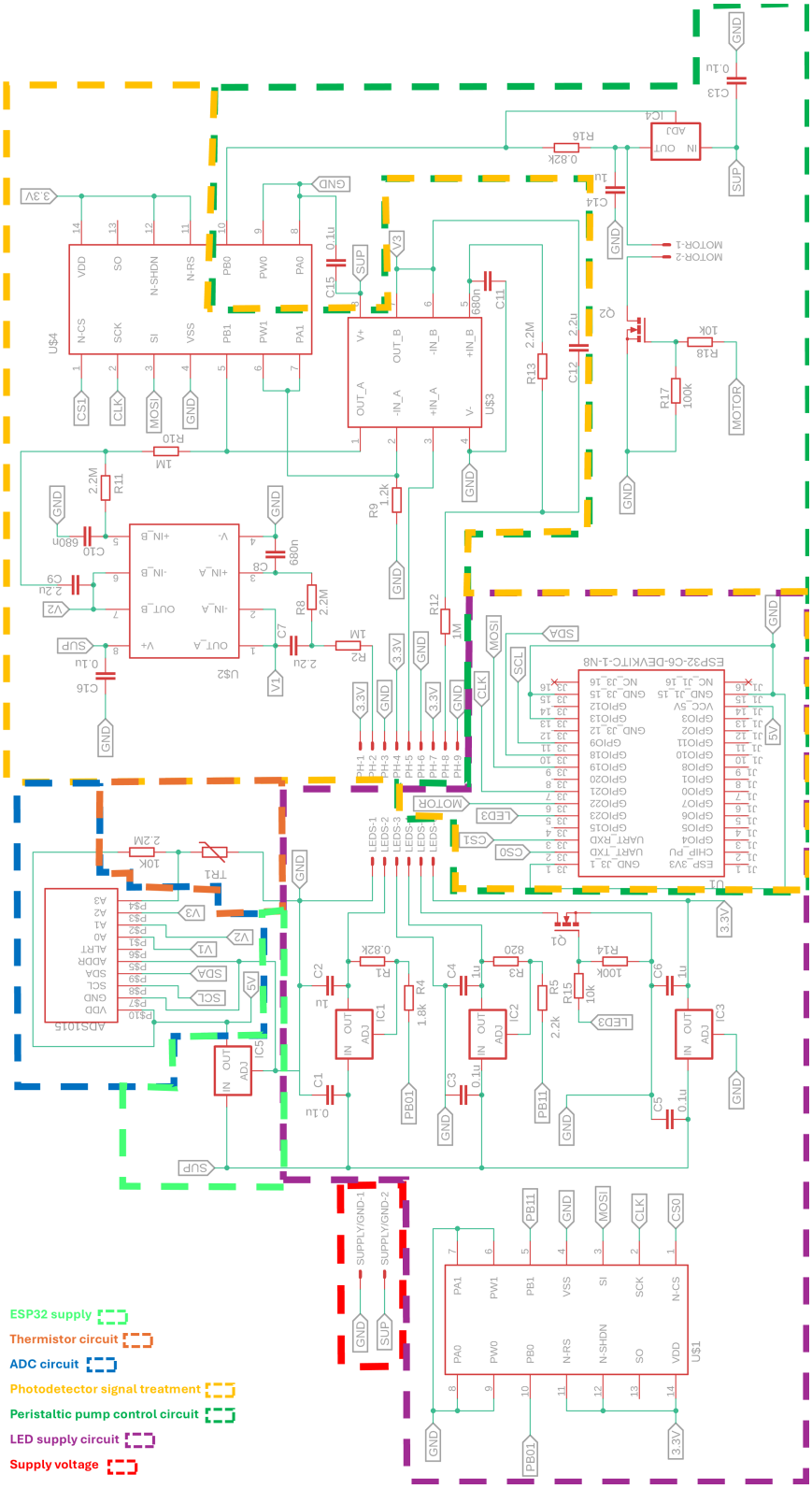

Figure C.2: Full updated circuit schematic with each zone represented.

D. Code developed for sensor Testing

D.1. Arduino IDE

```
void writePot(byte csPin, byte command, byte value) {
    digitalWrite(csPin, LOW); //select the selection pin of the device
    SPI.transfer(command); //Transfer command byte by SPI communication
    SPI.transfer(value); //Transfer the value byte of the potentiometer
    digitalWrite(csPin, HIGH); //de-select the potentiometer
    }

float A230(float X) {
    return 40.1 * pow(X, 1.20) * exp(0.53 * pow(X, 2.65));
}

float A300(float X) {
    return 523 * pow(X, 0.86) * exp(0.00312 / pow(X, 1.30));
}

void setup(){
    SPI.begin(clk, miso, mosi, ss); \\begin SPI communication
    pos0=30;    \\LED of 230nm potentimeter's position
    pos1=120;   \\LED of 300nm potentimeter's position

    \\turn on the detection LEDs by communicating with potentiometer 1
    writePot(csPin1, WRITE_WIPER0, pos0);
    delay(100);
    writePot(csPin1, WRITE_WIPER1, pos1);

    pos0=110;  \\Peristaltic pump potentiometer's position
    pos1=250;  \\Amplification potentiometer's position

    \\communicating with potentiometer 2
    writePot(csPin2, WRITE_WIPER0, pos0); \\Increase voltage across the
    terminals the peristaltic pump
    writePot(csPin2, WRITE_WIPER1, pos1); \\Increase amplification factor
    delay(100);
    digitalWrite(motor, HIGH); \\turn on the peristaltip pump
    delay(9000);
    digitalWrite(motor, LOW); \\turn off the peristaltic pump
    writePot(csPin2, WRITE_WIPER0, 0); \\Decrease the voltage across the pump

```

```
    SPI.end();

    Serial.begin(115200); \\begin Serial
    Wire.begin(SDA, SCL);  \\begin I2C communication
    ads.begin(0x48));  \\initialize the ADC ADS1015
    sumv230=0;      \\Variable used for the LED of 230nm
    sumv300=0;      \\Variable used for the LED of 300nm

    \\begin saving data
    for (int i = 0; i < 3000; ++i) {
        sumv230 =sumv230 + ads.readADC_SingleEnded(0);
        sumv300 =sumv300 + ads.readADC_SingleEnded(1);
        delay(10);
    }

    v230=(sumv230/3000);   \\Average values
    v300=(sumv300/3000);   \\Average values
    conc230=A230(v230,Ag230);  \Concentration determined by the LED1
    conc300=A300(v300,Ag300); \\Concentration determined by the LED2
}
```

D.2. Visual Studio Code

```
def read_serial():
    global befo_line
    with open(file_path, 'a') as file: #open the txt file in the file path
        while True:
            try:
                line_read = ser.readline().decode('utf-8').strip()#read serial
                if line_read:
                    file.write(line_read + '\n') #write line read in the txt
                    file.flush()   #update the txt file with the information
                    if befo_line == "Concentração 230nm":
                        now = datetime.now()#Time when the data gets captured
                        hor = now.strftime("%Y-%m-%d %H:%M:%S")
                        file.write(str(hor) + '\n') #write the time in the txt
                        file.flush()
                        ls.append(float(line_read))  #append lines in "ls" list
                        tim.append(hor)  #append time in "tim" list
                    befo_line = line_read
plt.ion()  # Enable interactive mode
fig, ax = plt.subplots()  #create plot
line, = ax.plot(tim, ls, "o-") #draw the tim and ls array in the plot
```

```
21
22
23 plt.show(block=False)
24 thread = threading.Thread(target=read_serial, daemon=True)
25 thread.start()  #start thread
26 while True:
27     try:
28         line.set_xdata(tim)
29         line.set_ydata(ls)
30         ax.relim()
31         ax.autoscale_view()
32         fig.canvas.draw()
33         fig.canvas.flush_events()
34         time.sleep(0.1)
```